STUDIES OF HIGH TEMPERATURE SUPERCONDUCTORS

(Advances in Research and Applications)

Volume 45
Cuprates
and Some Unconventional Systems

ANANT NARLIKAR
EDITOR
Inter-University Consortium for DAE Facilities, Indore, India

Nova Science Publishers, Inc.
New York

Coordinating Editor: Tatiana Shohov
Senior Editors: Susan Boriotti and Donna Dennis
Office Manager: Annette Hellinger
Graphics: Wanda Serrano
Editorial Production: Vladimir Klestov, Matthew Kozlowski and Maya Columbus
Circulation: Ave Maria Gonzalez, Vera Popovic, Luis Aviles, Raymond Davis, Melissa Diaz and Jeannie Pappas
Communications and Acquisitions: Serge P. Shohov
Marketing: Cathy DeGregory

Library of Congress Cataloging-in-Publication Data
Available upon request.

ISBN 1-59033-697-6

400 Oser Ave, Suite 1600
Hauppauge, New York 11788-3619
Tele. 631-231-7269 Fax 631-231-8175
e-mail: Novascience@earthlink.net
Web Site: http://www.novapublishers.com

Printed in the United States of America

SUPERCONDUCTIVITY OF HIGH-PRESSURE PHASES IN THE METAL-HYDROGEN SYSTEMS

I.O. Bashkin, V.E. Antonov and E.G. Ponyatovsky

Institute of Solid State Physics, Russian Academy of Sciences
142432 Chernogolovka, Moscow district, Russia

1. INTRODUCTION

Initiation or enhancement of superconductivity in metals due to hydrogen absorption has been a rare and rather unpredictable phenomenon so far. The first superconducting hydride, Th_4H_{15}, has been discovered in 1970 [1]. It had a superconducting temperature of $T_c = 8.05$ to 8.35 K and was thermally stable at ambient conditions. Two years later Skoskiewicz [2] reported on the discovery of superconductivity in non-stoichiometric palladium hydrides with H-to-metal atomic ratios of $n = 0.81$ and 0.87 produced by electrolytic hydrogenation [2]. The Pd – H(D) system has been a promising subject for experimental and theoretical investigation of superconductivity in the metal–hydrogen systems due to the simple *fcc* structure of the Pd sublattice, the broad homogeneity range $0.65 < n < 1$ of hydrogen solid solutions and the superconducting temperature strongly depending on the hydrogen content and reaching about 9 K in the hydrides and 11 K in the deuterides at $n \to 1$. The extensive study on the Pd – H(D) and related systems to 1978 was reviewed by Stritzker and Wühl [3]. Later research, however, gave no unambiguous examples of hydrogen-induced enhancement of the superconducting properties among the metal–hydrogen systems stable near normal conditions.

A notable advance in the study of the hydrogen-induced superconductivity was achieved with the use of hydrogen implantation. Stritzker *et al.* implanted hydrogen isotopes into metals at liquid-helium temperatures and observed postirradiation superconductivity in thin hydrogenated layers formed in the metal matrices, often with the inverse isotope effect (see Ref. [3]). After heating the samples to room temperature, the hydrogen atoms dissipated over the metal matrix and the

superconductivity vanished. A more detailed study of superconducting samples of this kind encountered serious problems.

Fruitful methods to produce new Me-H superconductors became the high-pressure treatment of the known metal hydrides in inert medium and the synthesis of new hydrides from metals subjected to high hydrogen pressure. The former method is used at ISSP RAS to obtain new hydrides of metals like Ti and Zr, which easily absorb hydrogen at low pressures and do not lose it in inert media, even at elevated temperatures. The second method is useful with metals that do not form hydrides at moderate hydrogen pressures. The technique for compressing gaseous hydrogen to pressures of up to 9 GPa at temperatures to 770 K developed at ISSP RAS [4] made it possible to synthesize hydrides of all 3*d*-metals and all 4*d*-metals except Ru. In particular, hydrides of Fe, Co, Mo, Tc, Rh and Re and various alloys of *d*-metals have been synthesized at ISSP for the first time. Both techniques allow rapid cooling of the prepared hydrides to liquid-nitrogen temperature under high pressure. Cooled to such a low temperature, all hydrides are metastable at ambient pressure therefore they can be recovered from the high-pressure cell to study their composition, crystal structure and other properties.

This work is to review the properties of the superconducting metal–hydrogen systems prepared with the use of high pressure. The authors are not aware of any other papers reviewing superconductivities of hydrides since that by Stritzker and Wühl [3] therefore relevant references will also be given to the papers presenting the studies on the stable metal–hydrogen systems and on the hydrogen-implanted metals.

2. TITANIUM HYDRIDES

2.1 Superconducting phases in the *T–P–c* phase diagram

Superconducting transitions in the pressure-treated titanium hydrides were first observed in 1985 [5,6] when several TiH_n samples with $0.13 \le n \le 0.85$ were quenched from about 600 K to liquid nitrogen under pressures of 4.5 to 6.5 GPa. Further studies revealed the occurrence of three superconducting phases in the Ti–H system. One of these phases has a stability region under high pressure, while the other two appear as the products of non-equilibrium phase transformations in the process of the high-pressure quenching and further treatment. For the sake of clarity, the presentation of superconducting properties of the Ti–H system will be preceded by a sketch of its *T–P–c* phase diagram. The phenomena underlying the origin and modification of the superconducting properties will be considered at the end of this Section.

The *T–c* phase diagram of the Ti–H system at ambient pressure has been a subject of an extensive research. The principle features of the diagram were assessed by San-Martin and Manchester [7]. The Ti–H system undergoes the eutectoid β–(α+δ) transformation at 573 K. The high-temperature β–phase is the solid solution of hydrogen in the body-centred cubic (*bcc*) lattice of β–Ti; the α–phase is the dilute solid solution of hydrogen in the hexagonal close-packed (*hcp*) lattice of β–Ti and the

α–phase is the non-stoichiometric dihydride with a face-centred cubic (*fcc*) metal sublattice and the composition $TiH_{\approx 1.5}$ at the eutectoid point. The eutectoid composition of the α–phase determined from calorimetric data is $n = 0.74$ ($c = 42.5$ at.% H) [8]. A small isotope effect is observed for the Ti–D system where $T_{eut} = 587$ K and $n_{eut} = 0.72$ ($c = 41.9$ at.% D) [8]. Closer to the stoichiometric composition and below 310 K, the *fcc* dihydrides with $n \geq 1.8$ undergo a transition to the ε–TiH_n phase with a face-centred tetragonal (*fct*) metal sublattice and the axial ratio $c/a < 1$. Hydrogen atoms in all these phases are randomly distributed on tetrahedral interstitial sites (tetrasites) [7,9,10]. There was presented a thermodynamic argumentation based on the calorimetric and volume measurements [8,11,13] that one more phase is also stable at ambient pressure. This phase, the ordered γ–TiH monohydride, transforms irreversibly to the α+δ two-phase state upon heating above 441 K. In the Zr–H system with a similar *T*–*c* diagram the γ↔α+δ transformation is reversible though sluggish [14-16]. The Ti atoms in γ–TiH form a face-centred orthorhombic sublattice with the axial ratios $b/a \approx 1.015$ and $c/a \approx 1.09$ whereas the hydrogen atoms occupy tetrasites on alternate (110) planes [9,10,12,17]. The present-day outline of the equilibrium *T*–*c* phase diagram [18,19] is shown in the left-hand part of Fig. 1.

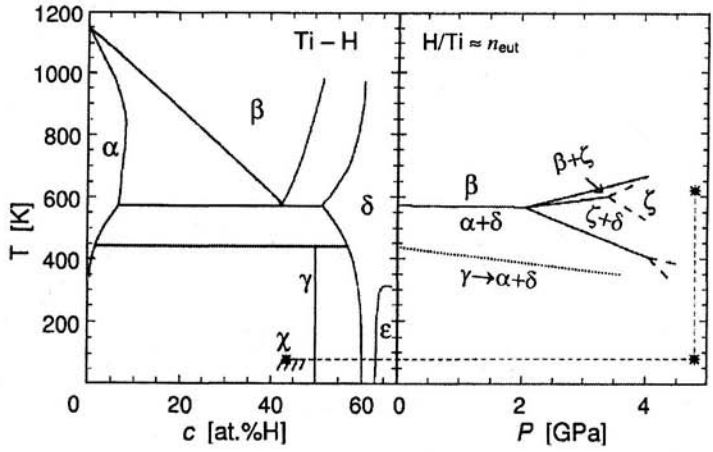

Fig. 1. Phase diagram of the Ti–H system [19]. The left-hand part shows the *T*–*c* projection at atmospheric pressure and the right-hand part is the *T*–*P* projection for the near-eutectoid hydrides. The path of quenching of the ζ–phase is represented by the dashed line and the metastability region of the resulting χ–phase is hatched. In the right-hand part of the figure, the low-temperature boundary of the ζ–phase stability region terminates with a dashed fork indicating the formation of one more high-pressure phase near these conditions; the line of the irreversible γ↔α+δ transition occurring on heating the γ–phase [24] is dotted.

The high-pressure behavior of the Ti–H system was studied in the composition range around the eutectoid point using differential thermal analysis (DTA), X-ray diffraction, the resistivity and volume measurements [8,13,19-24]. The right-hand part of Fig. 1 shows that the temperature of the eutectoid equilibrium as well as that of the $\gamma \leftrightarrow \alpha+\delta$ transition decrease under pressure with $dT/dP = -4$ and -25 K/GPa, respectively. The eutectoid line ends in the quadruple point located at $P = 2.05$ GPa, $T \approx 560$ K and $n \approx 0.69$ [22]. A new phase, ζ, becomes stable at pressures above this point. The initial slope of the high-temperature boundary of the ζ-phase stability region is $dT/dP = 50$ K/GPa. The low-temperature $\zeta \leftrightarrow (\alpha+\delta)$ transformation shows a hysteresis increasing with pressure so that the initial slopes of the direct and inverse transformations are -45 and -115 K/GPa, respectively. The T–c projections of the T–P–c phase diagram of the Ti–H system at $P \approx 1$ atm and 2.7 GPa are compared in Fig. 2 [24]. A similar shape of the T–c phase diagram was reported also for a pressure of 5 GPa [25], but with few experimental details. The main isotope effect in the T–P diagram of the Ti-D system is that the quadruple point is displaced to a pressure of 3.4 GPa [13,24].

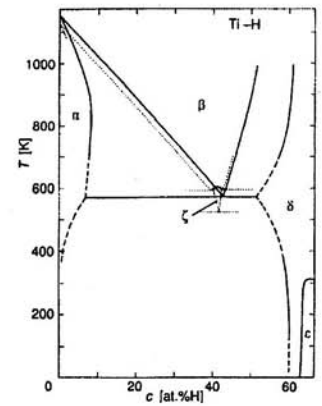

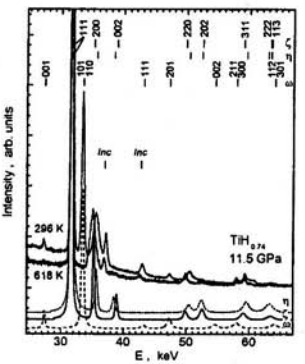

Fig. 2 (left). $T-c$ phase diagrams of the Ti – H system for $P \approx 1$ atm (solid and dashed curves) and 2.7 GPa (dotted lines) [24]. The width of the ζ–phase region is given only tentatively whereas the temperature values correspond to the experimental ones.

Fig. 3 (right). Energy dispersive X-ray diffraction spectra of $TiH_{0.74}$ at $T = 296$ K and 618 K measured in the course of heating at $P = 11.5$ GPa (top curves) and simulated diffraction patterns for the η, ζ and ω phase (bottom curves) [19,26]. The diffraction patterns of the ζ and η phases are indexed on the basis of the *fct* unit cell, the ω phase is hexagonal. The patterns also include reflections from the Inconel gasket of the high-pressure cell (marked).

Because of the slow kinetics at temperatures below 370 K, the $\zeta \rightarrow (\alpha+\delta)$ transformation became sluggish around 4 GPa and was no more fixed by DTA above 4.5 GPa [24]. The resistivity anomaly due to the $\gamma \rightarrow (\alpha+\delta)$ transformation was distinct to 3.3 GPa but became diffuse and indiscernible before the $\gamma \rightarrow (\alpha+\delta)$ and $\xi \rightarrow (\alpha+\delta)$ transition lines intersected near 3.8 GPa [8]. In contrast, the resistivity anomaly accompanying the $(\alpha+\delta) \rightarrow \zeta$ transformation in heating runs on TiH_n is split above 4 GPa and appeared as two isolated jumps therefore it was assumed that one more phase can be stable in the Ti–H system under pressure [24]. The second high-pressure phase, η, was found, indeed, using the *in situ* X-ray diffraction on $TiH_{0.74}$ [19,26]. The $\zeta \leftrightarrow (\omega+\eta)$ phase transitions were observed in isobaric heating/cooling runs at pressures of 6.3 and 11.5 GPa. The diffraction patterns of ζ–$TiH_{0.74}$ and $(\omega+\eta)$–$TiH_{0.74}$ are reproduced in Fig. 3. The hexagonal ζ phase is a high-pressure phase of pure titanium [27] and is characterized by low hydrogen solubility [20-22]. Its precipitation upon cooling of single-phase ζ–$TiH_{0.74}$ evidences that the hydrogen content of the η phase exceeds that of ζ.

Two other titanium hydrides, χ and κ, have no stability region in the equilibrium T–P–c phase diagram and appear as a result of the high-pressure quenching of the ζ phase. The procedure is schematically shown with the dashed line in Fig. 1 and includes the compression of a two-phase $(\alpha+\delta)$–TiH_n sample with a near-eutectoid composition and its further thermal treatment in the stability region of the ζ phase, normally around 6.5 GPa and 650 K during 15 to 20 min, followed by cooling at a rate of about 10^3 K/min. Recovery of the quenched sample to ambient pressure and its storage are carried out under liquid nitrogen. After this treatment, the TiH_n sample transforms to the single-phase state designated as the χ phase. Homogeneous χ–TiH_n samples were prepared in the composition range $0.69 < n < 0.92$. Outside this interval, either the ω or δ phase coexists with the quenched χ phase. The κ–TiH_n phase forms as an intermediate transformation product when the χ phase is heated above 95 K. The phase transformations at ambient pressure are discussed below in more detail.

Numerous structural data on the stable Ti–H(D) phases at ambient pressure obtained up to 1985 are compiled in Ref. [7]. Several later works supplemented this review with X-ray [12,17,19,24] and neutron diffraction [9,10,12,15,28,29] data on the structures of the stable and metastable phases and their thermal behavior at ambient and high pressures. The real-time neutron diffraction and small-angle scattering experiments at low and elevated temperatures [9,10] removed some ambiguities mentioned in Ref. [7] with regard to the sites occupied by hydrogen in the crystal structure of those phases. Representative data are listed in Table 1.

Here we comment on these data only briefly:

i) Hydrogen dissolved in the ω phase occupies tetrasites. The maximum hydrogen solubility of about 8 at.% is reached well above the eutectoid temperature.

ii) The ω phase only is observed in the $TiH(D)_{\sim 0.06}$ samples after a high-pressure quenching. Its lattice parameters at 100 K coincide with those for pure ω–Ti. The effect of hydrogen on the $\alpha \rightarrow \omega$ transition in titanium reaches saturation near

$n = 0.13$ [20,21]. Together with the data on superconductivity discussed below, this was the basis for the conclusion that the equilibrium hydrogen solubility in the α and ω phases is rather small.

iii) Hydrogen occupies only tetrasites in the β phase.

iv) Two methods are known to prepare the γ phase. The product of the transformation of the γ phase quenched under pressure consists of about 70% γ phase and 30% fine-grained Ti precipitates with the grain size 70 to 200 Å [33]. Otherwise, up to 10% γ phase in the (α+δ) matrix was obtained at $P = 1$ atm after cooling $TiH(D)_n$ samples from above the eutectoid temperatures [28,34]. Different microstructure and the internal stress of the samples can explain some scatter in the lattice parameters of the γ phase reported in Refs. [9,10,17,28]. The difference in the values of the deuterium occupancy numbers, $p_D = 0.96(1)$ [9,10] and $p_D = 0.85(8)$ [28], in the γ phase should be related rather to much lower content of this phase in the samples in Ref. [28] resulting in a lower accuracy of the data fit.

v) There is a marked scatter in the available data on the lattice parameters and the homogeneity ranges of the δ and ε dihydrides (see [7] and references therein). The scatter can partly be due to grain-structure and stress effects. Both δ and ε structures have been obtained at the stoichiometric composition. Dyuzheva et al. [37] observed the *fcc* δ–$TiH_{1.97}$ hydride with $a = 4.454$ Å at ambient pressure and its transformation to the ε phase upon the initial compression to 0.2 GPa, then the ε phase was stable up to 34 GPa. A significant extension of the range of thermal stability at 5 GPa was reported for the ε phase in Ref. [25].

vi) The high-pressure phases ζ and η were studied *in situ* only by X-ray diffraction [19,24,26]. The assumption of Ref. [19] that hydrogen occupies tetrasites in the ζ phase and octasites in the η phase is therefore speculative. Besides, the suggested tetragonal structures of those two phases were derived from fitting the peak positions in the experimental diffraction spectra rather than the peak intensities and shapes [19]. Other features, *e.g.* the large width of the (200) peaks in Fig. 2, denote that the true structure of the ζ and η phases can have a lower symmetry.

vii) Reitveld analysis of the χ phase neutron diffraction pattern became possible when large isotropic $TiD_{0.73}$ samples were quenched under pressure [29]. The structure parameters of the χ and κ phases were not refined in earlier works [9,10] due to the strong texture in the samples, as discussed in Ref. [18]. A remarkable feature of the χ phase is that hydrogen occupies octasites in the metal lattice, while it sits on tetrasites in other TiH_n phases. Among binary hydrides of *d*-metals, only the V–H(D) system gives another example of a change in the type of interstices occupied by hydrogen depending on the external conditions [38].

Table 1. $TiH(D)_n$ crystal structures and lattice parameters determined under the conditions indicated in the last but one column. Preference is given to the *fct* rather than *bct* unit cells for convenient comparison.

Phase	*n*	Metal lattice	Space group	H sites	*a* [Å]	*b* [Å]	*c* [Å]	*c/a*	Exper. conditions	Ref.
α		*hcp*	$P6_3/mmc$	tetra	2.9511		4.6843	1.5873	297 K	[3,26]
ω		*hex.*	*P6/mmm*		4.625		2.813	0.608	Room *T*	[23,27]
β	0.66	*bcc*	*Im3m*	tetra	3.36				653 K	[28]
	0.74				3.383				760 K	[6]
γ	≈1	*fco*	*Cccm*	ordered tetra	4.168	4.234	4.577	1.098	Room *T*	[5,6]
					4.189	4.230	4.584	1.094		[29]
δ	1.55	*fcc*	*Fm3m*	tetra	4.404				Room *T*	[32]
	1.84				4.433					
ε	≈1.98	*fct*	*F4/mmm*	tetra	4.487		4.358	0.971	Room *T*	[32]
	1.99				4.528		4.279	0.945	79 K	[33]
ζ	0.74	*fct*			4.253		3.854	0.906	618 K, 11.5 GPa	[15]
η	>0.74	*fct*			4. 214		3.909	0.926	296 K, 11.5 GPa	[15]
χ	0.73	*fct*	*F4/mmm*	octa	4.226		4.009	0.949	90 K	[25]
κ	0.74	*fct*		tetra, partial order	≈4.20		4.365	1.04	150 200 K	[5]
	0.94						4.524	1.08		

2.2. Superconducting properties of titanium hydrides

Three of the above phases of the Ti–H(D) system are superconducting. Superconductivity was found first in the χ phase quenched under pressure [5,6]. A detailed determination of the $T_c(n)$ dependence was completed using the magnetic susceptibility measurements [22]. Fig. 4 presents the T_c data collected through the composition range $n = 0.06$ to 1.15 for hydrides and $n = 0.61$ to 1.23 for deuterides quenched under a pressure of 6.3 GPa. There was a special care to retain the quenched phase, and the superconducting transition width was usually about 0.1 K. The inverse isotope effect is distinctly seen: T_c =4.3 K for χ-TiH_n and T_c =5.0 K for χ-TiD_n. A remarkable feature is that the T_c values are independent of composition through the homogeneity range $0.69 \leq n \leq 0.92$ of the quenched χ phase.

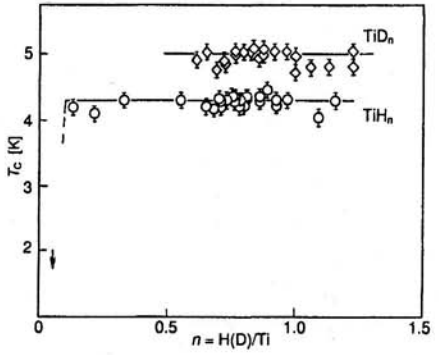

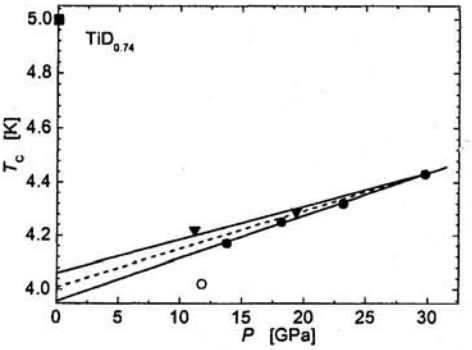

Fig. 4 (left). Superconducting temperatures of TiH_n and TiD_n quenched to liquid nitrogen at $P = 6.3$ GPa [22]. The arrow indicates that $TiH_{0.06}$ is not superconducting to 2 K.

Fig. 5 (right). Pressure dependence of the superconducting transition temperature in $TiD_{0.74}$ on compression (circles) and decompression (triangles) [19,39]. The T_c value of quenched χ–$TiD_{0.74}$ [22] is shown with a square.

A possible identity of the phase to another phase stable under high pressure was tested by *in situ* T_c measurements also using the inductance technique [19,39]. Fig. 5 shows that $TiD_{0.74}$ becomes superconducting at 11.8 GPa and its T_c increases upon further compression. The $T_c(P)$ dependence in Fig. 5 extrapolated to normal pressure gives $T_c \approx 4.0$ K, which is much lower than $T_c = 5.0$ K for χ–TiD_n quenched under pressure. Near the pressure of 11.8 GPa, the extension of the direct $\alpha+\delta \rightarrow \zeta$ transition line decreases to a temperature of about 300 K. The *in situ* structural data [19] taken into account, the $\alpha+\delta \rightarrow \zeta$ transition is replaced by the $\alpha+\beta \rightarrow \omega+\eta$ transition at 300 K. Hence, the $T_c(P)$ dependence in Fig. 5 is attributed to a high-pressure phase,

most likely, the η phase. This is also an argument for the individuality of the metastable ρ phase.

Modification of the superconducting properties of χ–$TiH_{0.71}$ due to phase transitions upon heating to the equilibrium state at atmospheric pressure was studied by the resistivity measurements, $\rho(T)$, on the samples subjected to partial annealing runs to temperatures in the range 80 to 270 K [40] (see also Ref. [23]). The results are presented in Fig. 6. Each partial annealing cycle consisted of a slow heating at a rate of about 3 K/min concomitant with the $\rho(T)$ measurements to a maximum temperature of the cycle, T_{ann}, then the sample was cooled to liquid helium in about 1 min. Thus, each curve in Fig. 6 shows a superconducting transition modified due to the change of the sample state in the previous heating run. Though it is difficult to estimate the degree of the transformation from these data, the general trend is as follows. Until $T_{ann} \leq 115$ K, the transition shape does not change and $T_c = 4.26$ K. Higher transformation degrees achieved in further runs result in the decrease of T_c (runs 7 to 12), the appearance of the second step-like anomaly in the $\rho(T)$ curves (runs 13 to 16) and finally, in the suppression of any hints of superconductivity after run 20.

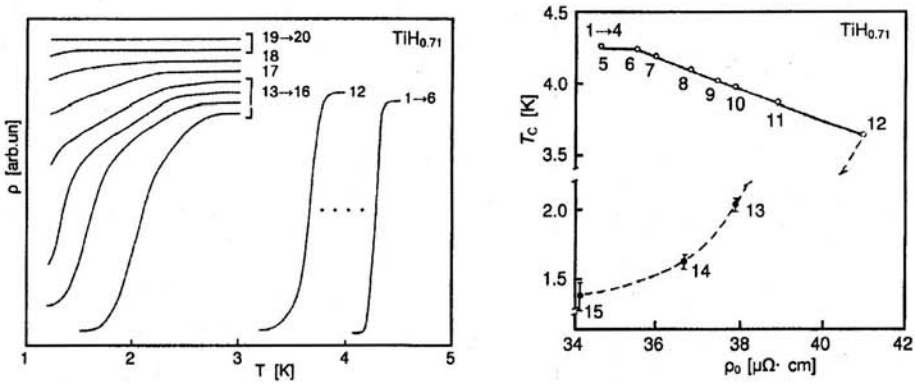

Fig. 6. Degradation of the superconducting transition in quenched χ–$TiH_{0.71}$ in a sequence of annealing runs to temperatures: *1* – 80 K, *2&3* – 89 K, *4* – 102 K, *5* – 106 K, *6* – 115 K, *7* – 124 K, *8* to *10* – 134 K, *11* – 144 K, *12* – 154 K, *13* to *16* – 165 K, *17* – 176 K, *18* – 188 K, *19&20* – 270 K [23,40]. Curves 14 to 20 are shifted upright for convenient comparison. The T_c values are taken at the half-jump of the resistivity.

Fig. 7. Correlation between T_c and the residual resistivity, ρ_0, in the same series of annealing runs as in Fig. 6. Points are labeled according to the curve numbers in Fig. 6. Black points 13 to 15 correspond to the two-step transitions.

Certain regularity was also found in the resistivity behavior in these annealing runs. In Ref. [40], the resistivity was represented as the sum $\rho(T) = \rho_0 + \rho_T$ of the residual resistivity, ρ_0, and the temperature-dependent part, ρ_T. Fig. 7 compares the ρ_0 and T_c changes. The ρ_0 value remained constant in the annealing runs with $T_{ann} \leq 106$ K and markedly increased after the annealing run with $T_{ann} = 106$ K when the T_c value was not yet changed. In further runs with $T_{ann} \leq 154$ K, the ρ_0 values increased by about 20% and then rapidly dropped after heating to 165 K in runs 13 to 16 when the superconducting transition acquired a two-step shape. These changes correlate with the structural behavior of the quenched χ phase upon slow heating, as was observed by real-time neutron diffraction (see below). The initial ρ_0 increase should be related to the hydrogen transition from octa- to tetrasites resulting in the formation of the partially ordered κ phase. Then the hydrogen atoms order in tetrasites to form the γ phase and the residual resistivity decreases.

Fig. 8 presents the ρ_T behavior in this annealing series [40]. The ρ_T/T^2 *vs.* T dependence is linear in wide temperature ranges, $T < 100$ K for runs 1 to 12 and $T < 80$ K for runs 14 to 19. The $\rho_T(T)$ dependence at low temperatures was therefore approximated as $\rho_T(T) = AT^2 + BT^3$. Above the indicated T-limits, the $\rho_T(T)$ curves were different in different runs, which was attributed to the changes in the phase composition of the sample. Parameter A changes from $0.33 \cdot 10^{-3}$ $\mu\Omega$·cm/K^2 for the χ and κ phases to $-0.13 \cdot 10^{-3}$ $\mu\Omega$·cm/K^2 for the heterogeneous mixture of the γ phase with fine-grained Ti precipitates. Teplinsky *et al.* [40] compared the positive AT^2 contribution to the experimental finding by Gurvitch [41] that strongly coupled superconductors acquire the AT^2 resistivity behavior as their disorder increases. The A values in Ref. [41] were of the same order of magnitude as in Ref. [40] or even higher. Negative A values close to the A value for the two-phase γ+Ti sample have been observed in many amorphous alloys [42]. Parameter B varies within ±15% around the mean value of $B = 0.14 \cdot 10^{-4}$ $\mu\Omega$·cm/K^3 for all curves in Fig. 8, that of α–Ti included. It was assumed therefore that the BT^3 contribution is due to the electron scattering on the metal lattice vibrations [40]. This $\rho_T(T)$ behavior is also consistent with the structural changes observed by neutron diffraction [9,10].

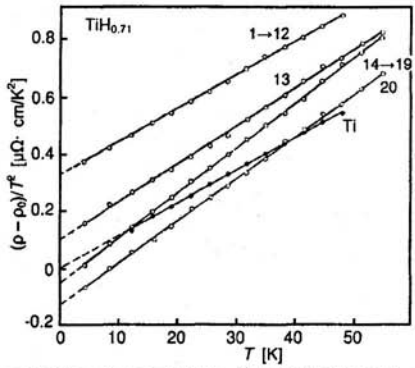

Fig. 8. Variation of the temperature-dependent part, ρ_T, of the resistivity in the same series of annealing runs as in Fig. 6 [40]. The labels at the curves correspond to those in Fig. 6. The curve for polycrystalline α–Ti (99.98 at.% pure; $\rho_{295\,K}/\rho_{4.2\,K} = 8.5$) is presented in black symbols.

Another interesting phenomenon is the enhancement of superconductivity of the Group IV metals due to low-temperature hydrogen implantation [43,44]. The Ti, Zr and Hf films cooled below 12 K [43] or 5 K [44] were irradiated with high-energy H_2^+, D_2^+ or He^+ ions. The implantation resulted in Gaussian-shaped concentration profiles of the implanted atoms with the layers of an about 500 Å width where the concentration was nearly uniform. These thin layers had considerably higher T_c than the initial pure metals. In the case of hydrogen and deuterium implantation, the maximum T_c values were achieved at $n = 0.15 \pm 0.02$. These T_c values are listed in Table 2. In the case of He implantation, the maximum T_c values were much lower if any, and they were achieved at much lower implanted doses.

Table 2. The maximum superconducting transition temperatures of the Group IV metals after hydrogen, deuterium or helium implantation.

	H	D	He	Ref.
Ti	4.95	4.89	<1	[41]
Zr	3.14	4.65	1.49	[40,41]
Hf	1.75	2.23	<1	[41]

The superconducting temperature of the samples with implanted hydrogen or deuterium decreased by 0.5 K after heating to 77 K and became less than 1 K after heating to room temperature. Stritzker and Meyer suggested therefore that the enhanced superconductivity is due to H(D) supersaturation of the *hcp* α-phase at

temperatures when hydrogen diffusion and other equilibrium processes do not occur. This assumption is corroborated by the data of the *in situ* transmission electron microscopy of Ni and Pd hydrides prepared by hydrogen implantation at temperatures below 20 K [45]. In that work, the formation of single-phase hydrides was observed all over the composition range $0 \leq\leq n \leq 1$, contrary to the equilibrium conditions.

Thus, the metastable *hcp* α solid solution supplements the set of superconducting phases obtained in the Ti–H system with the use of high pressure. The metastable *hcp* α–$ZrH(D)_{0.13}$ phase is the only superconducting phase in the Zr–H(D) system. No new phases were found in the study of the *T–P–c* phase diagram of this system at pressures to 7 GPa and temperatures to 900 K [46]. The $T_c(P)$ dependence of ZrD_n samples with $n \leq 0.5$ measured by inductance method at pressures to 43 GPa coincided within the experimental error with that characteristic of the α→ω→β transition sequence in pure Zr [47]. This is a strong argument against the occurrence of new superconducting phases in the Zr–H(D) system at pressures to 43 GPa.

2.3. Phase transformations on heating the χ phase at ambient pressure

The nature of changes in the superconducting properties occurring on heating the quenched χ phase was studied by calorimetry [48] and real-time neutron diffraction [9,10].

Several TiH_n (n = 0.75 and 0.76) and TiD_n (n = 0.69, 0.78 and 0.78) samples were scanned at a heating rate of about 0.5 K/min [48]. The results for each isotope coincided within 3 to 4%. The calorimetric curves are reproduced in Fig. 9. The heat evolution begins around 100°K in hydrides and around 115 K in deuterides; the interval of the transformation is about 100°K. The heat effects are two-peaked with the peak maxima around 130 and 180°K indicating that the transformation is two-staged. The two peaks were separated either graphically or experimentally. The experimental procedure was based on partial annealing runs in the calorimeter until no indication of the low-temperature peak (I) was observed, then the second stage was registered. In this way the heats related to two stages of the transformation were determined, and the activation energies at each stage were estimated from the Arrhenius plots in the temperature intervals where the fraction converted was small, as shown in Fig. 10. The total heat and the individual parameters of two stages of the χ→α+Ti transformation at ambient pressure are listed in Table 3.

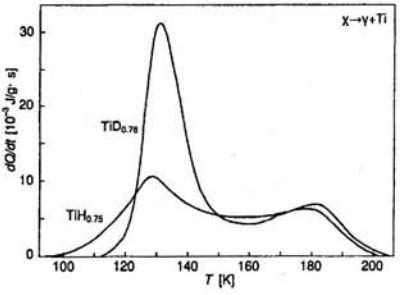

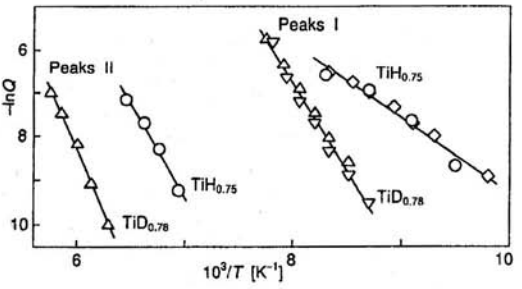

Fig. 9 (left). Heat evolution from χ–$TiH_{0.75}$ and χ–$TiD_{0.78}$ quenched from 600 K at $P = 6$ GPa and heated at a rate of 0.5 K/min [48].
Fig. 10 (right). Arrhenius plots for the low-temperature peak I and the high-temperature peak II of heat evolution from χ–$TiH(D)_n$ represented in Fig. 9 [48].

Table 3. Total heat and the parameters of the low- and high-temperature peaks of the transformation in quenched χ–$TiH(D)_n$ samples on heating at ambient pressure [48].

Phase	n	Total ΔH [J/g]	Peak I		Peak II	
			ΔH_1 [J/g]	E_{a1} [eV]	ΔH_2 [J/g]	E_{a2} [eV]
TiH_n	0.75	71	41	0.15	31	0.37
TiD_n	0.78	119	85	0.35	34	0.48

Almost all data in Table 3 show considerable isotope effects. The E_{a2} energies for hydrides are comparable to the activation energy, $E_a = 0.4$ to 0.5 eV, of hydrogen diffusion in δ–TiH_{2-y} (see [49] and references therein). Recently Wipf *et al.* [50] studied H and D diffusion in the δ phase by mechanical spectroscopy in the temperature range 5 to 400°K and reported the activation energy of $E_a = 0.49$ eV for hydrogen in δ–$TiH_{1.66}$ and $E_a = 0.60$ eV for deuterium in δ–$TiD_{1.64}$. This comparison together with the structural data led to the conclusion that the second stage of the transformation is controlled by hydrogen diffusion in tetrasites of the Ti matrix of the intermediate κ phase [48]. The first stage with even lower activation energies was related to the hydrogen transition from octa- to tetrasites [48], *i.e.* to the $\chi \rightarrow \kappa$ transition. The small E_a values indicate that some potential barriers can be much lowered in the metastable phases.

Fig. 11 presents the neutron diffraction pattern of an isotropic χ–$TiD_{0.73}$ sample quenched from 690°K at 6.5 GPa [29]. The diffraction pattern of the χ phase is characterized by the strong (111) reflection at $d = 2.41$ Å (*fct*). Other intense peaks appear at $d = 1.22$ to 1.29 Å; the {200} and {220} reflections have a zero intensity. The difference between the χ phase and the high-pressure ones is obvious from comparison of the structural and chemical parameters in Table 1.

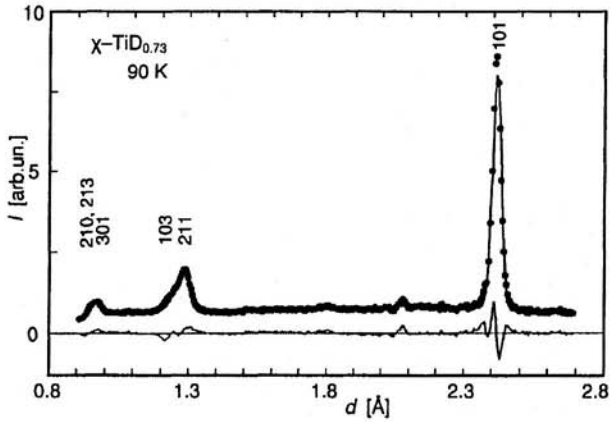

Fig. 11. Neutron diffraction pattern of χ–$TiD_{0.73}$ at $T = 90$°K measured with the DN-2 diffractometer at JINR, Dubna [29]. Shown are the experimental points, the calculated fitting curve and the differential curve. The indices are given for space group *I4/mmm*; *d* is the interspace distance.

The structural changes in quenched χ–$TiD_{0.74}$ during the slow heating to room temperature at a rate of about 1°K/min were studied by means of simultaneous real-time measurements of neutron diffraction and small-angle neutron scattering (SANS) [9,10]. A sequence of the $\chi \rightarrow \kappa \rightarrow \kappa + (\widetilde{\alpha}) \rightarrow \gamma + \widetilde{\alpha}$ phase transformations was observed with the time resolution of 0.5 min. Here $\widetilde{\alpha}$ is the designation of globular metal Ti precipitates whose grain size depends on the heating rate and can be as small as 60 Å, as found in a special SANS study with the PAXE spectrometer at LLB, Sacley [33]. The lattice parameters of the fine-grained Ti precipitates considerably differ from those of bulk Ti metal and gradually recover to the normal values on heating above room temperature [10]. Fig. 12 shows representative spectra of neutron diffraction (left part) and SANS (right part) measured with the DN-2 diffractometer at JINR, Dubna. The intensity and the position of the (111) reflection together with those of the arising (110) superlattice reflection represent the main structural features therefore their variation with temperature is illustrated in Fig. 13.

There were no significant changes in the spectra at temperatures up to 137°K and then the diffraction pattern drastically modified between 142 and 151 K. Peak (111) shifted to larger *d*-values and decreased in intensity by ~5 times meanwhile

superlattice reflections (110) and (112) arose in the pattern. These changes correspond to displacement of the D atoms from octa- to tetrasites concomitant with a partial D ordering on alternate {110} planes and with the increase in the volume of the unit cell, which means formation of the κ phase. Changes in the diffraction spectrum at higher temperatures represent the structural and chemical changes occurring in the κ phase and its further discontinuous transformation to the γ phase.

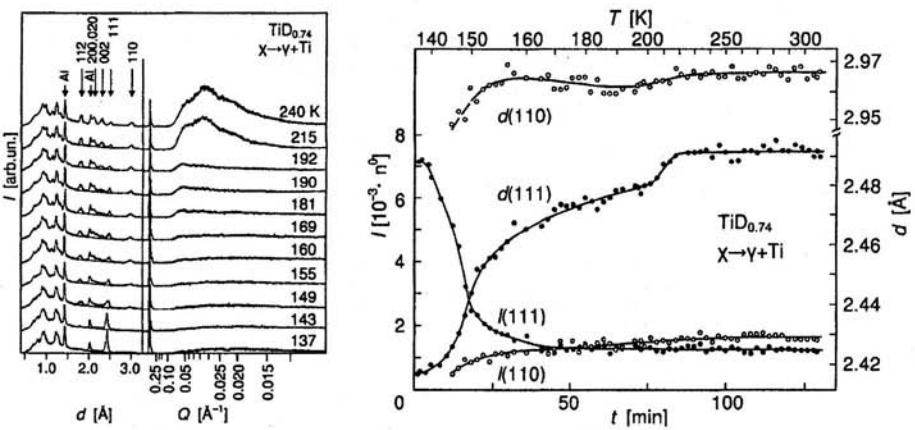

Fig. 12 (left). Evolution of the neutron diffraction (left part) and SANS (right part) spectra illustrating the $\chi \rightarrow \tilde{\alpha} + \gamma$ transformation on a slow heating of χ–$TiD_{0.74}$ [9,10]. The indicated reflections correspond to a distorted *fcc* unit cell. The reflections from the Al cryostat are also marked. The background is partially indicated in the diffraction patterns in order to visualize weak reflections. Q is the neutron momentum transfer; d is the interspace distance. Current temperatures are given on the right.

Fig. 13 (right). Temperature dependences of the intensities I and interspace distances d of the (110) and (111) diffraction peaks in the process of the $\chi \rightarrow \kappa \rightarrow \tilde{\alpha} + \gamma$ transformations in $TiD_{0.74}$ [9,10].

The position of the (110) peak remains nearly the same between 151 and 300 K, this suggests that the lattice parameters a and b of the κ and γ phases vary negligibly in this temperature range. Because $I(110) \sim n^2$, the increase of the (110) intensity by about 1.6 times indicates that the deuterium content in the κ phase increased from 0.74 to 0.94 between 151 and 205 K. The increasing order of the κ phase is connected with a closer packing of deuterium in alternate {110} planes, shortening of the D–D distances along the c-axis and therefore anomalously large increase of $d(111)$ in the temperature interval 151–205 K due to the repulsive D–D interaction. A small jump of the $d(111)$ value between 205 and 220 K is indicative of

a discontinuous κ→γ transition, then the diffraction pattern stays nearly the same up to 300 K. SANS is negligible up to about 180 K while the sample is composed of the χ or κ phase. The increase of the deuterium content of the κ phase with temperature results in the precipitation of deuterium-free titanium particles that gives rise to noticeable SANS starting from 180–200 K. The SANS intensity becomes much stronger at 215 K and higher temperatures, after the transformation of the κ phase to the nearly stoichiometric γ phase.

The neutron scattering and calorimetric data for TiD_n show a good correlation but for a 20 K difference in the temperature ranges of the processes observed. This difference is assumed to be of an experimental nature. The variation of the electrical properties of TiH_n discussed in Section 2.2 is interpreted as follows. The initial increase of the residual resistivity ρ_0 is due to the octa-tetra hydrogen transition. The nucleation of Ti grains as n increases in the ρ phase results in a further increase of ρ_0 and a decrease of T_c. Finally, the precipitation of Ti particles leads to the two-step shape of the superconducting transition, and ρ_0 and ρ_T characterize the highly ordered γ phase matrix incorporating poorly structured fine-grained Ti precipitates. So, the κ phase can be considered as a metastable phase with a wide homogeneity range and the composition-dependent temperature of the superconducting transition.

2.4. Vibrational spectra of the metastable phases

Inelastic neutron scattering (INS) investigation of the vibrational spectra appeared as the most adequate means for understanding the origin of the enhanced superconductivity in the metastable Ti hydrides. Fig. 14 presents the INS spectra of the quenched χ-$TiH_{0.71}$ sample and of the same sample transformed to the γ+Ti two-phase state by heating to ambient conditions [51]. Hydrogen vibrations in octasites of the quenched χ phase form a strong broad peak centered at 75 meV. Its full width at half-maximum is 44 meV. A large width of the peak is indicative of a considerable dispersion of hydrogen vibrations in octasites.

As seen from Fig. 14, the transition of hydrogen from octasites in χ-$TiH_{0.71}$ to tetrasites in γ–TiH results in a shift of the fundamental vibrational band to higher energies. The INS spectrum of γ–TiH was measured with a better resolution using the TFXA spectrometer at ISIS, DRAL (see [18] and references therein). The fundamental band of γ–TiH peaked at 152.7 and 166.7 meV is shown with the short-dash curve in Fig. 15.

Fig. 15 also shows the INS spectrum of $TiH_{0.74}$ measured after a partial χ→κ transition. This partial transition occurred when the sample was allowed to heat in a dry Dewar from 77 to about 100 K during 2 days. It is seen in Fig. 15 that the fundamental band of the partially ordered κ phase is less structured than that of the highly ordered κ phase, and its maximum is at a slightly lower energy of $\omega = 151$ meV.

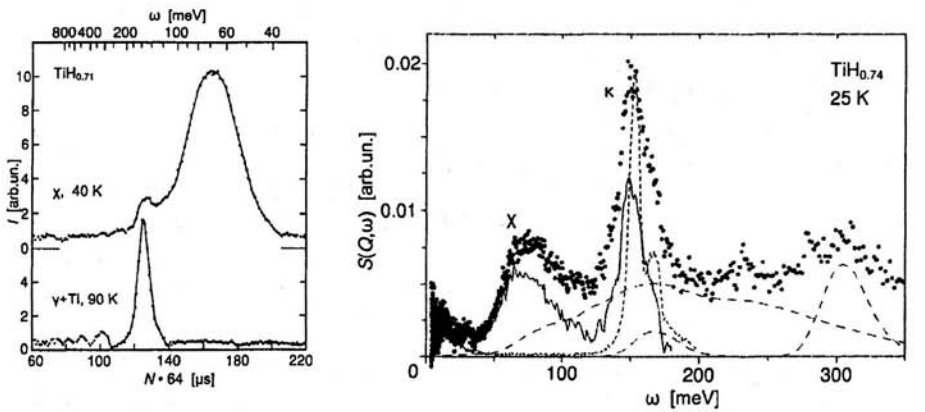

Fig. 14 (left). INS spectra of $TiH_{0.71}$ quenched to the χ phase from 620°K at $P = 6$ GPa (top), then transformed to the γ phase (bottom). The spectra were measured using the KDSOG-M spectrometer at JINR, Dubna, at ambient pressure and the temperatures indicated in the figure. The intensities are normalized to the measuring time [51].

Fig. 15 (right). INS spectrum of a $TiH_{0.74}$ sample composed of a mixture of the χ and κ phase and measured at 25°K with the TFXA spectrometer at ISIS [18]. The one-phonon spectrum (solid line) was obtained as a difference between the experimental data (points) and the multiphonon contributions calculated in the harmonic isotropic approximation (long-dash lines). The short-dash line presents the fundamental band of hydrogen vibrations in γ–TiH.

The most interesting features in the INS spectra of the TiH_n phases were found in the range of low-energy vibrations. Figs. 16 and 17 show the INS spectra of a χ-$TiH_{0.74}$ sample that was first measured as-quenched, then transformed to the κ phase by heating to 151°K directly in the experimental cell and finally converted to the γ+Ti two-phase mixture by heating to room temperature. As seen from Fig. 16, a broad peak at 50 to 90 meV due to the hydrogen vibrations in octasites of the χ phase is no more observed in the spectra of the κ and γ phases. As seen from Fig. 17, the superconducting χ and κ phases demonstrate additional scattering intensity at energies 5 to 9 meV compared to the non-superconducting γ phase. The nature of these low-energy modes is not well understood yet. Kolesnikov *et al.* [52] argued that the modes can be due to hydrogen tunneling within the distorted unit cell.

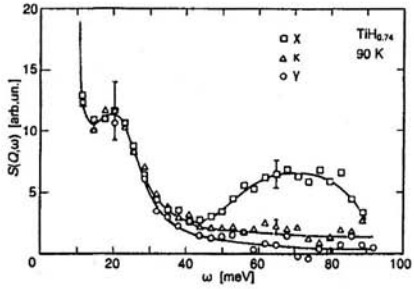

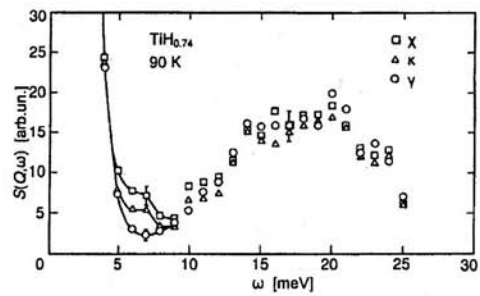

Fig. 16 (left). INS spectra for the χ, κ and γ phases of $TiH_{0.74}$ measured at 90°K with the SV22 spectrometer (DIDO reactor, KFA, Jülich) using neutrons with the incident energy of 102.1 meV [52].

Fig. 17 (right). The low-energy range of the INS spectra for the χ, κ and γ phases of $TiH_{0.74}$ measured with the incident neutron energy of 35.4 meV [52].

The low-energy vibrational modes were used to explain the enhanced superconductivity of the TiH_n phases within the anharmonic two-level model [53]. This model states that the interaction between the low-energy excitations and electrons contributes an additional term, λ_{TLS}, to the constant of the electron–phonon interaction, so that in some cases λ_{TLS} can exceed λ_{ph} due to other coupling mechanisms by an order of magnitude. Drechsler *et al.* [54] assumed tunneling of H(D) ions in α–$ZrH(D)_{0.13}$ and α–$HfH(D)_{0.13}$ prepared by implantation and presented an explanation of the inverse isotope effect in the superconductivity of those solutions using reasonable values of the model parameters. A zero isotope effect in α–$TiH(D)_{0.13}$ was related to probable difference in the type of the interstitials, octa- or tetrasites, occupied by the isotopes, which is not unlikely. Kolesnikov *et al.* [52] and, on deeper theoretical grounds, Galbaatar *et al.* [55] accepted the excitation energy in χ–$TiH_{0.74}$ to be equal to 7 meV and obtained a quantitatively correct value of the isotope effect. The estimated energy $\omega_{TLS} = 2.2$ to 2.3 meV of the low-energy excitations in χ–$TiD_{0.74}$ is nearly the same in both works, but this value has not been tested in experiment.

3. HYDRIDES FORMED UNDER HIGH HYDROGEN PRESSURES

In contrast to the Group IV and V *d*-metals and palladium, other *d*-metals do not form hydrides at low hydrogen pressures. Nevertheless, most these metals absorb significant amounts of hydrogen if the pressure is sufficiently high, see Fig. 18.

α ε $CrH_{1.0}$ af p	α′ ε,γ $MnH_{0.96}$ af af	α ε′,γ,ε $FeH_{1.0}$ f f	ε ε,γ $CoH_{1.0}$ f f	γ γ $NiH_{1.1}$ f p	γ Cu d
α ε $MoH_{1.05}$ sc sc	ε ε $TcH_{0.8}$ sc sc	ε ε $RuH_{0.03}$ sc	γ γ $RhH_{1.0}$ p p	γ γ $PdH_{1.0}$ p sc	γ Ag d
 W sc	ε ε $ReH_{0.22}$ sc sc	ε ε $OsH_{0.003}$ sc	 Ir sc	 Pt p	γ orth $AuH_{0.4}$ d

Fig. 18. Hydrides of *d*-metals synthesized under high hydrogen pressures (see [4,56] for details and references). The maximum hydrogen content achieved is indicated. The arrows show the direction of the changes in the crystal structure and magnetic and superconducting properties of the starting metals on hydrogenation. Metal lattices of the phases are: α = *bcc*, α′ = α-Mn, γ = *fcc*, ε = *hcp*, ε′ = *dhcp*, orth = orthorhombic. Magnetic state at low temperatures: af = antiferromagnetic, f = ferromagnetic, p = paramagnetic, d = diamagnetic, sc = superconductor.

Phase diagrams and crystal and magnetic structures of binary hydrides of the Group VI–VIII transition metals are discussed in the recent review [56] which also provides a list of relevant publications. The hydrides can be briefly characterized as follows.

The hydrides have close-packed metal sublattices with *fcc*, *hcp* or *double hcp* structure, in which hydrogen occupies octahedral interstitial positions. The hydrides are metals and most of them exist in wide composition ranges and can be considered as solid solutions of hydrogen distributed over interstices either randomly or in a superstructure order. Three of the possible structures of binary hydrides are schematically shown in Fig. 19a,b,c. Occupancy of all octahedral interstices in the *hcp* (Fig. 19a) or *fcc* (Fig. 19c) metal lattice corresponds to the H-to-metal atomic ratio of $n = 1$. In some *hcp* hydrides with a lower hydrogen content, the hydrogen atoms form layered superstructures, occupying every third octahedral base layer at concentrations close to $n = 1/3$ (observed in ε-$CoH_{0.34}$) or every second layer at around $n = 1/2$ (ε-$CoD_{0.50}$, ε-$TcH_{0.45}$ and, most likely, ε-$Mn_{0.65}$). In the ordered structures, as shown in Fig. 19b for the case of $n = 1/2$, the metal layers separated by the hydrogen atoms move apart while the layers containing no hydrogen between them move closer together.

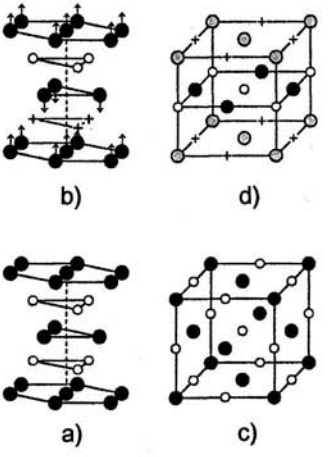

Fig. 19. Crystal structures of high-pressure hydrides: (a) the NiAs type; (b) anti-CdI_2 type; (c) NaCl type; (d) the structure of the ordered PdAgH and PdCuH phase. The crosses and small open circles mark octahedral interstitial positions, respectively, empty and occupied by hydrogen atoms. The large filled circles show positions of metal atoms. The black circles in structure (d) represent Pd atoms, the grey circles Ag or Cu atoms. The arrows in structure (b) indicate the directions of displacements of the metal atoms from the *hcp* positions due to hydrogen ordering.

Compared to phase transformations occurring at high pressures in the Me-H samples with fixed total hydrogen content that were considered in Section 2, synthesis of hydrides in the hydrogen atmosphere is carried out under the conditions approaching those of dynamic equilibrium of hydrogen in the solid and gaseous phase. Incorporation of one more phase, gaseous hydrogen, in the reaction decreases the number of thermodynamic degrees of freedom by one. As a result, the hydrogen content of the metal is no longer an independent variable and its value is determined by the pressure and temperature applied.

Accordingly, only single-phase fields are possible in the *T–P* diagrams of metals in equilibrium with gaseous hydrogen, but the composition of every phase can vary with *T* and *P* within the corresponding field. The *T–P* diagrams of binary Me-H systems constructed at ISSP RAS and also the diagram of the Pd-H system from literature [57] are presented in Fig. 20. The solid lines show the transitions accompanied by a decrease in the hydrogen content of the sample (hydride decomposition), as these lines are much closer to the equilibrium phase boundaries than the lines of hydride formation [58].

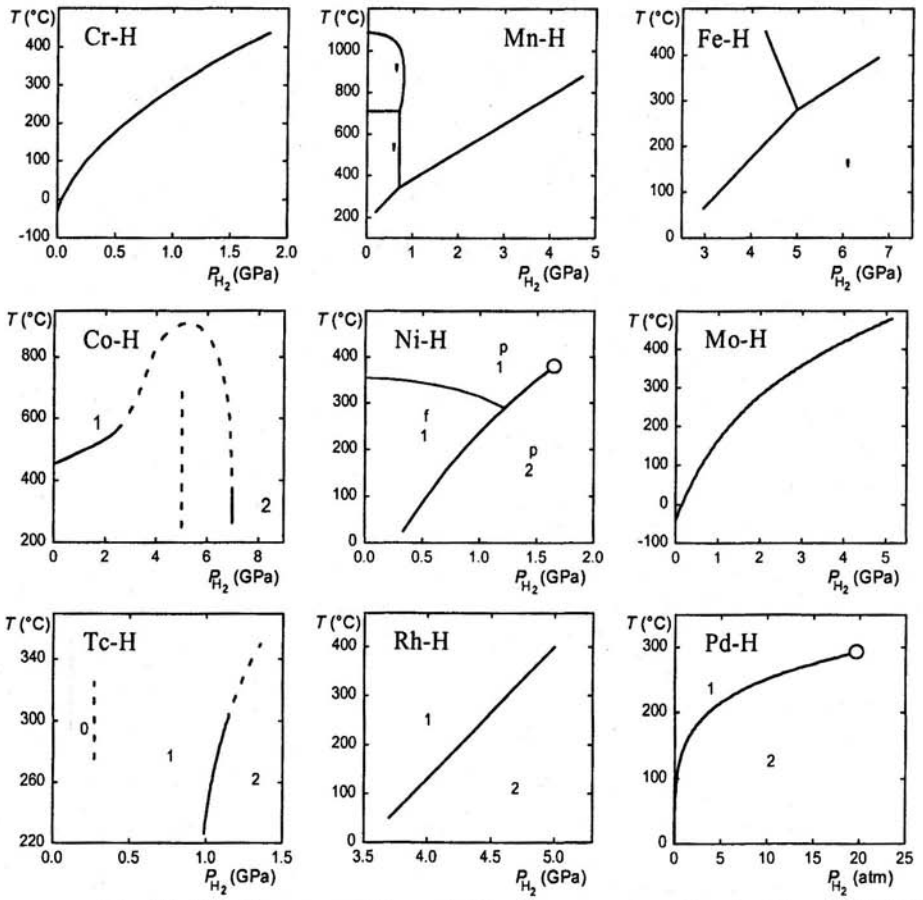

Fig. 20. *T-P* diagrams of the metal-hydrogen systems for the Group VI–VIII transition metals (see [4,56] for details and references). Metal lattices of the phases are: $\alpha = bcc$, $\alpha' = \alpha$–Mn, $\beta' = \beta$-Mn, $\gamma = fcc$, $\varepsilon = hcp$, $\varepsilon' = dhcp$. The subscripts '0', '1' and '2' mark isomorphous phases in the order of increasing hydrogen content. The superscripts 'f' and 'p' mark ferro- and paramagnetic phases, respectively. The dashed portion of the $\varepsilon \rightarrow \gamma$ boundary in the Co-H diagram is tentative. The vertical dashed line in this diagram is a schematic plot of the line of supercritical anomalies of the transformation between the metastable γ_1 and γ_2 phase. The dashed curves in the Tc-H diagram represent the lines of supercritical anomalies of the $\varepsilon_0 \leftrightarrow \varepsilon_1$ and $\varepsilon_1 \leftrightarrow \varepsilon_2$ transformations. The circles in the Ni-H and Pd-H diagrams show the position of the critical point of the $\gamma_1 \leftrightarrow \gamma_2$ transformation (the γ_1 and γ_2 phase in the Pd-H system are usually denoted as the α and β phase, respectively).

Table 4. Composition, superconducting temperature T_c, pressure and temperature of synthesis in a hydrogen or deuterium atmosphere, structure and parameters of the metal sublattice at ambient pressure and 80–100 K for some *d*-metals and their high-pressure hydrides and deuterides. References are given to the papers presenting the superconducting properties.

Components	n = H/Me	T_c [K]	Synthesis		Metal lattice	a [Å]	c [Å]	N^e_{eff} [el./atom Me]	Ref.
			P [GPa]	T [°C]					
Pd	0	$<2\cdot10^{-4}$	—	—	*fcc*	3.887	—	10	[148]
Pd-H	1.0	≈9	>1	20	*fcc*	4.090	—	10.5	[3]
Pd-D	1.0	≈11	>1	20	*fcc*	4.084	—	10.5	
Rh	0	$3.25\cdot10^{-4}$	—	—	*fcc*	3.798	—	9	[149]
Rh-H	1.0	<0.3	7	350	*fcc*	4.024	—	9.5	[61]
Ru	0	0.495	—	—	*hcp*	2.704	4.277	8	
Ru-H	0.035	0.455	9	350	*hcp*	2.705	4.278	8.02	
Tc	0	7.85	—	—	*hcp*	2.735*	4.388*	7	[64]
Tc-H	0.04	7.35		300	*hcp*	2.74*	4.39*	7.02	
Tc-H	0.485	≈0.3 & ≈1.0	0.6	300	*hcp*	2.801*	4.454*	7.25	[66]
Mo	0	0.92	—	—	*bcc*	3.144	—	6	[67]
Mo-H	1.07	0.92	6	325	*hcp*	2.932	4.747	6.54	
Mo-D	1.06	1.11	6	325	*hcp*	2.931	4.747	6.53	
Re	0	1.70	—	—	*hcp*	2.755	4.451	7	[61]
Re-H	0.20	0.7	8	350	*hcp*	2.801	4.465	7.1	
Ni-H	1.06	<0.3	6.5	250	*fcc*	3.737	—	10.53	
V	0	5.40	—	—	*bcc*	3.023	—	5	[102]
V-H	2.0	<0.35	7	325	*fcc*	4.271	—	6	
Nb	0	9.22	—	—	*bcc*	3.300	—	5	
Nb-H	2.0	<0.35	7	325	*fcc*	4.562	—	6	

* The lattice parameters of Tc-H hydrides refer to room temperature.

$N^e_{eff} = N^e + 0.5n$, where N^e is the average number of outer s+d electrons per atom in the starting metal.

3.1. Hydrides of the Group VI–VIII transition metals

None of the Group VI–VIII 3*d*-metals and their hydrides shows superconducting properties. The metals are magnetically ordered at low temperatures and the hydrides of Mn, Fe and Co are also magnetically ordered (Fig. 18). ε-$CrH_{0.97}$ is paramagnetic down to helium temperatures [59,60]. γ-$NiH_{1.06}$ is paramagnetic down to 0.3 K [61].

The Group VI–VIII 4*d*-metals except Pd are superconductors. The basic properties of these metals and their high-pressure hydrides are listed in Table 4. The table also presents similar data for 3*d*-metal Ni and 5*d*-metal Re and for V and Nb metals from Group V. In most cases, the superconducting temperature of the sample was determined from the step midpoint position in the temperature dependence of magnetic susceptibility $\chi(T)$.

Pd-H system. Both palladium and palladium hydride have an *fcc* metal lattice. In a hydrogen atmosphere, palladium hydride is formed via the isomorphous $\gamma_1 \rightarrow \gamma_2$ transition, where γ_1 and γ_2 are the Pd-H solid solutions poor and rich in hydrogen, respectively (these phases in the Pd-H system are usually called the α and β phase). At room temperature, the transition is accompanied by an abrupt increase in the hydrogen solubility from $n \approx 0.01$ in the γ_1 phase to $n \approx 0.61$ in the $_2$ phase [57]. The compositions of the coexisting γ_1 and γ_2 phases get closer to each other with increasing temperature, and the line of the $\gamma_1 \leftrightarrow \gamma_2$ equilibrium terminates at a critical point, as shown in Fig. 20.

A hydrogen pressure of about 0.007 atm is sufficient to form the γ_2 hydride of palladium with $n \approx 0.61$ at room temperature [57], whereas pressures exceeding 1 GPa are necessary to approach $n \approx 1$ [3]. Since the discovery superconductivity in palladium hydrides at $n > 0.8$ [2], a lot of works have been devoted to synthesis and studies of hydrides and deuterides of Pd and its alloys in the range of high H and D concentrations. So far as the $T_c(n)$ dependences for the hydrides and deuterides of pure palladium are concerned, results obtained with samples prepared by different techniques (under a high hydrogen pressure, electrochemically, by hydrogen implantation) are in good agreement with each other [3]. The T_c values of palladium hydrides rise above 1 K at $n \approx 0.8$ and reach 9±0.5 K at $n = 1$. The $T_c(n)$ dependence resulted from averaging the available experimental data will be shown by the dashed line in Figs. 29, 32 and 33. The superconducting temperature of palladium deuterides is higher than that of hydrides at any $n > 0.8$ and reaches $T_c = 11 \pm 0.5$ K at $n = 1$. Palladium hydrides are shown to be type II superconductors with the second critical magnetic field varying at $T = 0$ K from 80 to 250 G depending on the hydrogen content of the hydride and/or on the concentration of lattice defects [3].

An explanation of the increase of T_c with increasing hydrogen content of palladium and also of the "inverse" isotope effect—higher T_c values for the deuterides than for the hydrides—was first proposed by Ganguly [62] and then confirmed by several theoretical and experimental investigations [3]. The Pd-H and Pd-D systems proved to be the first superconductors where the optic phonon modes take part in an effective way in the attractive electron-electron interaction leading to enhancement in

superconductivity. The higher superconducting temperature of the deuterides is due to the weaker force constant between Pd and D than between Pd and H resulting from less anharmonic zero-point vibrations of heavier D atoms [62].

Rh-H system. The hydrogen content of the primary γ_1 solutions does not exceed $n = 0.01$ and the composition of the γ_2 hydride is close to RhH throughout the stability regions of these phases in the *T–P* phase diagram studied so far (Fig. 20). Samples of polycrystalline rhodium (99.98%) and its hydride were shown to be non-superconducting at $T \geq 0.3$ K [61].

Ru-H system. The equilibrium hydrogen solubility in *hcp* ruthenium at 250°C monotonically increases with pressure and reaches $n \approx 0.03$ at 9 GPa [63]. To estimate the effect of hydrogen on the superconducting temperature of Ru metal [61], a single crystal of ruthenium was grown from Ru powder (99.96%) and loaded with hydrogen at 9 GPa and 350°C. The hydrogen content of the sample reached $n = 0.035 \pm 0.01$ that resulted in the decrease of its T_c from 0.495 K to 0.455 K. After removal of the hydrogen by annealing in vacuum at 500°C, the superconducting temperature of the sample increased to the initial value of 0.495 K. The reversibility of the T_c changes suggests that the observed decrease in the superconducting temperature of the Ru sample was due to the dissolved hydrogen rather than the defects introduced in the course of the high-pressure treatment. The initial slope of the $T_c(n)$ dependence is of the order of -1 K/H atom.

Tc-H system. At high pressures, the system undergoes two isomorphous phase transitions, $\varepsilon_0 \rightarrow \varepsilon_1$ and $\varepsilon_1 \rightarrow \varepsilon_2$. The lines of both transitions terminate in the critical points at $T < 300$°C (Fig 20). At 300°C, the equilibrium hydrogen solubility in Tc is $n \approx 0.5$ at 0.7 GPa and $n \approx 0.8$ at 2 GPa (Fig. 21). The Tc-H samples prepared under high hydrogen pressure and elevated temperature do not loose hydrogen at ambient conditions for periods of months. Phase compositions of such samples correspond to the equilibrium at fixed total hydrogen content. In particular, the X-ray diffraction study at room temperature revealed a miscibility gap between the range $0 < n \leq 0.04$ of the primary ε_0-solutions and the range $0.385 \leq n \leq 0.78$ of the ε-hydrides [64]. The neutron diffraction investigation at 300 K and 120 K demonstrated [65] that hydrogen is randomly distributed over octahedral interstices in $TcH_{0.69}$ with the deficient NiAs-type structure shown in Fig. 19a and forms a layered superstructure of the anti-CdI_2 type (Fig. 19b) in $TcH_{0.45}$.

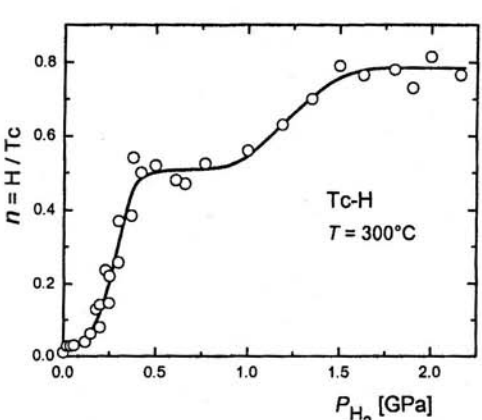

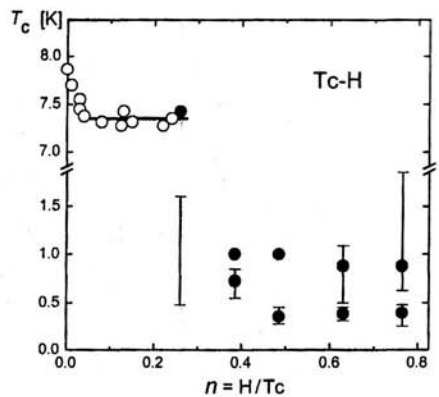

Fig. 21 (left). Hydrogen solubility in technetium at 300°C [64].
Fig. 22 (right). Superconducting temperature T_c as a function of the hydrogen content n = H/Tc of Tc-H samples [66]. The horizontal portion of the $T_c(n)$ dependence at $0.04 < n < 0.385$ is due to the constant hydrogen content $n \approx 0.04$ of the ε_0-phase in the two-phase mixtures $\varepsilon_0 + \varepsilon$ formed in this concentration interval.

As seen from Fig. 22, the superconducting temperature of the ε_0-solutions monotonically decreases with increasing hydrogen content from 7.85 K for initial technetium to ≈7.35 K at $n = 0.04$. The Tc-H samples with $n \geq 0.385$, which should have been single-phase ε-hydrides according to the X-ray and neutron diffraction data, also proved to be superconducting. However, in their $\chi(T)$ dependences (Fig. 23) there were two steps characteristic of superconducting transitions. Fig. 22 shows the intervals of those transitions estimated at the level 95% of the step height. As one can see, the temperature intervals of superconducting transitions are minimum for the sample with $n = 0.485$ and increase on moving away from this composition towards lower or higher hydrogen concentrations.

Two superconducting transitions in the Tc-H samples with $n \geq 0.385$ evidence the presence of two superconducting phases with different values of T_c. The X-ray investigation of the sample with $n = 0.485$ showed no signs of a phase transition in its metal lattice on cooling from 300 K to 7 K [66]. The occurrence of a phase transition in the hydrogen sublattice that cannot be detected by X-rays was therefore concluded to be the most plausible explanation for the decomposition of the single-phase ε-hydrides to two different phases at low temperatures.

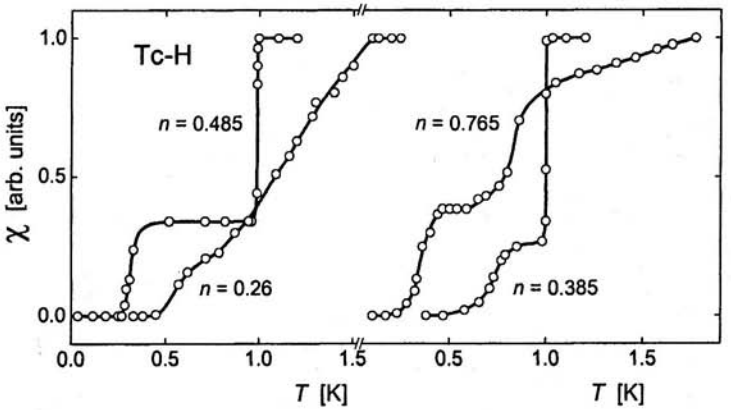

Fig. 23. Temperature dependences of the magnetic susceptibility χ for samples of technetium hydrides with the indicated H/Tc ratio of n [66]. In the $\chi(T)$ dependence for the two-phase ($\chi_0 + \chi$) sample with $n = 0.26$, there is one more step at $T = 7.42$ K corresponding to the superconducting transition in the α_0-phase.

Mo-H system. The hydrogen solubility in *bcc* (α) molybdenum is small. The composition of the *hcp* (ε) hydride is close to MoH irrespective of the pressure and temperature of synthesis within the region of the hydride stability on the *T–P* diagram shown in Fig. 20.

A single crystal of Mo with the resistance ratio $R_{300\,K}/R_{4.2\,K} \approx 1000$ was used as the starting material to synthesize hydride and deuteride samples for the studies on superconductivity [67]. The hydride and deuteride samples obtained were polycrystalline because their formation was a polymorphic transition accompanied by an about 17% increase in the sample volume. Both the hydride and deuteride proved to be superconductors. The hydride has the same $T_c = 0.92$ K as pure Mo, while the T_c value of the deuteride is about 0.2 K (*i.e.* 20%) higher (Fig. 24).

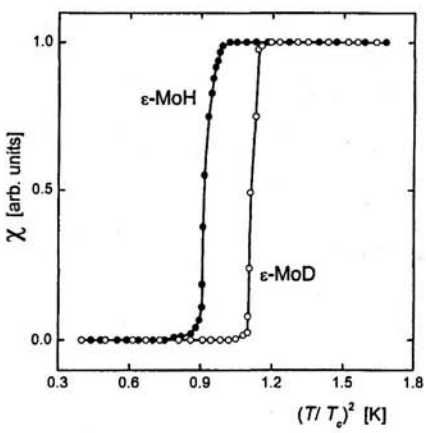

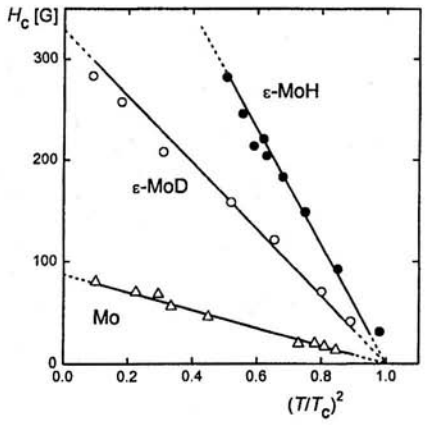

Fig. 24 (left). Temperature dependences of the magnetic susceptibility in the vicinity of superconducting transition in molybdenum hydride and deuteride [67].

Fig. 25 (right). Critical magnetic field H_c *vs.* the square of reduced temperature for the molybdenum single crystal and for the polycrystalline molybdenum hydride and deuteride [67].

The critical field H_c of Mo, MoH and MoD samples was estimated from the position of the step of the $\chi(H)$ isotherms in fields H up to 280 G. As seen from Fig 25, the temperature dependences of H_c are described satisfactorily by the familiar expression $H_c(T) = H_c(0)\cdot[1 - (T/T_c)^2]$. The extrapolated values of $H_c(0)$ vary from ≈90 G for the initial single-crystalline Mo to ≈300 G for the polycrystalline ε-MoD and to ≈600 G for the ε-MoH. After removal of H or D from the MoH and MoD samples by vacuum annealing at 500°C for 30 min, the resulting polycrystalline sample of Mo had T_c = 0.92°K and $H_c(0)$ ≈ 120 G. Some increase in $H_c(0)$ for molybdenum, from about 90 to 120 G, after the hydrogenation/dehydrogenation cycle was due to the lattice defects and residual stresses created by this procedure.

By analogy with palladium [3], the "inverse" isotope effect—a higher superconducting temperature for the deuteride than for the hydride—in the case of molybdenum could also be attributed to the considerable contribution of optical phonons into the electron-electron coupling and the weaker anharmonicity of optical vibrations of the D atoms compared to the H atoms. It seems worth noting, however, that the fundamental peak of optical H vibrations in ε-MoH lies at 114 meV [68], which is approximately twice as high as that of 56 meV in γ-PdH [69]. Correspondingly, the influence of optical H vibrations on the superconducting properties of molybdenum hydride should not be as strong as in palladium hydride.

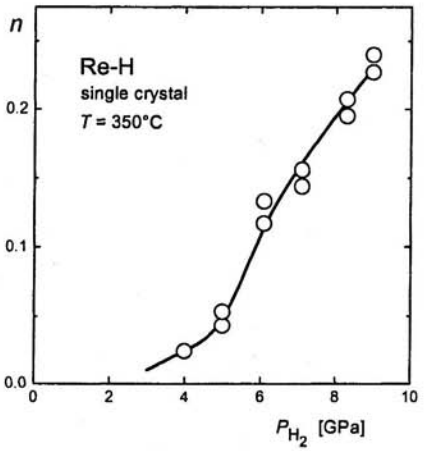

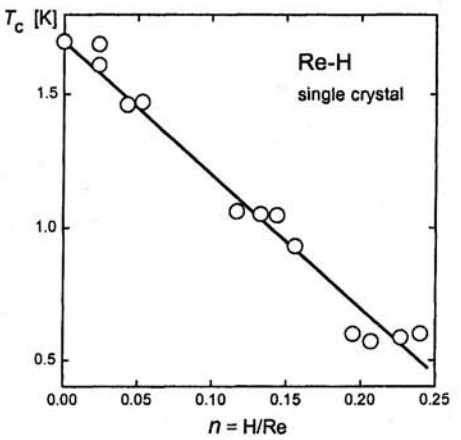

Fig. 26 (left). Hydrogen solubility in *hcp* rhenium metal at 350°C [61].
Fig. 27 (right). Superconducting temperature T_c as a function of the hydrogen content n = H/Re of Re-H solid ε-solutions [61].

Re-H system. At 170–350°C, the equilibrium hydrogen solubility in *hcp* rhenium monotonically increases with pressure and reaches $n \approx 0.23$ at 9 GPa and 350°C (Fig. 26). To study the concentration dependence of T_c for Re-H solid solutions, single-crystalline Re-H samples were prepared from a single crystal of Re with the resistance ratio $R_{300\,K}/R_{4.2\,K} \approx 100$ and $T_c = 1.70$ K [61]. As seen from Fig. 27, incorporation of hydrogen into rhenium metal results in an approximately linear decrease in the T_c values with the slope $dT_c/dn = -5.0 \pm 0.2$ K/H atom. The temperature interval of the superconducting transition remains sufficiently narrow (Fig. 28) that points to a homogeneous distribution of hydrogen over the metal volume. After removal of hydrogen from the Re-H samples by annealing in vacuum at 500°C, the superconducting temperature increased to the initial value of 1.70 K of the rhenium crystal used.

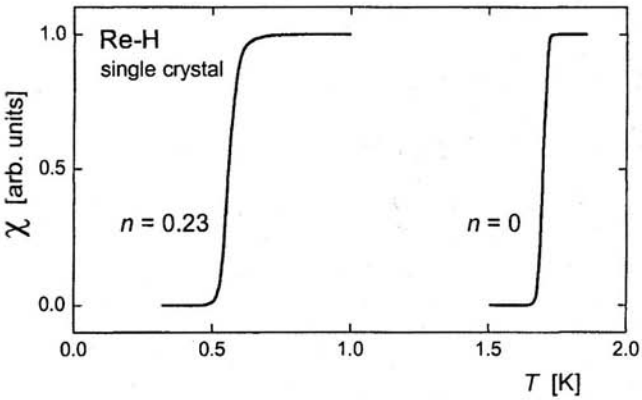

Fig. 28. Temperature dependences of the magnetic susceptibility χ in the vicinity of the superconducting transitions in the initial Re sample (n = 0) and in the Re-H solid solution with n = 0.23 [61].

3.2. Hydrides of Pd alloys with noble metals

3.2.1. *Superconductivities of hydrides produced by hydrogen implantation and under a high hydrogen pressure*

Soon after the discovery of superconductivity in the Pd-H solid solutions with $n > 0.8$ [2], Stritzker found out [70] that implantation of hydrogen in alloys of palladium with noble metals (Cu, Ag and Au) cooled to helium temperatures made them superconductors with T_c values of up to 13–17°K much exceeding $T_c \approx 9$°K attainable for the Pd-H solutions [3]. Stritzker's discovery gave strong incentive to the experimental investigations of superconducting properties of hydrogen solutions in palladium alloys with various metals: Ni [3,71–73], Fe and Cr [74], Ti [3], Rh [3,75,76]. Pt [3,76], Al [3,77,78], In [78] and B [79]. None of those solutions, however, had as high values of T_c as hydrogen solutions in the alloys of palladium with noble metals. Stritzker's results for such solutions were later confirmed in the work of Ref. [78], where implantation of hydrogen into a $Pd_{50}Cu_{50}$ alloy induced superconductivity with $T_c \approx 13$°K.

Hydrogenation of Pd alloys with noble metals under high hydrogen pressures at ISSP RAS gave quite different results. The $Pd_{80}Ag_{20}$ and $Pd_{60}Cu_{40}$ alloys with the compositions close to the optimum ones for achieving the highest values of T_c by hydrogen implantation were loaded with hydrogen at 250°C and hydrogen pressures up to 7 GPa [80]. The T_c values of the hydrogen solutions thus obtained are presented in Fig. 29. The $Pd_{60}Cu_{40}$-H solutions with the hydrogen content up to $n = 0.61$ are not superconducting at $T \geq 2$°K, while the $Pd_{60}Cu_{40}$ alloy with the same concentration of implanted hydrogen should have T_c no less than 6–10°K, as illustrated by the $T_c(n)$ dependence [70] for the $Pd_{55}Cu_{35}$ alloy of a similar composition. Implantation of hydrogen into the $Pd_{80}Ag_{20}$ alloy should result in $T_c \approx 15$°K at $n = 0.8$ [70]. As seen from Fig. 29, the superconducting temperature of the $Pd_{80}Ag_{20}$-H solutions produced

under high hydrogen pressures is below 4 K at $n = 0.8$ and it does not rise above 7.5°K even at $n \approx 1$. On the whole, the $T_c(n)$ dependences for these solutions do not differ much from the dependence for the Pd-H solutions averaged through the results of different authors and shown in Fig. 29 by the dashed line.

So far as theory is concerned, there had been no generally adopted viewpoint as to how the alloying of palladium with noble metals should affect the superconducting temperature of the hydrides. For example, according to the theoretical estimates of Refs. [81–83], this alloying should increase T_c. On the other hand, the theoretical results of Ref. [84] and the estimates made in Ref [85] based on the experimental investigation of the low-temperature specific heat of non-superconducting $Pd_{80}Ag_{20}$-H solutions indicated that T_c should decrease. The experimental study of superconducting $Pd_{80}Ag_{20}$-H solutions prepared under high pressures demonstrated [80] that such an alloying nearly does not affect the superconductivity of palladium hydrides at all.

The high T_c values of the Pd-noble metal-H samples prepared by hydrogen implantation at helium temperatures [70,78] could be due to specific radiation defects and to a significant instability of the crystal structure formed. An important role that radiation defects could play follows, in particular, from another experimental result of Stritzker. He showed [86] that Pd films became superconductors with the critical temperature of up to 3.2°K after irradiation at low temperatures with He^+ ions, accelerated to the energy high enough for the ions went all the way through the films without sticking inside. The author [86] ascribed the effect to suppression of strong spin fluctuations, which are thought to be the reason for the absence of superconductivity in Pd metal [87].

It should be noted, however, that the maximum values of T_c achieved with the Pd-H and Pd-D samples prepared by implantation virtually coincided with those of nearly defect-free samples prepared under high hydrogen or deuterium pressures [3]. By contrast, the samples of hydrides of palladium-noble metal alloys with implanted hydrogen had much higher T_c values than the samples with the same composition loaded with hydrogen under high pressures. The implantation being expected to produce similar radiation defects both in Pd and Pd-noble metal alloys, another factor should be responsible for further enhancement of superconductivity of the Pd-noble metal alloys. Most likely, it is instability of the crystal structure, which is specific for these very alloys with implanted hydrogen and manifests itself in a softening of some phonon modes and in the corresponding strengthening of the electron-phonon coupling.

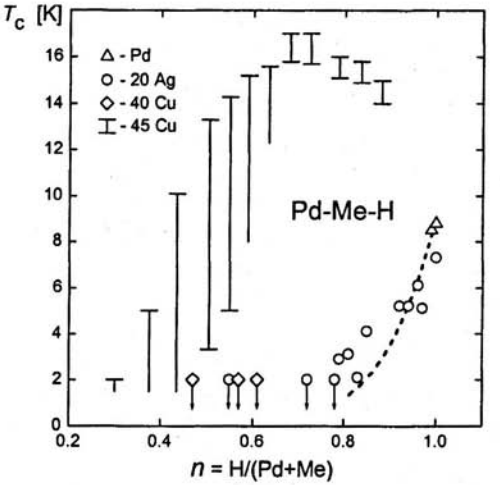

Fig. 29. Superconducting temperature T_c as a function of the hydrogen content n = H/(Pd+Me) for solid solutions of hydrogen in *fcc* palladium and its alloys with Ag and Cu [4]. Palladium [4] and the $Pd_{80}Ag_{20}$ and $Pd_{60}Cu_{40}$ alloys (at.%) [80] were loaded with hydrogen under a high pressure. The symbols with arrows indicate the absence of superconductivity at $T \geq 2$°K. The $Pd_{55}Cu_{45}$-H solutions were prepared by hydrogen implantation [70]. The vertical bars show the temperature intervals, in which the sample resistance dropped from 90 to 10% of the residual resistance of the normal phase. The dashed line presents the T_c vs. n dependence for Pd-H solutions [3].

Formation of a highly unstable crystal structure as the main reason for the high T_c values of the Pd-noble metal-H solutions was first suggested by Stritzker [70]. He observed clear signs of lattice instability while studying the dependences of T_c *vs.* the dose of hydrogen implanted in the Pd-Cu and Pd-Ag alloys with compositions close to the optimum ones for achieving the maximum $T_c > 15$°K. A monotonic increase of T_c with increasing dose of implanted hydrogen was sometimes interrupted and T_c dropped below 1°K. The disappearance of superconductivity was also accompanied with a sudden drop of the residual resistance R_{res} by 10–20%. Further hydrogen implantation led to a monotonic decrease in R_{res}, but superconductivity never reappeared. Stritzker explained this by the formation of a new non-superconducting phase with a smaller value of R_{res}.

3.2.2. *Superstructures in the Pd-Cu-H and Pd-Ag-H systems*

Studies carried out at ISSP RAS have shown that disordered *fcc* alloys of Pd with Cu and Ag placed in a hydrogen atmosphere at pressures up to 7 GPa and temperatures up to 100–150°C form non-stoichiometric γ-hydrides with a deficient NaCl-type structure (Fig. 19c). The achievable concentration of hydrogen atoms chaotically distributed over octahedral interstices in the metal lattice decreases with decreasing Pd concentration of the alloys from $n \approx 1$ for pure Pd to $n \approx 0.5$ for the alloys containing 50 at.% Pd. At temperatures of synthesis exceeding 150–200°C, a new irreversible phase transformation accompanied by a tetragonal distortion of the *fcc* metal lattice was observed in the $Pd_{60}Cu_{40}$-H [88] and $Pd_{50}Ag_{50}$-H [89] systems. Tetragonal samples of $PdAgH_{0.90}$ hydride synthesized at 200°C and 2.8 GPa [90] and of $PdCuH_{0.84}$ hydride synthesized at 325°C and 3 GPa [91] were studied by neutron diffraction and shown to be atomically ordered. The ordered structure of these hydrides (γ^{or} hereafter) with the compositions close to the stoichiometry PdMeH is presented in Fig. 19d and consists of layers ...–Me–PdH–Me–PdH–... stacked perpendicular to the tetragonal axis with the hydrogen atoms on the octahedral sites within the Pd layers. The only difference between the structures of the two hydrides was that $PdAgH_{0.90}$ had $c/a > 1$ while $PdCuH_{0.84}$ had $c/a < 1$.

The ordered state of the metal lattice of the $Pd_{60}Cu_{40}$-H [88] and $Pd_{50}Ag_{50}$-H [89] hydride is retained after the complete removal of hydrogen by annealing in vacuum at 250–300°C, though its degree of tetragonality decreased. The lattice turns back to the initial disordered *fcc* after a vacuum annealing at 350–375°C or plastic deformation at room temperature. These results show that the layered superstructure formed in the $Pd_{60}Cu_{40}$ and $Pd_{50}Ag_{50}$ alloys at high hydrogen pressures is not an equilibrium property of the alloys in the absence of hydrogen. The ordered state corresponds to the full (including each sort of the atoms) thermodynamic equilibrium in the Pd-Cu-H and Pd-Ag-H system at high hydrogen pressures.

Both ordered and disordered $Pd_{50}Ag_{50}$-H solutions with the hydrogen content up to $n \approx 0.5$ are not superconducting at $T > 2$°K [89]. The $Pd_{80}Ag_{20}$ alloy forms with hydrogen only disordered γ-solutions at pressures up to 6.7 GPa and temperatures up to 400°C [89] and the $T_c(n)$ dependence in Fig. 29 presents the results for these very disordered solutions.

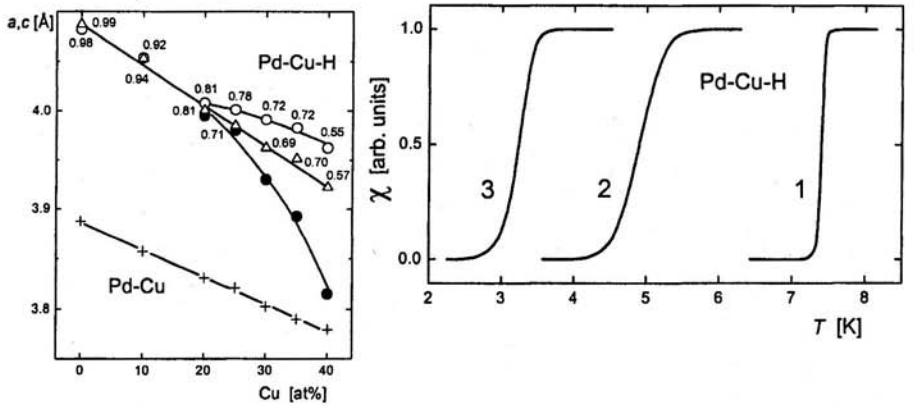

Fig. 30 (left). Parameters a and c of the metal lattice determined by X-ray diffraction at ambient pressure and 80 K for the initial *fcc* Pd-Cu alloys (crosses) and for the Pd-Cu-H solid solutions synthesized by a 24 h exposure to a hydrogen pressure of 2 GPa at 100°C (open triangles) and at 300°C (open and closed circles) [92]. The closed circles show the c-parameter of the tetragonal lattice of the ordered γ^{or}-solutions, the other symbols stand for the a-parameters of both the disordered *fcc* and the ordered tetragonal lattices. The numbers placed near the symbols indicate the hydrogen content of the samples in the units of the H/(Pd+Cu) atomic ratio.

Fig. 31 (right). Temperature dependences of the magnetic susceptibility χ in the vicinity of superconducting transitions in: (1) $Pd_{90}Cu_{10}$ γ-sample, $n = 0.94$; (2) $Pd_{75}Cu_{25}$ γ-sample, $n = 0.94$; (2) $Pd_{75}Cu_{25}$ γ^{or}-sample, $n = 0.86$ [92].

The influence of the atomic ordering on T_c was studied for the Pd-Cu-H system [92]. Using disordered *fcc* Pd-Cu alloys containing 10, 20, 25, 30, 35 and 40 at.% Cu as the starting materials, two series of hydrides were prepared by a 24 h exposure to a high hydrogen pressure at two different temperatures, 100 and 300°C. To illustrate the effect of hydrogenation, Fig. 30 presents X-ray data for the samples prepared at a pressure of 2 GPa. As is seen, the composition range of the ordered γ^{or} solutions at 300°C is rather wide, and even the $Pd_{80}Cu_{20}$-H solution with $n = 0.81$ still exhibits a noticeable tetragonal distortion of the lattice, though the ordering conforms to the PdCuH stoichiometry. However, the diffraction lines of the γ^{or}-samples containing 30, 25 and 20 at.% Cu were considerably broadened that points to their concentration inhomogeneity. Diffraction lines on the X-ray patterns of γ-hydrides of these alloys prepared at 100°C were broadened too, and the linewidths increased when the time of synthesis was increased from 24 to 72 h. This broadening was due to the concentration inhomogeneity of the samples arising at the initial stage of the ordering process, which could not develop farther because of the sluggish kinetics.

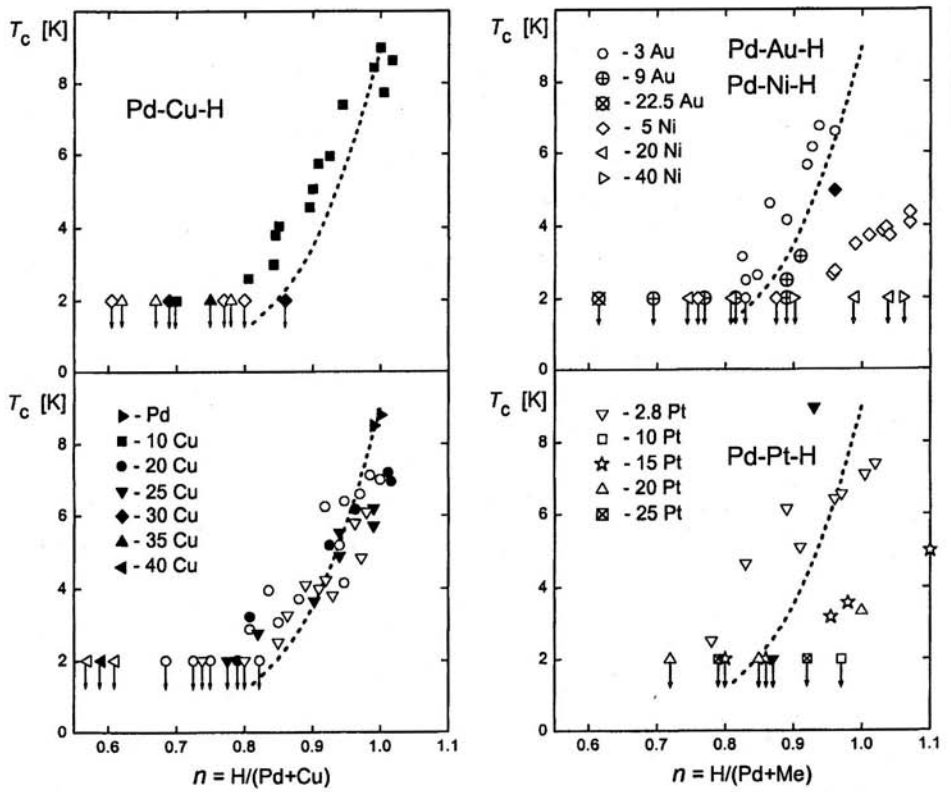

Fig. 32. Superconducting temperature T_c as a function of the hydrogen content n = H/(Pd+Cu) for the disordered γ-solutions (closed symbols) and for the ordered γ^{or}-solutions (open symbols) of hydrogen in Pd-Cu alloys [92]. The symbols with arrows indicate the absence of superconductivity at $T \geq 2$ K. The dashed line presents the T_c vs. n dependence for the Pd-H γ-solutions [3].

Fig. 33. Superconducting temperature T_c as a function of the hydrogen content n = H/(Pd+Me) for single-phase solid solutions of hydrogen in *fcc* palladium and its alloys with Au [93], Ni (the open symbols show results of Ref. [94], the closed diamond is for the sample with 5 at.% Ni measured in Ref. [72]) and Pt (the open symbols show results of Ref. [95], the closed circles are for the samples with 2.8 at.% Pt measured in Ref. [76]). The dashed line presents the T_c vs. n dependence for the Pd-H γ-solutions [3].

Three representative dependences of the magnetic susceptibility in the range of superconducting transitions in the Pd-Cu-H hydrides are presented in Fig. 31. The concentration inhomogeneity of the $Pd_{75}Cu_{25}$-H samples causes a broadening of the

steps of their $\chi(T)$ dependences. The dependences for the $Pd_{80}Cu_{20}$-H solutions look similar.

Fig. 32 shows the T_c values of the Pd-Cu-H solutions studied. Within experimental scatter, the atomic ordering does not change the $T_c(n)$ dependences of the Pd-Cu-H solutions, and all the dependences are close to that for the hydrogen solutions in pure palladium. This result suggests, in particular, that the ordered γ^{or} state of the Pd-Cu-H and Pd-Ag-H solutions is different from the state with high T_c values formed on hydrogen implantation (discussed in Section 3.2.1).

The Pd-Au-H system was studied in Ref. [93]. No atomic ordering was detected in the initially disordered *fcc* Pd-Au alloys containing 3, 9, 22.5, 50 and 75 at.% Au after their hydrogenation at pressures up to 6.7 GPa and temperatures from 200–350°C. The T_c values for the γ-solutions of hydrogen in the alloys with 3.9 and 22.5 at.% Au are shown in Fig. 33.

3.3. Hydrides of Pd-Ni and Pd-Pt alloys

While hydrides in the Pd-Cu-H and Pd-Ag-H systems showed a clear tendency to atomic ordering, hydrides in the Pd-Ni-H [94] and Pd-Pt-H [95] systems demonstrated the opposite tendency to decomposing into phases rich and poor in palladium.

3.3.1. *Pd-Ni-H system*

Pd and Ni form a continuous solid solution with a disordered *fcc* structure. Alloying Pd with Ni results in the occurrence of ferromagnetism at 2.5 at.% Ni and further monotonic increase in the Curie temperature and spontaneous magnetization of the ferromagnetic alloys. In a hydrogen atmosphere, both palladium and nickel hydrides are formed via the isomorphous $\gamma_1 \rightarrow \gamma_2$ transition, where γ_1 and γ_2 are the solutions poor and rich in hydrogen, respectively, see Fig. 20.

Experiments with Pd-Ni-H samples charged with hydrogen by implantation at helium temperature [3] and electrolytically at 200 K [73] showed that the maximum value T_c^{max} of the superconducting temperature achievable on hydrogenation rapidly decreases with increasing Ni concentration, and the samples containing more than 10 at.% Ni never become superconducting at $T > 1$ K. This is exactly the result one could expect from the alloying with a ferromagnetic Ni metal. Interestingly, the dependence of T_c^{max} on the Ni concentration in the nickel-rich Pd-Ni alloys loaded with hydrogen under a high hydrogen pressure and room temperature demonstrated a quite different behavior [71,72]: a deep minimum at ≈10 at.% Ni was followed by a pronounced maximum ($T_c^{max} \approx 10$ K) at ≈20 at.% Ni, and then the T_c^{max} values decreased sharply again.

The X-ray investigation of Pd-Ni alloys with 5, 20, 40, 60 and 80 at.% Ni hydrogenated at hydrogen pressures and temperatures from 20 to 350°C has shown [94] that at $T < 250$°C only γ-solutions are formed in the Pd-Ni-H system, and the line

of the isomorphous $\gamma_1 \leftrightarrow \gamma_2$ transformation moves monotonically towards higher pressures with increasing Ni content of the alloys. At $T > 250$°C, the γ_2-solutions (hydrides) based on the alloys with 20–80 at.% Ni decompose into γ-hydride of nearly pure nickel and γ-hydride of palladium with a few atomic percent Ni. The two-phase state of such samples is retained after the complete removal of hydrogen by vacuum annealing at $T \leq 350$°C. Annealing in vacuum at $T > 400$°C or plastic deformation of hydrogen-free samples at room temperatures brings the alloys back to the starting single-phase homogeneous state. Separation into phases enriched and depleted in palladium thus is not an equilibrium property of Pd-Ni alloys under ambient conditions. This is the property of the ternary Pd-Ni-H system.

As seen from Fig. 33, the T_c values of single-phase samples of the $Pd_{95}Ni_5$-H γ_2-solutions prepared in Ref. [94] lie significantly lower than those of the Pd-H solutions, while the $Pd_{80}Ni_{20}$-H and $Pd_{60}Ni_{40}$-H γ_2-solutions are not superconducting at $T \geq 2$ K. This agrees with the results of Refs. [3,73] for the samples charged with hydrogen by implantation or electrolytically. The high T_c values observed in Refs. [71,72] for the high-pressure Pd-Ni-H samples with the Ni concentrations around 20 at.% cannot be explained unambiguously as the crystal structure of the samples was not examined. Nevertheless, in view of the phase separation observed in the Pd-Ni-H system at elevated temperatures [94], it is plausible to assume that the Pd-Ni-H samples with ~20 at.% Ni prepared in Refs. [71,72] at room temperature could also consist of a mixture of a palladium-rich and palladium-depleted phase, and the palladium-rich phase was superconducting.

3.3.2. *Pd-Pt-H system*

Alloying of Pd with approximately 14 at.% Pt decreases the critical temperature of the $\gamma_1 \rightarrow \gamma_2$ transformation in the Pd-Pt-H system below 25°C, and the equilibrium hydrogen solubility in the *fcc* Pd-Pt alloys with a higher platinum concentration is a continuous function of pressure at room temperature [96]. The hydrogen solubility in Pd-Pt alloys at room temperature and pressures up to 2.4 GPa has been studied in detail in Ref. [97] and shown to decrease monotonically at any given pressure with increasing Pt concentration. Hydrogenation of *fcc* Pd-Pt alloys containing 2.8, 10, 15, 20, 25, 40 and 60 at.% Pt at pressures to 6.5 GPa and $T < 250$°C resulted in the formation of single-phase homogeneous γ-solutions [95]. Hydrogenation of the alloys containing ≥15 at% Pt at $T \geq 250$°C led to the decomposition of the Pd-Pt-H solutions into hydride of palladium with a few atomic percent Pt and a nearly hydrogen-free alloy with the composition close to $Pd_{25}Pt_{75}$. After removal of hydrogen by annealing in vacuum at 300°C, all the Pd-Pt samples recovered their initial homogeneous state.

The T_c values of single-phase samples of the Pd-Pt-H γ-solutions prepared in Ref. [95] are presented in Fig. 33. As seen from the figure, the variation of the $T_c(n)$ dependence with increasing platinum concentration in the Pd-Pt alloy is nonmonotonic. The superconducting temperature of the $Pd_{97.2}Pt_{2.8}$-H solutions reaches 7.4 K at $n \approx 1$; the $Pd_{90}Pt_{10}$-H solutions with $n \leq 0.97$ display no superconductivity at $T \geq 2$ K; superconductivity reappears in the $Pd_{85}Pt_{15}$-H and $Pd_{80}Pt_{20}$-H solutions and

then vanishes again, as the alloys with 25, 40 and 60 at.% Pt loaded with hydrogen up to $n = 0.92$, 0.51 and 0.11, respectively, are not superconducting at $T \geq 2$ K.

Superconductivity of two $Pd_{97.2}Pt_{2.8}$-H samples prepared under high hydrogen pressures at room temperature was studied in Ref. [76]. As seen from Fig. 33, the results of Ref. [76] and Ref. [95] differ significantly, but they are not contradictory in view of the very large scatter in the $T_c(n)$ values determined in Ref. [95]. Superconducting properties of the Pd-Pt-H system were also studied on samples with implanted hydrogen [3]. The maximum superconducting temperature achievable with hydrogen implantation was reported to reach 9–9.5°K for the alloys containing up to about 30 at.% Pt and to decrease steeply at higher platinum concentrations. The results of Ref. [3] and Ref. [95] are inconsistent.

3.4. Hydrides of alloys of V, Nb and Ta with Ru and Os

A significant increase of the superconducting temperature on hydrogenation was also observed for Nb alloyed with Ru [98], Rh [99] and Pd [99,100]. Concentrations of the alloying metals were within 15–35 at.%. The alloys were loaded with hydrogen either by electrolysis of H_2SO_4 [98,100], or in a hydrogen atmosphere at a pressure of 0.1 GPa and temperatures up to 400°C [99]. Regretfully, the Nb-Me-H samples studied in Refs. [98-100] were inhomogeneous and multi-phase that made it difficult to determine the crystal structure and the hydrogen content of the superconducting phases.

The encouraging results of Refs. [98–100] motivated further studies of the effect of hydrogen on superconductivity of the Nb-Ru [101] and Nb-Rh [102] alloys and also of V-Ru [103], Ta-Ru [104], V-Os and Ta-Os [105] alloys. Vanadium and tantalum are chemical analogues of niobium, all staying in the same column V of the periodic table; osmium is an analogue of ruthenium from group VIII. The alloys were hydrogenated in a hydrogen atmosphere at 300 or 325°C and pressures up to 6.5–9 GPa followed by the rapid cooling under pressure down to 90–100 K. To prevent hydrogen loss, the samples thus obtained were never warmed above 100 K until their crystal structure and superconducting temperature were determined.

The structure types, lattice parameters and T_c values of the phases formed in the studied systems are listed in Table 5. For every system, an isotherm of hydrogen solubility at 300 or 325°C was constructed and phase compositions of quenched samples were examined by X-ray diffraction at ambient pressure and 83 K. Most phase transitions observed in the systems were sluggish, and samples synthesized in the pressure intervals of such transitions remained in a non-equilibrium two-phase state despite a rather long synthesis time of a day or more used in the experiments. Table 5 compiles only those results that were obtained with single-phase samples.

Table 5. Composition of the alloy, superconducting temperature T_c, pressure and temperature of the hydrogenation, structure and parameters of the metal sublattice at ambient pressure and 80–100°K for some alloys of *d*-metals and their high-pressure hydrides.

Alloy	n = H/Me	T_c [K]	Synthesis		Structure	a [Å]	b [Å]	c [Å]	N_{eff}^{e} [el/atom Me]	Ref.
			P [GPa]	T [°C]						
$V_{90}Ru_{10}$	0	<2	—	—	α	3.011	—	—	5.3	[103]
	0.5	<2	0.8	300	β	2.996	3.302	—	5.55	
	1.04	3.0	1.1–3.6	300	γ_1	3.971	—	—	5.82	
	2.0	<2	>3.8	300	γ_2	4.265	—	—	6.3	
$V_{81.5}Ru_{18.5}$	0	<2	—	—	α	3.005	—	—	5.56	
	1.12	<2	1.3	300	ε	2.787	4.688	—	6.12	
	1.36	<2	7	300	ε	2.858	4.696	—	6.24	
$V_{66}Ru_{34}$	0	<2	—	—	α^{or}	2.995	—	—	6.02	
	1.24	<2	2.4	300	ε	2.810	4.577	—	6.64	
	1.34	<2	7	300	ε	2.822	4.572	—	6.69	
$Nb_{83}Ru_{17}$	0	<2	—	—	α	3.242	—	—	5.51	[101]
	1.92	<2	>4	325	ε′	5.391	3.170	5.113	6.47	
$Nb_{74.5}Ru_{22.5}$	0	<2	—	—	α	3.217	—	—	5.53	
	1.04	5.08	1.2	325	γ′	4.244	4.180	—	6.05	
	1.72	<2	7	325	≈ε	3.082	5.033	—	6.39	
$Nb_{69}Ru_{31}$	0	<2	—	—	α	3.199	—	—	5.93	
	1.04	4.3	2	325	γ′	4.23	4.16	—	6.45	
	≥1.5	<2	7	325	≈ε	3.05	4.98	—	6.68	
$Nb_{50}Ru_{50}$	0	<2	—	—	γ″	4.371	3.396	4.225	6.5	
	0.24	<2	1.0–1.4	325	γ_2″	4.379	3.459	4.327	6.62	
	1.13–1.25	<2	2.2–7	325	ε′	5.098	2.914	4.727	7.07-7.13	
$Ta_{77.4}Ru_{22.6}$	0	<2	—	—	α	3.316	—	—	5.68	[104]
	1.10	3.1	>3.2	300	ε′	5.188	2.966	4.951	6.23	
$Ta_{69}Ru_{31}$	0	<2	—	—	γ^{or}	3.194	—	—	5.93	
	0.95	2.8	>4.2	300	ε′	5.163	2.937	4.881	6.41	

Table 5 (continued).

Alloy	n = H/Me	T_c [K]	Synthesis		Structure	a [Å]	b [Å]	c [Å]	N^e_{eff} [el/atom Me]	Ref.
			P [GPa]	T [°C]						
$V_{91}Os_9$	0	<2	—	—	α	3.012	—	—	5.27	[105]
	0.6	<2	2	325	α	3.110	—	—	5.57	
	>1.7	<2	>3	325	γ	4.250	—	—	6.12	
$V_{79.5}Os_{20.5}$	0	<2	—	—	α	3.004	—	—	5.62	
	0.2	<2	3.5	325	α	3.037	—	—	5.72	
	1.03	<2	>4	325	ε	2.848	4.665	—	6.13	
$Ta_{88.5}Os_{11.5}$	0	<2	—	—	α	3.256	—	—	5.35	
	0.43	<2	9	325	α	3.324	—	—	5.56	
$Nb_{88}Rh_{12}$	0	1.34	—	—	α	3.260	—	—	5.48	[102]
	0.81	<0.35	0.03–0.07	325	α	3.404	—	—	5.88	
	1.7	0.75	2.5	325	γ′	4.508	4.431	—	6.33	
	2.0	0.9	5.5–7	325	γ′	4.532	4.523	—	6.48	
$Nb_{65}Rh_{35}$	0	2.65	—	—	σ	5.090	5.090	—	6.4	
	0.6	2.45	1.5	325	σ	5.298	5.298	—	6.7	
	1.0	2.25	3.5	325	σ	5.347	5.347	—	6.9	
	1.4	1.8	7	325	σ	5.412	5.412	—	7.1	
$Zr_{50}Ru_{50}$	0	<0.34	—	—	α^{or}	3.249	—	—	6	[121]
	1.1	3.0	7	325	CrB	3.668	4.509	10.65	6.55	
$Hf_{50}Ru_{50}$	0	1.18	—	—	α^{or}	3.225	—	—	6	
	1.8	4.5	3–7	325	CrB	3.655	4.462	10.58	6.9	

Structures of the metal lattices are: α = *bcc*, α^{or} = CsCl type, β = β-V_2H type (parameters of the tetragonal pseudocell are given), γ = *fcc*, γ′ = *fc tetragonal*, γ″ = the structure based on a *fc orthorhombic* pseudocell, ε = *hcp*, ε′ = rhombically distorted *hcp*, σ = σ-phase ($D8_b$), CrB = orthorhombic CrB-type. $N^e_{eff} = N^e + 0.5n$, where N^e is the average number of outer $s + d$ electrons per atom in the starting alloy.

In the figures that follow, X-ray results for various phases will often be presented in the form of values $\Delta V_a(n)$ of the volume increase per metal atom accompanying the hydride formation. Sometimes such a presentation is rather informative and makes it possible to estimate independently the hydrogen content of a phase, because the $\Delta V_a(n)$ dependence of many transition metals and their alloys is approximately linear over a wide range of hydrogen contents [106], the slope $\beta = V_a/n$ varying from about 1.5 Å^3 per metal atom per H atom for solid hydrogen solutions in α-Mn [107] to about 3 Å^3 per metal atom per H atom for the Pd-H solutions [108]. For example, $\Delta V_a(n)$ for all phases formed in the Nb-H system is satisfactorily expressed by a linear dependence with $\beta \approx 2.5$ Å^3 per metal atom per H atom [106].

3.4.1. *V-Ru-H system*

Three V-Ru alloys containing 10, 18.5 and 34 at.% Ru were examined for the occurrence of superconducting hydrides [103]. The starting alloys with 10 and 18.5 at.% Ru had a disordered *bcc* (α) crystal lattice. The lattice of the alloy with 34 at.% Ru was ordered to the CsCl type structure. None of the alloys was superconducting at $T \geq 2$ K.

The alloys were loaded with hydrogen at 300°C and pressures from 0.2–7 GPa. The results of studies on the $V_{90}Ru_{10}$-H samples prepared in this way are shown in Fig. 34.

As seen from Fig. 34a, the hydrogen content of the single-phase samples increases in a step-wise manner from $n \approx 0.5$ for the β-solutions formed at $0.2 \leq P \leq 1$ GPa to $n \approx 1$ for the γ_1 solutions with an *fcc* metal lattice at $1.5 \leq P \leq 3.2$ GPa and then to $n \approx 2$ for the γ_2 solutions at $P \geq 3.9$ GPa. The β-phase in the $V_{90}Ru_{10}$-H system is an analogue of the γ-V_2H phase in the V-H system [106,109], the ΔV_a and c_β/a_β values of these phases also being close. The γ_2-phase in $V_{90}Ru_{10}$-H can be considered as an analogue of γ-VH_2 with the CaF_2-type crystal structure, the ΔV_a value of γ-VH_2 being somewhat smaller [38,109]. The γ_1-phase in $V_{90}Ru_{10}$-H has no analogue among the phases in the V-H system. As seen from Fig. 34b, this very γ_1-phase is a superconductor and has $T_c \approx 3.0$ K.

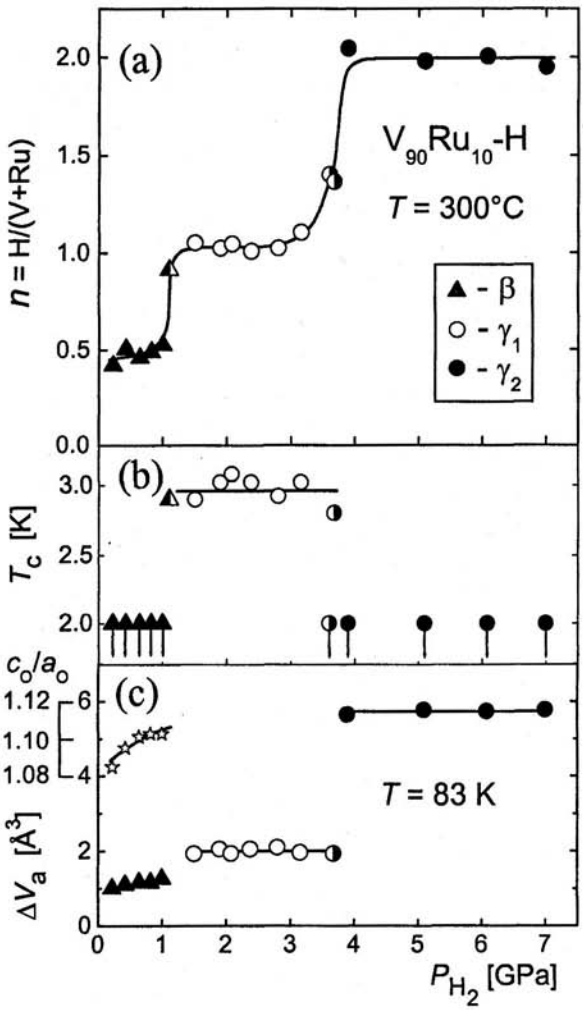

Fig. 34. System $V_{90}Ru_{10}$-H [103]. The hydrogen content n (**a**); the superconducting temperature T_c (**b**); the volume increase per metal atom ΔV_a and the axial ratio c_β/a_β (open stars) of the body-centered tetragonal pseudocell of the β-phase (**c**) are given as functions of the hydrogen pressure P_{H_2} of synthesis at 300°C. β is the monoclinic phase of the β-V_2H type; γ_1 and γ_2 are the solutions with an *fcc* metal lattice. The half-filled symbols stand for two-phase samples. The symbols with arrows in Fig. 34b indicate the absence of superconductivity at $T \geq 2$ K.

The spectra of optical hydrogen vibrations in the γ_1-phase ($n = 1.04$) and γ_2-phase ($n = 1.83$) of $V_{90}Ru_{10}$-H were studied by inelastic neutron scattering (INS) [110]. The energy $\hbar\omega_0 \approx 150$ meV of the fundamental optical peak in the INS spectrum of the γ_2-phase [110] was lower than $\hbar\omega_0 \approx 165$ meV for γ-$VH_{1.92}$ [111], but still lay in the range characteristic of dihydrides of *d*-metals with hydrogen atoms on tetrahedral interstices in the *fcc* metal lattice (the CaF_2-type structure) [111]. Such a peak in the spectrum of the γ_1-phase of $V_{90}Ru_{10}$-H was observed at $\hbar\omega_0 \approx 115$ meV [110]. As interatomic forces strengthen with decreasing interatomic distances, the

smaller $\hbar\omega_0$ value of the γ_1-phase with the smaller lattice parameter points to different hydrogen positions in the γ_1- and γ_2-phases. The value of $\hbar\omega_0 \approx 115$ meV is more typical of *fcc* and *hcp* monohydrides of *d*-metals with octahedral hydrogen coordination [112]. Assuming a disordered *fcc* metal lattice, the superconducting γ_1-phase of $V_{90}Ru_{10}$-H therefore has the same crystal structure of the NaCl-type (Fig. 19c) as superconducting PdH.

As seen from Table 5, the phases formed at 300°C in the $V_{81.5}Ru_{18.5}$-H and $V_{66}Ru_{34}$-H systems are different from those in the $V_{90}Ru_{10}$-H system, and none of these phases is superconducting at $T \geq 2$ K.

3.4.2. *Nb-Ru-H system*

In the work of Ref. [101], hydrides of four Nb-Ru alloys containing 17, 25.5, 31 and 50 at.% Ru were synthesized in an H_2 atmosphere at 325°C and pressures up to 7 GPa. In agreement with the data in literature [113], the starting Nb-Ru alloys with 17, 25.5 and 31 at.% Ru had a disordered *bcc* (α) structure, while the 50 at.% Ru alloy had a structure with a face-centered orthorhombic pseudo-cell denoted as γ'' in Table 5. None of the alloys was superconducting at $T \geq 2$ K in accordance with the earlier result [98] that *bcc* Nb-Ru alloys with 20, 25 and 33 at.% Ru had $T_c = 0.24$, 0.25 and <0.35 K, respectively.

In the $Nb_{83}Ru_{17}$-H system, single-phase samples were obtained only at pressures above 4 GPa. The ε'-phase with $n \approx 1.9$ formed under these conditions has an orthorhombically distorted *hcp* metal lattice, see Table 5. To illustrate the character of the distortion, Fig. 35 shows schematically a hexagonal plane of the *hcp* lattice where the solid lines mark the orthorhombic cell. In the standard description of hexagonal structures, with the orthorhombic axis Z_{orth} along the hexagonal axis X_{hex} and the axis Y_{orth} along Z_{hex}, the parameter $a_{orth} = a_{hex} \cdot \sqrt{3}$. The $a_{\varepsilon'}/c_{\varepsilon'}$ ratio of the $Nb_{83}Ru_{17}$-H ε'-phase being $0.982\sqrt{3}$, this may be regarded as the result of a uniform stretching of the hexagonal lattice in the [10.0] direction.

At high hydrogen pressures, the Nb-Ru alloys containing 25.5, 31 and 50 at.% Ru also form the ε'-phase. Its hydrogen content monotonically decreases and the $a_{\varepsilon'}/c_{\varepsilon'}$ ratio monotonically increases with increasing ruthenium concentration and reach $n \approx 1.2$ and $a_{\varepsilon'}/c_{\varepsilon'} = 1.010\sqrt{3}$ for the alloy with 50 at.% Ru. In the case of the alloys containing 25.5 and 31 at.% Ru, $a_{\varepsilon'}/c_{\varepsilon'} \approx \sqrt{3}$ and the symmetry of their metal lattices is nearly hexagonal (ε).

As seen from Table 5, neither the ε'-phase, nor α- or γ''-solutions of hydrogen in any Nb-Ru alloy are superconducting at $T \geq 2$ K. Superconductivity was observed only in the face-centered tetragonal γ'-phase with $n \approx 1$ formed by the alloys with 25.5 and 31 at.% Ru. Results for the $Nb_{74.5}Ru_{25.5}$-H system are given in Fig. 36; those for the $Nb_{69}Ru_{31}$-H system look similar. The superconducting temperature is a maximum for the single-phase samples formed in a narrow pressure range and it decreases steadily in the two-phase ($\gamma'+\varepsilon$) samples as the synthesis pressure increases.

This T_c decrease as well as the wide interval of the $\gamma' \rightarrow \varepsilon$ transition are due to the specific character of this transition, which proceeds by accumulating '*hcp*' stacking faults in the metal lattice of the γ'-phase [101].

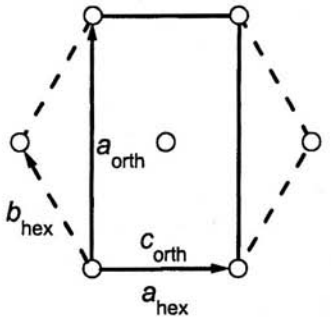

Fig. 35. Schematic of the (00.1) plane of a hexagonal lattice.

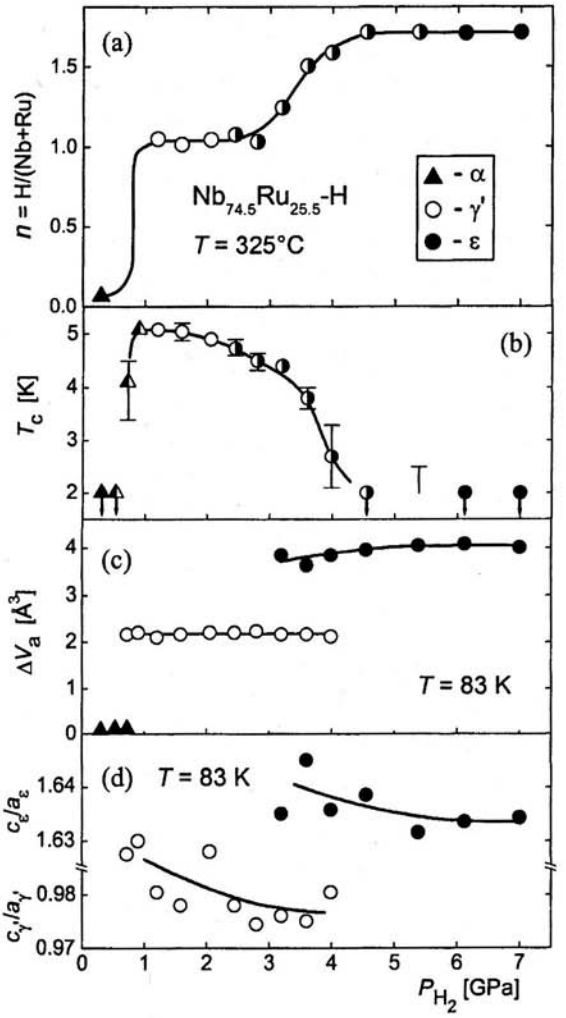

Fig. 36 (right). System $Nb_{74.5}Ru_{25.5}$-H [101]. The hydrogen content n (**a**); the superconducting temperature T_c (**b**); the volume increase per metal atom ΔV_a (**c**); the axial ratios $c_{\gamma'}/a_{\gamma'}$ and $c_\varepsilon/a_\varepsilon$ of the γ'- and ε-phase (**d**) are given as functions of the hydrogen pressure P_{H_2} of synthesis at 325°C. α denotes the *bcc* phase; γ' is the phase with a face-centered tetragonal metal lattice; ε is the phase with a (pseudo) hexagonal close-packed metal lattice. The half-filled symbols stand for two-phase samples. In Fig. 36b, the symbols with arrows indicate the absence of superconductivity at $T \geq 2$ K; the vertical bars show the width of the superconducting transition.

The T_c values of the γ'-phases from Ref. [101] are in a satisfactory agreement with the results of Ref. [98] for the Nb-Ru alloys with 20, 25 and 33 at.% Ru loaded with

hydrogen electrolytically. However, based on an X-ray pattern taken of a superconducting $Nb_{80}Ru_{20}$-H sample, the T_c values determined in Ref. [98] were ascribed to a different phase with an *fcc* metal lattice and $a \approx 4.41$ Å corresponding to a dihydride phase ($\Delta V_a \approx 4.81$ Å^3 per metal atom). This conclusion of Ref. [98] is not convincing because the sample was exposed to room temperature for a few minutes while being put into the X-ray cryostat that should lead to a nearly complete loss of hydrogen from any dihydride phase. Ref [101] also argues that the *fcc* phase in Ref. [98] could be a sort of carbide formed in the course of spark machining of the starting $Nb_{80}Ru_{20}$ sample.

Optical hydrogen vibrations in a single-phase γ′-sample ($n = 1.00$) and in a two-phase γ′+ε sample ($n = 1.56$) of $Nb_{74.5}Ru_{25.5}$-H prepared at high hydrogen pressures were studied by INS at15 K [110]. In accordance with the tetragonal symmetry of the crystal structure, the fundamental optical band of the γ′-phase is split into two overlapping peaks centered at $\hbar\omega_0 \approx 86$ and 136 meV. This result is compatible with the octahedral coordination of hydrogen atoms in the γ′-phase, which can be expected in view of its MeH stoichiometry.

The fundamental optical H band of the ε-phase of $Nb_{74.5}Ru_{25.5}$-H consists of a single broad peak centered at $\hbar\omega_0 \approx 152$ meV. The occurrence of only one peak indicates that only one type of interstices is occupied by hydrogen in this phase. Judging by the hydrogen content $n \approx 1.7$ of the ε-phase, those are tetrahedral interstices. The absence of peak splitting agrees with the nearly cubic symmetry of such interstices formed by four metal atoms sitting at the apices of tetrahedrons, which are nearly ideal because of the nearly ideal ratio of $c/a = 1.633 \approx \sqrt{8/3}$ of the ε-phase (see Table 5).

3.4.3. *Ta-Ru-H system*

Hydrides of two Ta-Ru alloys containing 22.6 and 31 at.% Ru were synthesized in a hydrogen atmosphere at 300°C and pressures up to 8 GPa [104]. In agreement with the data in literature [114], the starting Ta-Ru alloy with 22.6 at.% Ru had a disordered *bcc* (α) structure, while the lattice of the alloy with 31 at.% Ru was ordered to the CsCl type structure. None of the alloys was superconducting at $T \geq 2$ K.

Loading the two Ta-Ru alloys with hydrogen gave similar results. Fig. 37 illustrates the case of the alloy containing 22.6 at.% Ru. Dissolution of hydrogen in the α- or α^{or}-phase of the Ta-Ru alloys did not make them superconducting at $T \geq 2$ K. Superconductivity was observed in the ε′-phases with $n \sim 1$ formed at higher hydrogen pressures (see also Table 5). The hydrogen content, superconducting temperature and lattice parameters of the ε′-phases were virtually independent of the synthesis pressure. The $a_{\varepsilon'}/c_{\varepsilon'}$ ratio of these phases was $1.010\sqrt{3}$ and $1.015\sqrt{3}$ for the alloys with 22.6 and 31 at.% Ru, respectively, thus corresponding to a uniform compression of the *hcp* metal lattice in the [10.0] direction.

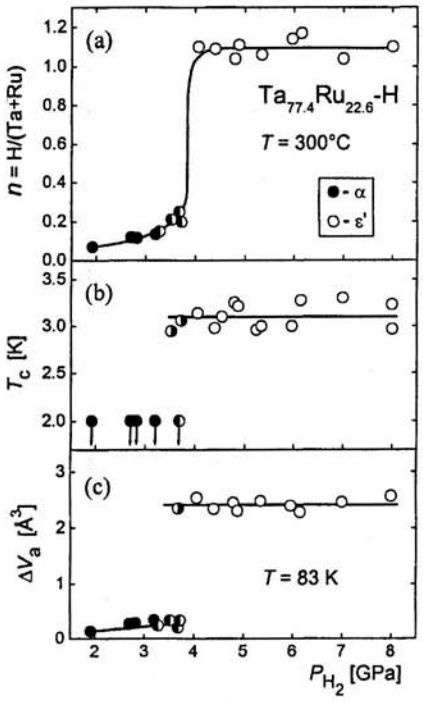

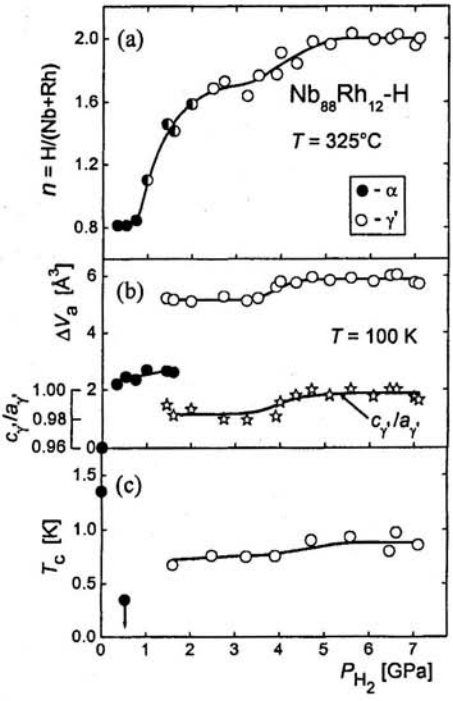

Fig. 37 (left). System $Ta_{77.4}Ru_{22.6}$-H [104]. The hydrogen content n (**a**); the superconducting temperature T_c (**b**) and the volume increase per metal atom ΔV_a (**c**) are given as functions of the hydrogen pressure P_{H_2} of synthesis at 300°C. α is the *bcc* phase; ε′ is the phase with an orthorhombically distorted *hcp* metal lattice. The half-filled symbols stand for two-phase samples. The symbols with arrows in Fig. 37b indicate the absence of superconductivity at $T \geq 2$ K.

Fig. 38 (right). System $Nb_{88}Rh_{12}$-H [102]. The hydrogen content n (**a**); the volume increase per metal atom ΔV_a and the axial ratio $c_{\gamma'}/a_{\gamma'}$ (open stars) of the γ′-phase (**b**) and the superconducting temperature T_c (**c**) are given as functions of the hydrogen pressure P_{H_2} of synthesis at 325°C. α is the *bcc* phase; γ′ is the phase with a face-centered tetragonal metal lattice. The half-filled symbols stand for two-phase samples. The symbol with an arrow in Fig. 38c indicate the absence of superconductivity at $T \geq 0.35$ K.

3.4.4. *V-Os-H and Ta-Os-H systems*

Hydrides formed at 325°C by the $V_{91}Os_9$ and $V_{79.5}Os_{20.5}$ alloy at hydrogen pressures up to 7 GPa and by the $Ta_{88.5}Os_{11.5}$ alloy at pressures up to 9 GPa were studied in the work of Ref. [105]. Each starting alloy had a disordered *bcc* (α) structure and showed no superconductivity at $T \geq 2$ K. The basic results of Ref. [105] are presented in Table 5.

In contrast to the $V_{90}Ru_{10}$ alloy [103], the $V_{91}Os_9$ alloy does not form either β-V_2H type solutions, or a superconducting γ_1 phase with $n \approx 1$. Instead, the primary α-solution of $V_{91}Os_9$-H transforms directly to an *fcc* dihydride phase as the hydrogen pressure increases. Similar to the $V_{81.5}Ru_{18.5}$ and $V_{66}Ru_{34}$ alloy [103], the $V_{79.5}Os_{20.5}$ alloy forms an *hcp* monohydride. Alloying Ta with 11.5 at.% Os strongly decreases the equilibrium hydrogen solubility, and only primary α-solutions with $n \leq 0.43$ are formed in the $Ta_{88.5}Os_{11.5}$-H system at pressures up to 9 GPa.

None of the phases in the studied V-Os-H and Ta-Os-H system is superconducting at $T \geq 2$ K.

3.5. Hydrides of Nb-Rh alloys

The Nb-Rh alloys provide extensive opportunities for a study of the influence of hydrogen on the superconductivity of phases with different crystal structures. Three superconducting Nb-Rh alloys containing 12, 25 and 35 at.% Rh with the *bcc*, A15 (β-W) and $D8_b$ (σ) structure, respectively, were hydrogenated at 325°C and pressures up to 7 GPa and then X-rayed at 100 K and analyzed for superconductivity at temperatures down to 0.35 K [102]. The results are presented in Tables 5 and 6 and in Figs. 38–41.

In the $Nb_{88}Rh_{12}$-H system, as seen from Figs. 38a and 38b, primary α-solutions with hydrogen contents up to $n \approx 0.8$ are formed at pressures to about 0.8 GPa. At higher pressures, the system undergoes a polymorphous phase transition resulting in the formation of γ′-solutions with a face-centered tetragonal metal lattice and $n > 1.7$. The dependences of the hydrogen solubility and lattice parameters of the γ′-solutions in the pressure range 1–2 GPa are typical of supercritical isotherms in the metal-hydrogen systems. This suggests the occurrence of an isomorphous $\gamma_1' \leftrightarrow \gamma_2'$ transformation terminating at a critical point at a pressure of about 1.5 GPa and a temperature below 325°C.

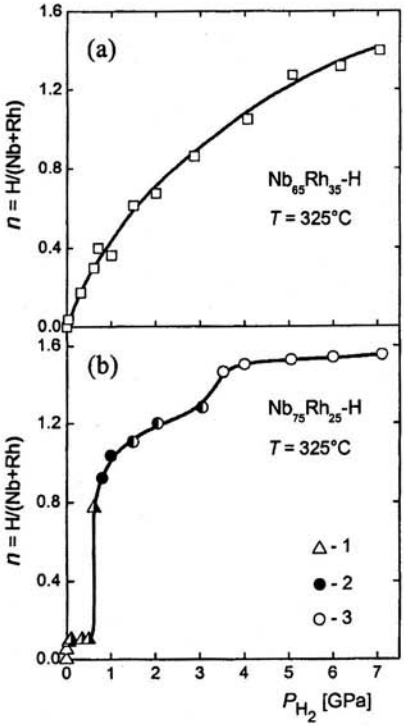

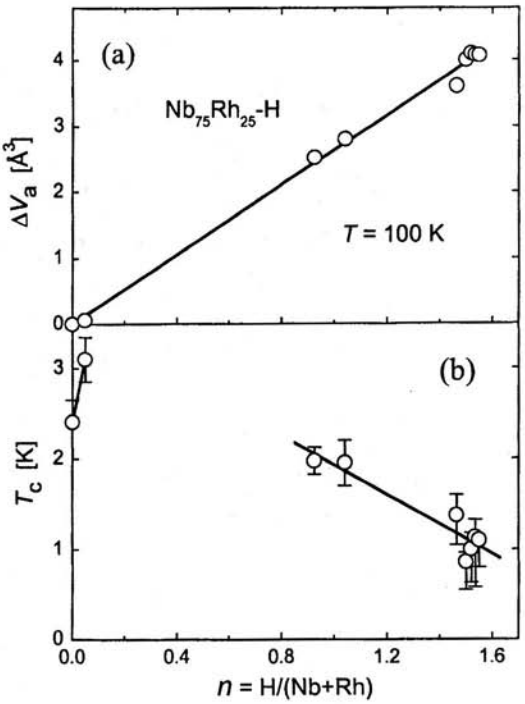

Fig. 39 (left). Hydrogen solubility in the $Nb_{65}Rh_{35}$ (**a**) and $Nb_{75}Rh_{25}$ (**b**) alloy at 325°C [102]. Symbols 1–3 in Fig. 39b stand for single-phase samples with the same A15 type of the metal lattice, which are formed in three different intervals of the hydrogen concentration. The half-filled symbols indicate two-phase samples.

Fig. 40 (right). Solid solutions $Nb_{75}Rh_{25}$-H with the A15 type metal lattice [102]. The volume increase per metal atom ΔV_a (**a**) and the superconducting temperature T_c (**b**) are presented as functions of the hydrogen content n of single-phase samples. The vertical bars in Fig. 40b show the width of the superconducting transition.

The superconducting temperature of the *bcc* $Nb_{88}Rh_{12}$ alloy drops from 1.34 K to below 0.35 K on dissolution of $n = 0.81$ of hydrogen (Fig. 38c, Table 5). The superconductivity reappears again in the γ′-solutions and T_c even slightly increases from ≈0.75 K to ≈0.9 K with the hydrogen content of the solutions increasing from $n \approx 1.7$ to $n \approx 2$. At present, the γ′-phase of $Nb_{88}Rh_{12}$-H is the only known superconducting dihydride. In particular, Nb and V dihydrides are shown to possess no superconductivity at temperatures down to 1.2 K [115] and 0.35 K [102] (see also Table 4).

The $Nb_{75}Rh_{25}$-H system at 325°C undergoes two phase transitions isomorphous in respect of the metal lattice. As seen from Fig. 39b, the transitions are sluggish and develop over rather large pressure intervals 0.005–0.7 and 1.5–3.3 GPa. Samples synthesized in the one-phase ranges have the metal lattice of the same A15 type as the starting $Nb_{75}Rh_{25}$ alloy. The atomic volume of the alloy increases approximately linearly with the hydrogen content at a rate of $\beta \approx 2.63$ Å^3 per metal atom per H atom (Fig. 40a). The behavior of T_c of these samples is more complex. As seen from Fig. 40b, the superconducting temperature of the primary hydrogen solutions increases with n, whereas in the solutions with $n \approx 0.9$ it falls below T_c of the starting $Nb_{75}Rh_{25}$ alloy and then decreases to approximately 1 K at $n \approx 1.5$.

The equilibrium hydrogen solubility in the σ-type $Nb_{65}Rh_{35}$ alloy at 325°C monotonically increases with pressure and reaches $n \approx 1.4$ at 7 GPa (Fig. 39a). An increase in the hydrogen concentration is accompanied by a monotonic decrease in T_c from 2.65 to ≈1.8 K (Fig. 41b) and by an approximately linear volume expansion at a rate of $\beta \approx 2.52$ Å^3 per metal atom per H atom (Fig. 41a), whereas the c_σ / a_σ ratio varies nonmonotonically reaching a maximum at $n \approx 0.6$. By analogy with some other hydrogen solid solutions with complex tetragonal lattices (*e.g.* Zr_2Pd-H [116]), the maximum of the c_σ / a_σ dependence was attributed [102] to the change in the type of interstices occupied by hydrogen.

In the work of Ref. [99], hydrogenation of a $Nb_{80}Rh_{20}$ alloy to $n = 0.10$ at a hydrogen pressure of 0.1 GPa and a temperature of 400°C increased its T_c from 2.65 to 5.64 K. According to the phase diagram of the binary Nb-Rh system [117], the $Nb_{80}Rh_{20}$ alloy should consist of a mixture of a *bcc* phase with 13–14 at.% Rh and an A15 phase containing 25 at.% Rh. In Ref. [99], the observed T_c values were ascribed to the *bcc* phase and the primary hydrogen solution on its base. The results of Ref. [102] show that the superconducting phases in Ref. [99] were the A15 phase and its solution with hydrogen.

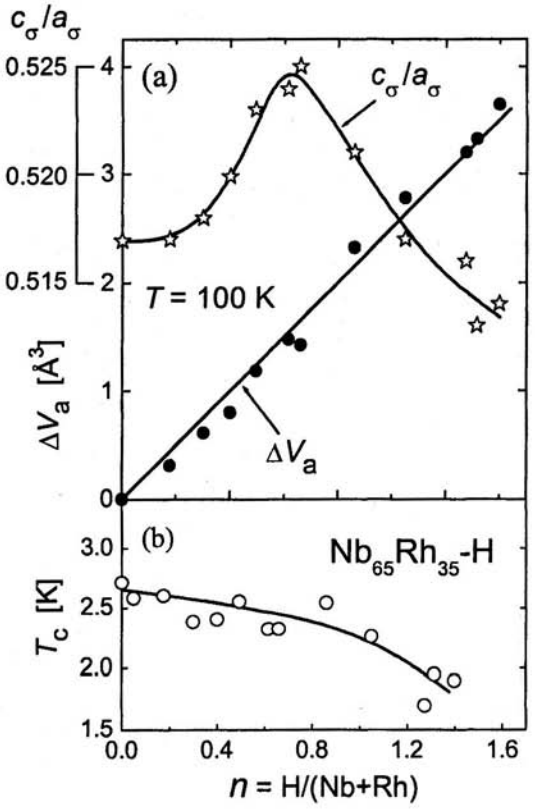

Fig. 41. Solid solutions $Nb_{65}Rh_{35}$-H with the σ-type metal lattice [102]. The volume increase per metal atom ΔV_a (filled circles) and the axial ratio c_σ/a_σ (open stars) of the tetragonal metal lattice (**a**) and the superconducting temperature T_c (**b**) are shown as functions of the hydrogen content n of single-phase samples.

3.6. Matthias rule and rigid *d*-band model

As was first noted by Matthias [118], there is a correlation between the superconducting temperature T_c and the electron concentration N^e of alloys of transition metals. Namely, the electron concentrations of most alloys with relatively high T_c values are grouped in two intervals centered at $N^e \approx 4.5$ and ≈ 6.5 electrons per atom, N^e being defined as the average number of outer $d + s$ electrons per atom of the alloy. Since the T_c value is determined by the electron structure and the lattice dynamics of the alloy and both are strongly dependent on its crystal structure, the occurrence of the above correlation can be explained assuming that (*i*) the crystal structure of transition alloys is to a large extent determined by the electron concentration and (*ii*) with the given crystal structure, the concentration dependence of the electron structure largely obeys the rigid band model. The correlation (Matthias rule) then suggests that alloys with the crystal structures characteristic of the concentration intervals around $N^e \approx 4.7$ and ≈ 6.7 electrons per atom have electronic structures most favorable for the

superconductivity, and these alloys could have high T_c values if the lattice dynamics is favorable as well.

For an alloy taken at random, Matthias rule cannot predict the T_c value or even the occurrence of superconductivity. Nevertheless, based on this rule, one could expect that the T_c values of a continuous solid solution plotted against N^e should form a two-peaked curve with maxima in the vicinity of 4.5 and 6.5 electrons per atom. The curves for different solutions could differ significantly, of course, and should be constructed individually. However, as long as the rigid band model is valid, the changes in the $T_c(N^e)$ dependence should not be drastic if one of the components of the solution is substituted by a similar *d*-metal. To incorporate hydrogen in this scheme, the rigid *d*-band model can be used.

The rigid *d*-band model was first proposed to explain the effect of hydrogen on the magnetic properties of 3*d*-metals and their alloys with an *fcc* [4] and *hcp* [119] lattice. Its applicability to the superconducting properties of hydrides of 4*d*- and 5*d*-metals was later considered in Ref. [120] and to the crystal structures of high-pressure hydrides in Ref. [121]. A more detailed discussion of the model is given in Ref. [122].

The rigid *d*-band model takes into account the specific changes in the band structure of transition metals on hydrogen uptake first outlined by Switendick [123] and then confirmed by many other calculations for various *d*-metals. According to the calculations, the hydrogen nearly does not affect the upper part of the *d*-band of the host metal, but noticeably decreases the energy of the *s*-states. The latter reduces the rate η of *d*-band filling with the electrons supplied by the hydrogen atoms to a value of the order of $\eta = 0.5$ electrons per H atom (varying from about 0.3 to about 1 for different metals and alloys). This concept implies that those properties of the metal which essentially depend on the *d*-band occupation should vary with increasing hydrogen concentration as if the hydrogen were merely donor of a fractional number of $\eta \sim 0.5$ electrons per atom into the otherwise unchanged metal *d*-band. This is the approximation that we call a rigid *d*-band model for brevity.

As the electron-phonon interaction depends strongly on the electron density of states at the Fermi level, and the density of *d*-states in transition metals is much higher than that of *s*-states, it is the degree of *d*-band filling that actually governs the T_c behavior of transition metals and alloys. If the $T_c(N^e)$ dependence is known, the rigid *d*-band model therefore allows one to estimate the contribution from the increasing *d*-band occupancy to the change in T_c on hydrogenation:

$$T_c(n) = T_c(N^e + n) \approx T_c(N^e + 0.5n) \equiv T_c(N^e_{\text{eff}}) \qquad (1)$$

where N^e is the electron concentration of the alloy and n is the H-to-metal ratio of its hydride.

Assuming, in accordance with the Matthias rule, that the $T_c(N^e)$ dependences for alloys with any crystal structure are smooth curves with two maxima around 4.5 and 6.5 electrons per atom and a deep minimum around 5.5 electrons per atom, Eq. (1) qualitatively describes the experimental data for hydrides of any *d*-metal except Pd and for many alloys discussed above. In fact, it explains the occurrence of

superconductivity in χ-, η- and κ-hydride of Ti with $N^e_{eff} \approx 4.35$–4.45 el./atom Ti (Table 1) and in the ε-hydride of Mo with $N^e_{eff} \approx 6.5$ el./atom Mo (Table 4), the decrease of T_c with increasing hydrogen concentration in the ε-solutions of hydrogen in Ru ($N^e = 8$ el./atom), Tc and Re ($N^e = 7$ el./atom) and the absence of superconductivity in γ-hydride of Rh with $N^e_{eff} \approx 9.5$ el./atom and γ-dihydrides of V and Nb with $N^e_{eff} \approx 6$ el./atom (Table 4). Formula (1) also accounts for the presence of superconductivity in ε′-hydrides of the Ta-Ru alloys with $N^e_{eff} \approx 6.2$–6.4 el./atom (Table 5) and in various hydrides of the Nb-Rh alloys (Tables 5 and 6) including γ′-dihydrides of the $Nb_{88}Rh_{12}$ alloy with $N^e_{eff} \approx 6.3$–6.5 el./atom.

At the same time, Eq. (1) obviously fails in explaining the superconducting properties of the V-Ru-H and Nb-Ru-H systems (Table 5). For example, γ_1-hydride of the $V_{90}Ru_{10}$ alloy ($N^e_{eff} \approx 5.8$ el./atom) is a superconductor whereas the γ_2-dihydride ($N^e_{eff} \approx 6.3$ el./atom) is not, *etc.* It should be noted, however, that the alloys from Table 5 are not very suitable for testing Eq. (1) since they are composed of metals positioned far from each other in the periodic table. The rigid band model is usually inapplicable to the electron structure of such alloys and their superconducting properties therefore may not obey Matthias rule. In particular, as seen from Table 5, the $Nb_{50}Ru_{50}$ alloy is not superconducting despite its $N^e = 6.5$ el./atom.

In the next two sections we will discuss the effect of hydrogen on T_c of two groups of alloys with superconducting properties well obeying the rigid band model. These are the *bcc* alloys of Nb with Ti [124] and the A15 alloys of Nb with 5*d*-metals Os, Ir, Pt and Au [120].

3.7. Hydrogen solid solutions in *bcc* Nb-Ti alloys

Niobium as well as V and Ta forms with hydrogen wide ranges of continuous *bcc* solutions at elevated temperatures. However, the $T_c(n)$ dependences of those solutions cannot be examined experimentally because of a very small equilibrium hydrogen solubility at low temperatures. For example, the maximum hydrogen content of the Nb-H solutions is only $n \approx 4 \cdot 10^{-2}$ at 300 K and falls down to $n \approx 4 \cdot 10^{-3}$ at 200 K [125]. The high-temperature homogeneous state of the *bcc* solutions with a higher hydrogen content cannot be quenched due to the high diffusion mobility of hydrogen resulting in the hydride precipitation from the oversaturated *bcc* solution even at a temperature as low as 150 K [125]. Besides, plastic deformation of the *bcc* matrix near to the hydride precipitations increases T_c by about 0.1 K that much exceeds the effect of the residual H dissolved in this matrix [126].

Alloying Nb with Ti makes it possible to fix the homogeneous high-temperature *bcc* state of the hydrogen solutions for investigations at low temperatures (see Ref. [127] and references therein) due to H trapping by the Ti atoms. The results of one such investigation [124] for the Nb-Ti alloys containing 20, 35 and 50 at.% Ti are presented in Fig. 42. The alloys were loaded with hydrogen under non-equilibrium

conditions at a hydrogen pressure of 1 GPa and temperature 200°C and then quenched to 80 K. Different hydrogen concentrations were achieved by varying the synthesis time. The method exploited the specific feature of the Nb-Ti-H system that the ingression of H into the samples at 200°C is controlled by processes on their surface and the diffusion in the bulk is fast enough to provide a nearly equilibrium distribution of hydrogen over the sample volume for any total H content reached. (The equilibrium phases at the synthesis conditions were γ-dihydrides. They also were synthesized in Ref. [124] and showed no superconductivity at $T \geq 2$ K.).

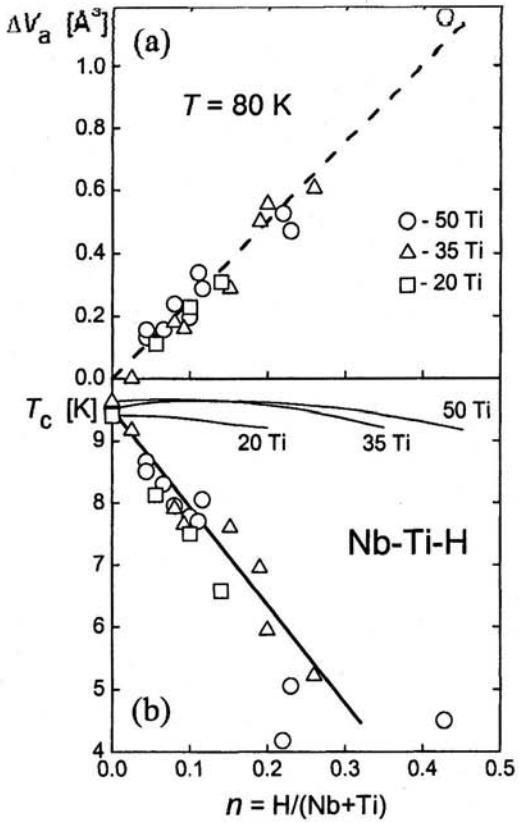

Fig. 42. Solid hydrogen solutions in *bcc* (α) Nb-Ti alloys containing 20, 35 and 50 at.% Ti [124]. The volume increase per metal atom ΔV_a (**a**) and the superconducting temperature T_c (**b**) are presented as functions of the hydrogen content n of single-phase samples. The dashed line in Fig. 42a shows the $\Delta V_a(n)$ dependence for the Nb-H α-solutions [106]. The thin solid curves labeled 50Ti, 30Ti and 20Ti in Fig. 42b are the dependences $T_c(n) = T_c(N^e + \eta n)$ calculated with $\eta = 1$ el./atom H using the $T_c(N^e)$ dependence for the *bcc* Nb-Ti alloys [129], where N^e is the electron concentration of the alloy.

As seen from Fig. 42a, the $\Delta V_a(n)$ values of the *bcc* samples of Nb-Ti-H are in satisfactory agreement with the approximately linear dependence for the *bcc* solutions Nb-H [106] with the slope $\beta \approx 2.5$ Å^3 per metal atom per H atom typical of hydrides of most 4*d*-metals and alloys. This indicates the absence of precipitations of dihydride phases, which should have caused a significant decrease in ΔV_a otherwise The linewidth of the diffraction pattern and the width of the superconducting transition ≈0.3 K of the Nb-Ti samples did not noticeably increase on hydrogenation

that suggests a good homogeneity of the *bcc* Nb-Ti-H solutions prepared in Ref. [124].

The $T_c(n)$ dependences for the three Nb-Ti alloys studied (Fig. 42b) do not differ from each other within experimental error and are close to a straight line with $dT_c/dn = -15$ K per H atom. A monotonic decrease of T_c with similar rates of –10 to –20 K per H atom was also observed for the Nb-Ti alloys containing 45.4–74.4 at.% Ti [128] and doped with H up to $n \sim 0.3$ using different methods (mainly, by melting or annealing in a hydrogen-containing atmosphere). Assuming that the Nb-Ti-H solutions investigated in Ref. [128] were the *bcc* solutions, the steep decrease of T_c at a rate of $dT_c/dn \approx -15$ K per H atom is characteristic of hydrogen solutions in *bcc* Nb-Ti alloys from the wide concentration interval 20–74.4 at.% Ti. One can therefore speculate that T_c of the *bcc* Nb-H and Ti-H solutions, if they were stable at low temperatures, also would decrease with increasing H content and the rate of the decrease would be of the same order of magnitude.

The observed $T_c(n)$ dependences for hydrogen solutions in *bcc* Nb-Ti alloys are inconsistent with the predictions of the rigid *d*-band model. In fact, $N^e = 4$ el./atom for Ti and 5 el./atom for Nb. The $T_c(N^e)$ dependence for the *bcc* Nb-Ti alloys, in agreement with the Matthias rule, has a shallow maximum at $N^e \approx 4.7$ el./atom [129], *i.e.* at the N^e value close to that for the $Nb_{65}Ti_{35}$ alloy. The dependences $T_c(n) = T_c(N^e + \eta n)$ calculated for the *bcc* Nb-Ti alloys with 50, 35 and 20 at.% Ti using $\eta = 1$ electron per H atom are shown in Fig. 42b by thin lines. These dependences do not agree at all with the experimental ones.

The value of $\eta = 1$ el. per H atom was chosen because it provides a quantitative description of the concentration dependence of magnetic susceptibility of the *bcc* Nb-Ti-H solutions at 180°C [130] and because approximately this value of η was calculated for the *bcc* V-H solutions [131], a close analogue of the Nb-Ti-H solutions. However, taking any other reasonable value of $\eta < 1$ el. per H atom cannot soften the disagreement between calculations and experiment either.

The experimental results of Ref. [130] evidence that hydrogenation causes only a very weak deformation of the *d*-band of *bcc* Nb-Ti alloys in the vicinity of the Fermi level, so the contribution to the $T_c(N^e)$ dependence from the *d*-band filling should be at least of the same order of magnitude as that given by Eq. (1) of the rigid *d*-band model. The steep and virtually identical decrease of the superconducting temperature of the studied alloys at a rate of about -15 K per H atom [124,128] is therefore due to another reason, which is common for all those alloys. Most likely, these are changes induced by hydrogen in the phonon spectrum of the host metal. For example, the changes can consist in the increase in the mean frequency of acoustic vibrations, as has been observed in *bcc* Nb and Ta with dissolved hydrogen [132].

3.8. Hydrogen solid solutions in A15 alloys of Nb with Os, Ir, Pt and Au

The applicability of the rigid band model to alloys of 4*d*- and 5*d*-metals in most cases is limited to intervals of a few atomic percent. The available experimental data make it possible, however, to specify at least two kinds of alloys with superconducting properties obeying the rigid band model. These are (*i*) primary solid solutions of neighboring elements in the periodic table and (*ii*) $A_{1-y}(B,C, \ldots)_y$ alloys or intermetallic compounds with fixed y, where the elements B, C, *etc.* are close neighbors, whereas element A is positioned far from them in the periodic table. In such systems replacing, for instance, element B by element C or varying their relative concentrations produces only minor changes in the band structure of the alloy. Wherever data are available, the Matthias plots of T_c vs. N^e for both kinds of alloys exhibit a large broad peak centered at $N^e \approx 6.3$–6.7 el./atom [117,133,134].

The effect of hydrogen on the superconducting temperature of four compounds of type (*ii*), the A15 alloys of Nb with 5d-metals Os, Ir, Pt and Au occupying successive places in the periodic table, was investigated in Ref. [120]. Samples were hydrogenated at 325°C and pressures up to 7 GPa, quenched under pressure to 83 K and then X-rayed at 100 K and analyzed for superconductivity at temperatures down to 0.35 K. The A15 compound Nb_3Au and its hydrides prepared in this way were also studied by X-ray and neutron diffraction at 120 K [135] and by ^{197}Au Mössbauer spectroscopy at 4.2 K [136]. The results of works [120,135,136] are presented in Table 6 and in Figs. 43–46.

Fig. 43 shows the hydrogen solubility isotherm at 325°C for the Nb_3Au compound. It demonstrates one feature common of all four Nb_3Me compounds studied. Namely, the compounds do not form with hydrogen a continuous solid solution. A certain increase of the hydrogen solubility in the primary solution is followed by a steep increase due to the phase transition and a further gradual rise at higher pressures. The pressure of the transition is the least for the Nb_3Au-H system and increases steadily with decreasing atomic number of the second component, reaching a maximum of about 4.5 GPa for the Nb_3Os-H system. The transition is isomorphous in respect of the metal lattice, and the concentrated solutions (hydrides) have metal lattices of the same A15 type as the starting compounds, but with larger lattice parameters.

Table 6. Composition, superconducting temperature T_c, pressure of synthesis in a hydrogen or deuterium atmosphere at 325°C and parameter of the metal sublattice at ambient pressure and 100 K for some Nb alloys and their high-pressure hydrides and deuterides with the A15 structure.

System	n = H/Me	T_c [K]	Synthesis pressure [GPa]	a [Å]	N^e_{eff} [el./atom Me]	Ref.
$Nb_{75}Rh_{25}$-H	0	2.4	—	5.130	6.00	[102]
	0.05	3.1	0.03	5.137	6.03	
	1.0	1.9	1	5.384	6.50	
	1.5	1.1	4–7	5.503	6.75	
$Nb_{75}Os_{25}$-H	0	1.0	—	5.138	5.75	[120]
	0.9	4.3	5.2	5.376	6.20	
	1.0	3.8	7	5.381	6.25	
$Nb_{75}Os_{25}$-D	1.02	3.0	7.04	5.375	6.26	
$Nb_{75}Ir_{25}$-H	0	1.9	—	5.135	6.00	
	0.02	2.4	2	5.139	6.01	
	1.0	3.0	4.2	5.383	6.50	
	1.18	2.7	6–7	5.412	6.59	
$Nb_{75}Ir_{25}$-D	1.16	2.9	7.04	5.414	6.58	
$Nb_{76}Pt_{24}$-H	0	9.2	—	5.161	6.20	
	0.05	9.2	0.2	5.186	6.23	
	1.0	2.3	3.2	5.407	6.70	
	1.28	?	5–7	5.442	6.84	
$Nb_{76}Pt_{24}$-D	1.30	?	7.06	5.438	6.85	
$Nb_{74}Au_{26}$-H	0	10.1	—	5.198	6.56	
	0.03	9.5	0.02	5.204	6.58	
	0.7	3.8	0.5	5.410	6.91	
	1.0	1.2	3.5	5.458	7.06	
	1.08	<0.4	7	5.470	7.10	
$Nb_{74}Au_{26}$-D	1.10	1.1	7.12	5.459	7.11	

$N^e_{eff} = N^e + 0.5n$, where N^e is the average number of outer $s + d$ electrons per atom in the starting alloy.

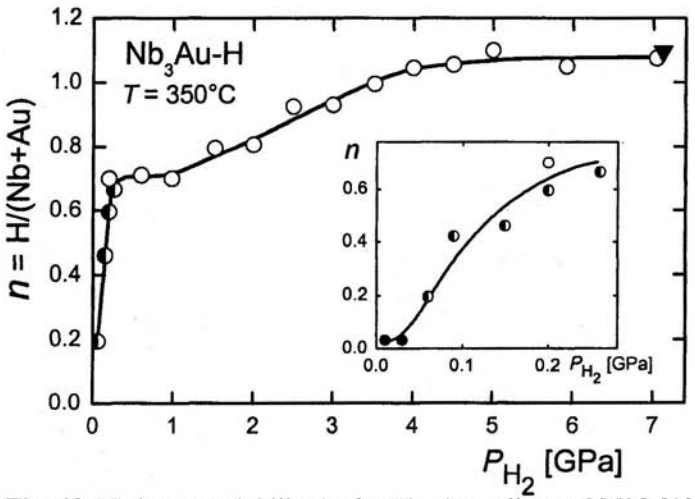

Fig. 43. Hydrogen solubility in the $Nb_{74}Au_{26}$ alloy at 325°C [120]. The filled and open circles stand for single-phase samples with the same A15 type of the metal lattice formed in two different intervals of the hydrogen concentration. The half-filled circles indicate two-phase samples. The filled triangle is for the $Nb_{74}Au_{26}$-D sample.

The neutron diffraction investigation of Nb_3AuH_x samples with $x = 2.9$ and 4.2 ($n = 0.73$ and 1.05, respectively) showed [135] that in both hydrides the hydrogen atoms occupy approximately 2.6 interstitial *d* sites, while the remaining hydrogen fills *i* sites. The plateau with $n \approx 0.7$–0.73 in the isotherm in Fig 43 extending from about 0.2 to 1.5 GPa is thus followed by a further increase in n due to the *i* sites filling at higher pressures, the occupancy of the *d* sites remaining approximately unchanged.

The crystal structure of Nb_3AuH_x is shown in Fig. 44. The Au atoms form a *bcc* lattice, in which Nb atoms occupy half of the tetrahedral interstitial sites (*c* positions). The other half of the tetrahedral sites (*d* positions) lie at the centers of tetrahedrons formed by nearest-neighbor Nb atoms and is partly filled with hydrogen occupying 2.6 of 3 sites available in the unit cell. The *i* sites lie in pairs along the <111> space diagonals inside asymmetrical tetrahedrons of three Nb atoms and one Au atom. The distance between the two *i* sites in a pair is about 0.62–0.66 Å and therefore they cannot be occupied by hydrogen at the same time due to the blocking effect [137] requiring that the distance between hydrogen atoms in a metal should not be much less than 2 Å. Occupancy of half of the *i* sites corresponds to $x = 4$ ($n = 1$), so the occupancy of these sites was about 2% in the Nb_3AuH_x sample with $x = 2.9$ and reached about 18% in the sample with $x = 4.2$.

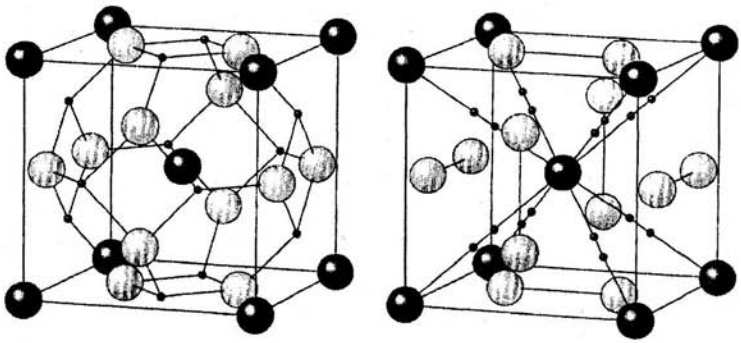

Fig. 44. Crystal structure of Nb_3AuH_x, space group $Pm3n$ [135]. Au atoms are shown as dark spheres, Nb as light spheres and the H interstices as small black spheres. In the left and right unit cell the interstitial d and i positions, respectively, are shown.

The X-ray [135] and Mössbauer [136] investigation revealed that the A15 metal lattice of the starting Nb_3Au compound and its hydrides was partly disordered, with about 8% of the regular Au positions randomly occupied by Nb. This atomic disorder explains the observed maximum concentration $x \approx 2.6$ of hydrogen on d sites under the assumption that hydrogen does not occupy d sites with one or more nearest-neighbor Nb atoms replaced by Au atoms. Strong repulsive interaction is characteristic of H and Au atoms dissolved in transition metals (see Ref. [138]).

The full crystal structures of hydrides of three other A15 compounds of Nb with Os, Ir and Pt have not been studied so far but, taking into account the affinity of hydrogen to niobium, the d positions look most favorable for hydrogen occupancy and should be filled first. For instance, one of A15 hydrides, Nb_3SnH_x with $x \approx 1$, was studied by neutron diffraction earlier [139] and shown to have hydrogen atoms randomly distributed over these very d positions. As the hydrogen content of the A15 hydrides in Ref. [120] significantly exceeded the maximum value $x = 3$ attainable with every d position filled, hydrogen atoms in those hydrides should partly occupy interstitials of another kind as well. Based on the effective radius of 0.56–0.60 Å of a hydrogen atom [137], occupation of the i positions is most likely.

Fig. 45 shows the T_c values of single-phase samples of the Nb_3Me-H and Nb_3Me-D solutions studied in Ref. [120]. The width of superconducting transition is relatively narrow in all samples except Nb_3Pt-H and Nb_3Pt-D with $n > 1.15$. Removal of hydrogen from the samples by vacuum annealing at 500°C restores the lattice parameter and T_c to the values characteristic of the initial Nb_3Me compounds. Again, the only exception is the Nb_3Pt-H and Nb_3Pt-D samples with $n > 1.15$. The annealing of these samples restores the lattice parameter, but T_c does not turn back to 9.2 K of the initial Nb_3Pt compound. Instead, the superconducting transition is stretched over a wide temperature interval from about 7 to 3 K. Presumably [120], this is due to changes in the atomic ordering of the metal lattice occurring in the course of synthesis

of such samples at a high hydrogen pressure. The strong dependence of T_c of Nb_3Pt on the degree of atomic order was noted earlier in Ref. [140].

As seen from Fig. 45, the T_c values of Nb_3Au-H solutions fall almost linearly at a rate of –8.9 K per H atom over the whole range of hydrogen contents studied. As hydrogen is on *d* sites in the solutions with $n < 0.75$ and fills both *d* and *i* sites at higher *n*, the superconducting temperature is insensitive to the type of interstitials occupied by hydrogen. Along with the hydrides, one sample of deuteride of each Nb_3Me compound was prepared at a deuterium pressure of 7 GPa and 325°C. Table 6 and Fig. 45 show that the deuterides have virtually the same composition, lattice parameter and T_c as the hydrides prepared under the same pressure and temperature. The absence of the T_c increase (the "inverse" isotope effect) when protium is replaced by deuterium suggests that optical H vibrations in the Nb_3Me-H solutions can play no significant role in the enhancement of superconductivity.

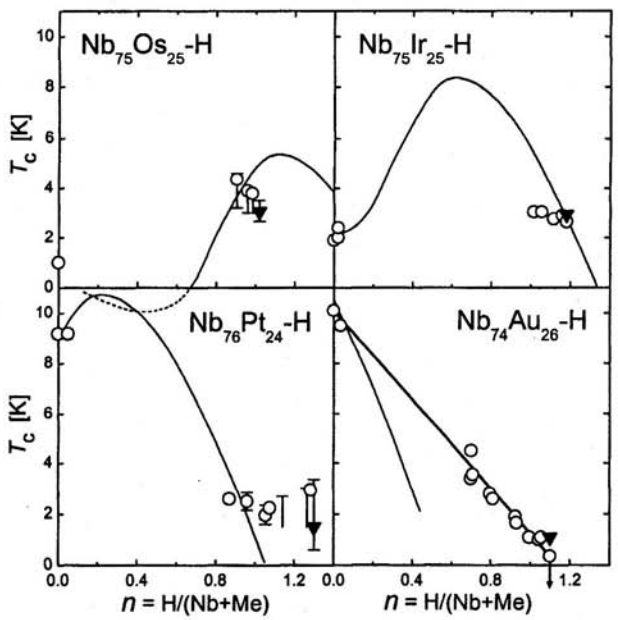

Fig. 45. Superconducting temperature T_c as a function of the hydrogen content *n* of single-phase samples of Nb_3Me-H (open circles) and Nb_3Me-D (filled triangles) solid solutions with the A15-type metal lattice [120]. The vertical bars show the width of the superconducting transition. The symbol with an arrow indicate the absence of superconductivity in the corresponding Nb_3Au-H sample at $T \geq 0.35$ K. The thin curves are the dependences $T_c(n) = T_c(N^e + \eta n) - \tau \cdot n$ calculated with $\eta = 0.5$ el./atom H and $\tau = 6$ K/atom H using the $T_c(N^e)$ dependence for the A15 compounds of Nb and Mo with 5*d*-metals, which is shown in Fig. 46 with the dashed curve. N^e is the electron concentration of the initial compound.

To visualize the effect of increase in the *d*-band filling with increasing hydrogen content, Fig. 46 gives the T_c values of single-phase Nb_3Me-H samples plotted against the effective electron concentration $N^e_{eff} = N^e + \eta n$ with $\eta = 0.5$ electron per H atom. In order not to complicate the diagram, the symbols mark only the limiting points of the composition intervals studied experimentally. As can be seen, the character of the $T_c(N^e_{eff})$ dependences of the Nb_3Me-H solutions agrees with the dependence $T_c(N^e)$ for Nb_3Me and Mo_3Me compounds [141] shown by the dashed curve. In particular, T_c of the Nb_3Os-H and Nb_3Ir-H solutions exceeds its value in the starting compounds without hydrogen, while hydrogenation of the Nb_3Au compound leads to a monotonic decrease of T_c.

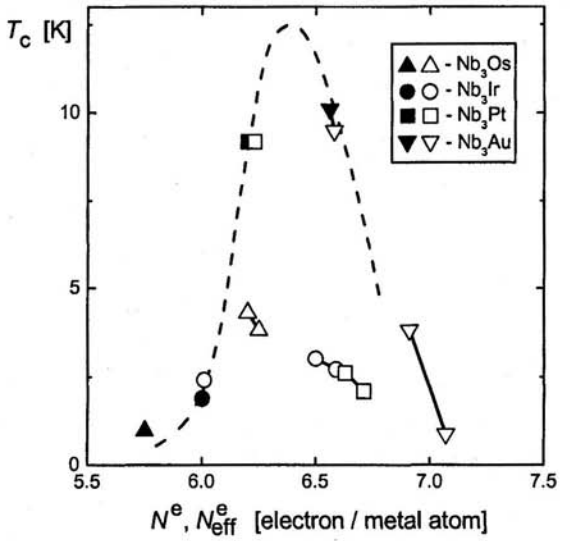

Fig. 46. Superconducting temperature T_c of the initial Nb_3Me samples (filled symbols) and of single-phase Nb_3Me-H samples (open symbols) as a function of the effective electron concentration $N^e_{eff} = N^e + \eta n$ with $\eta = 0.5$ electron per H atom [120]. N^e is the electron concentration of the initial compound; n is the H/(Nb+Me) atomic ratio. The dashed curve shows the $T_c(N^e)$ dependence for A15 compounds of Nb and Mo with 5*d*-metals [141].

Another fact demonstrating the applicability of the rigid band model to superconductivity of various Nb_3Me compounds and evidencing the significant role of *d*-band filling in the variation of T_c of these compounds on hydrogenation is the similarity between the $T_c(n)$ dependences of hydrogen solid solutions in Nb_3Ir (Fig. 45) and its isoelectronic analogue Nb_3Rh (Fig. 40b); see also Table 6. In both

systems, the starting compounds have close T_c values. T_c of the primary solutions steeply increases with increasing hydrogen concentration and T_c of the concentrated solutions decreases.

The effect of hydrogen on T_c of one more A15 compound, $Nb_3Au_{0.75}Ir_{0.25}$, was studied in Ref. [142]. The compound had T_c = 7.3 K instead of 12.5 K corresponding to its electron concentration N^e = 6.375 el./atom (see the dashed curve in Fig. 46) because the sample was not annealed after melting and was in a non-equilibrium state. A two-phase sample of $Nb_3Au_{0.75}Ir_{0.25}$-H prepared at a hydrogen pressure of 0.1 GPa and 100°C had the mean value of n = 0.475 and T_c = 3.2 K. The decrease in T_c of the $Nb_3Au_{0.75}Ir_{0.25}$ compound on hydrogenation is in line with the expected $T_c(N^e_{eff})$ dependence.

In principle, the agreement of the experimental results for the A15 compounds with the $T_c(N^e)$ curve in Fig. 46 can be considerably improved by taking a different value of η for each Nb_3Me-H system. For example, $\eta \approx 0.35$ el. per H atom puts the $T_c(N^e_{eff})$ values of the Nb_3Os-H hydrides on the ascending side of the $T_c(N^e)$ curve and $\eta \approx 0.7$ el. per H atom places the points for the Nb_3Ir-H and Nb_3Pt-H hydrides onto the descending side of that curve. However, as the analysis of the $T_c(n)$ dependence for the σ-type $Nb_{65}Rh_{35}$-H solutions shows, this additional fitting is unlikely to have physical significance.

In contrast to the Nb_3Me-H solutions with a large miscibility gap that brings uncertainty in the interpretation of the experimental results, the $Nb_{65}Rh_{35}$ σ-alloy forms with hydrogen a continuous solution (Fig. 41). This makes it possible to track the $T_c(N^e_{eff})$ dependence over a wide range of electronic concentrations and to compare it with the $T_c(N^e)$ dependence for σ-alloys without hydrogen. Regretfully, such a dependence for σ-alloys of Nb with 4*d*-metals is not constructed yet, but it should be qualitatively the same as that [133,134] for the σ-alloys of Nb with 5*d*-metals Re, Os, Ir and Pt. The T_c values of the latter are close to 2 K and nearly independent of N^e in the range $6 \le N^e \le 6.5$ el./atom. At higher electron concentrations, they increase at a rate of about 10 K per electron per atom, reach a maximum of about 5 K at $N^e \approx 6.7$–6.8 el./atom and then begin to decrease. As seen from Table 5, the $Nb_{65}Rh_{35}$ alloy has N^e = 6.4 el./atom and the effective concentration N^e_{eff} of the $Nb_{65}Rh_{35}$-H solutions reaches 6.7–6.8 el./atom at n =0.6–0.8. However, instead of a steep increase up to the maximum value at n =0.6–0.8, the superconducting temperature of the $Nb_{65}Rh_{35}$-H solutions nearly does not change at hydrogen contents up to $n \sim 1$ and then decreases (Fig. 41b).

It is therefore very likely that, alongside with the filling of the *d*-band of the $Nb_{65}Rh_{35}$ alloy, another mechanism is at work to reduce T_c as n increases. To flatten the maximum of the $T_c(N^e_{eff})$ dependence for the $Nb_{65}Rh_{35}$-H σ-solutions, that mechanism should decrease T_c at a rate of about -5 to -10 K per H atom. A nearly linear decrease of T_c at a similar rate of about -15 K per H atom was observed for hydrogen solutions in the *bcc* Nb-Ti alloys (Fig. 42b). The superconducting

temperature of the Nb-Ti alloys slightly varying with N^e, the decrease in T_c under hydrogenation is almost entirely governed by a mechanism not directly related to the change in the *d*-band filling. With the two contributions taken together, the $T_c(n)$ dependences for the $Nb_{65}Rh_{35}$-H and Nb-Ti-H solutions can be written as

$$T_c(n) \approx T_c(N^e + 0.5n) - \tau \cdot n \equiv T_c(N^e_{eff}) - \tau \cdot n \qquad (2)$$

where τ is the constant of the order of 5 to 15 K per H atom.

This formula also explains why ε-MoH has T_c as low as 0.92 K (Table 4) though its $N^e_{eff} \approx 6.5$ el./atom corresponds to the position of the pronounced maximum of the Matthias curve. It explains the relatively low $T_c \approx 1.7$–2 K of γ′ dihydrides of the $Nb_{88}Rh_{12}$ alloy (Table 5) with $N^e_{eff} \approx 6.3$–6.5 el./atom. With $\tau = 6$ K per H atom, Eq. (2) gives a semi-quantitative description for the experimental $T_c(n)$ dependences of hydrogen solid solutions in the A15 compounds of Nb with Os, Ir and Pt (thin curves in Fig. 45). It also describes the $T_c(n)$ dependence for the primary Nb_3Au-H solutions with $n \leq 0.03$, but seems to fail in the case of concentrated solutions in this system (Fig. 45). (It is however difficult to judge at the moment if Eq. (2) is really inapplicable to the Nb_3Au-H hydrides since their N^e_{eff} values lie in the yet unexplored interval of the $T_c(N^e)$ dependence for A15 alloys without hydrogen, see Fig. 46.)

In any case, for a rather large variety of alloys, the variation of T_c on hydrogenation due to the increasing *d*-band filling is obviously accompanied by its steady and steep decrease caused by some other mechanism. As was first noted in Ref. [120], the decrease could result from the hardening of acoustic phonon modes of the host metal. An increase in the mean frequency of acoustic vibrations due to dissolved hydrogen has been observed for *bcc* Nb and Ta [132] and can be characteristic of many other transition metals and alloys as well. It must be noted, however, that the hardening of acoustic phonon modes of the metal on hydrogenation is not an obligatory effect. For instance, the mean frequency of acoustic vibrations in *fcc* hydrides of Pd and Ni is lower, respectively, than in pure *fcc* Pd and Ni [143], and this is one of the reasons why *fcc* PdH has the highest T_c value among hydrides of *d*-metals and alloys. A new low-energy mode lying in the acoustic range is responsible for superconductivity of the metastable Ti-H phases [52].

3.9. Hydrides of HfRh and ZrRu compounds

Along with the A15 compounds, HfRh and ZrRu compounds also belong to the $A_{1-y}(B,C, \ldots)_y$ alloys of the (*ii*) type discussed at the beginning of Section 3.8 (A ≡ Hf, Ru and B, C, … ≡ Ru, Rh, Pd, Pt, …). The behavior of physical properties of such alloys with varying the relative concentrations of elements B, C, … usually well obeys

the rigid band model. In particular, the $T_c(N^e)$ dependence exhibits a large broad peak centered at $N^e \approx 6.3$–6.7 el./atom.

In the work of Ref. [121], hydrides of the HfRh and ZrRu compounds were synthesized in an H_2 atmosphere at 325°C and pressures up to 7 GPa. These samples and also two samples of deuterides of HfRh and ZrRu prepared at 7 GPa and 325°C were X-rayed at 100 K and analyzed for superconductivity at temperatures down to 1.5 K. The full crystal structures of the initial HfRu compound and its hydride and deuteride were studied by neutron diffraction at 120 K. The results are presented in Table 5 and in Figs. 47 and 48.

As can be seen from Fig. 47, at 325°C the hydrogen solubility in the CsCl-type lattice of HfRu and ZrRu is very low, until at pressures of about 2 and 0.7 GPa, respectively, hydrides with a different structure of the metal lattice begin to form. The hydrogen content of the single-phase hydrides of HfRu was $n \approx 1.8$ and did not depend on the pressure. That for the ZrRu hydrides monotonically increased with pressure from $n \approx 0.8$ at 1 GPa to $n \approx 1.1$ at 7 GPa.

Both HfRu and ZrRu hydrides turned out to be superconductors with higher T_c than the initial compounds without hydrogen (Fig. 48). Within experimental error the T_c values of the hydrides were independent of the pressure of the synthesis and, in the case of the ZrRu hydrides, of the hydrogen content. The T_c values of the deuterides did not differ from those for the hydrides.

According to the X-ray diffraction data, both HfRu and ZrRu hydrides have an orthorhombic metal lattice of the CrB type. The full crystal structure of HfRu hydride and deuteride determined by neutron diffraction is of the $ZrNiH_3$ type. A schematic drawing of this structure is given in Ref. [137].

The HfRu and ZrRu compounds have $N^e = 6$ el./atom and the effective electron concentration of their hydrides is $N^e_{eff} = N^e + 0.5n \approx 6.9$ and 6.4–6.55 el./atom, respectively. These values fall into the peak region of the Matthias plot. The superconducting temperature is therefore expected to increase on hydrogenation of the alloys, which is, indeed, observed (Table 5). The equality of the T_c values for the hydride and deuteride of HfRu as well as ZrRu indicates that the interaction of the conduction electrons with optical vibrations of the hydrogen or deuterium, respectively, that predominates and gives rise to a substantial isotope effect in PdH/PdD, is hardly at work in the present case.

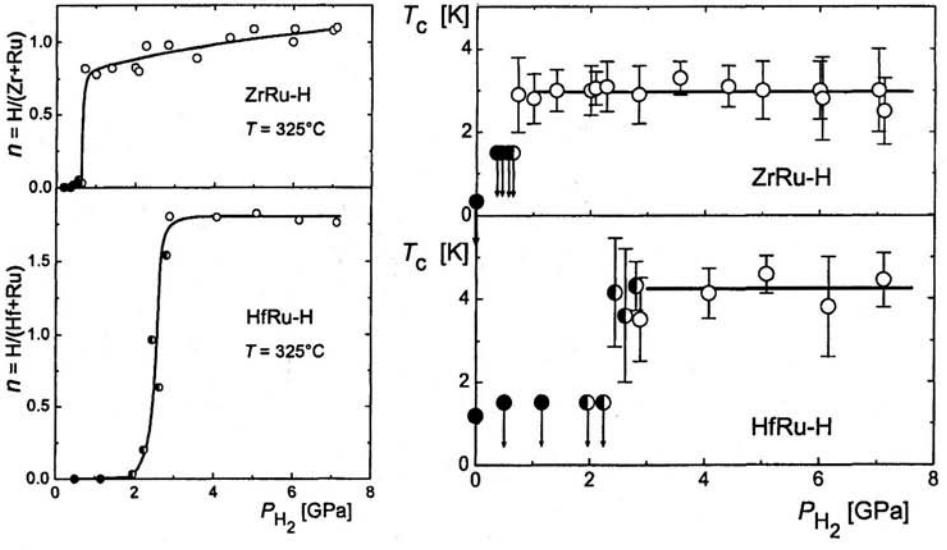

Fig. 47 (left). Hydrogen solubility in the ZrRu and HfRu compound at 325°C [121]. The filled and open circles stand for single-phase samples with the cubic CsCl-type and the orthorhombic CrB-type metal lattice, respectively The half-filled circles indicate two-phase samples.

Fig. 48 (right). Superconducting temperature T_c of ZrRu-H and HfRu-H samples as a function of the hydrogen pressure of their synthesis at 325°C [121]. The filled and open circles stand for single-phase samples with the CsCl-type and CrB-type metal lattice, respectively. The half-filled circles refer to two-phase samples. The symbols with arrows signify the absence of superconductivity at temperatures above the indicated. The vertical bars show the 10%–90% width of the superconducting transition.

An interesting observation was the CrB type metal lattice structure of the HfRu and ZrRu hydrides. This is the structure of the HfPt and ZrPt compounds [144], whose electron number, $N^e = 7$ el./atom, is close to the N^e_{eff} of the HfRu and ZrRu hydrides. This fact shows that effective electron numbers near 7 el./atom favor this structure. In fact, there are more and more indications that the crystal structures of transition metals and alloys, with the possible exception of ferromagnetic Fe, Co and Ni, are to a large extent determined by the *d*-band filling and, as a consequence, by the electron concentration N^e. In particular, because of a strong dependence of the superconducting properties of the metals upon their crystal structure, the existence of the Matthias rule implies by itself such a correlation.

With correlations of this kind existing in pure metals as well as their alloys and intermetallic compounds, one should also expect similar correlations between the crystal structures and N^e_{eff} of the hydrides of transition metals and their alloys. There is, indeed, evidence for such correlations. For example, most hydrides with $6.1 \leq N^e_{eff} \leq 7.1$ el./atom have closed packed metal lattices (*hcp*, *fcc* and their slightly distorted modifications, see Tables 4 and 5) characteristic of most *d*-metals and alloys with N^e in the same range. This extension of the rigid *d*-band model also accounts for the crystal structures of higher hydrides of the 3*d*-metals Fe, Co and Ni (N^e = 8, 9, and 10 el./atom). As one can see from Fig. 20, iron hydride is *dhcp* like Co metal doped with Fe [145], CoH is *fcc* like Ni, and NiH is *fcc* like Cu (N^e = 11 el./atom). It is interesting to note that the calculated crystal structures of ferromagnetic Fe, Co and Ni are notoriously incorrect because of a large magnetic contribution to the total energy of the crystals which is difficult to evaluate [146]. The rigid *d*-band model describes the magnetic properties of the hydrides [4,119] in a satisfactory way and thus takes this magnetic contribution into account automatically.

For the 4*d*- and 5*d*-metals and alloys, the most convincing observation is the above mentioned CrB type metal structure of the HfRu and ZrRu hydrides, but other examples can also be given. For instance, as seen from Table 4 and Fig. 20, the metal lattice of the hydride of Rh (N^e = 9 el./atom) is *fcc* as that of Pd (N^e = 10 el./atom), and the metal lattice of the hydride of Pd (N^e = 10 el./atom) is *fcc* like that of Ag (N^e = 11 el./atom). In the case of the type (*ii*) Nb_3Me alloys (Me = Os, Ir, Pt and Au) with N^e ranging from 5.75 to ≈6.5 el./atom, the hydrides all have the same A15 metal structure as the starting alloys (Table 6). The model predicts this at least for the cases with Me = Os, Ir and Pt.

The applicability of the rigid *d*-band model for the description of the crystal structures of hydrides is certainly much more limited than for the description of their physical properties, since there are many additional factors affecting the formation of hydrides. In particular, the interstices in the metal lattice of the hydride must be of a size appropriate for the accommodation of hydrogen atoms. Moreover, the structures with minimum specific volume are preferentially formed if the synthesis is done under high pressure. The success of the model thus shows that, for many groups of alloys, *d*-band filling dominates over other mechanisms governing hydride formation. It is interesting to note that the dominating role of the increase in the electron concentration in the formation of interstitial phases has already been discussed long ago [147] for solid solutions of carbon in the *d*-metals of Groups V and VI.

4. CONCLUSIONS

The application of high-pressure techniques to the synthesis of hydrides of transition metals and alloys resulted in the discovery of a number of new superconducting phases and made it possible to outline principle features of the effect of hydrogen on superconductivity in function of the position of the metals in the periodic table.

Hydrogenation of palladium located in the rightmost column of *d*-elements makes it a superconductor with a relatively high value of $T_c \approx 9$ K at H/Pd = 1 due to a large contribution of anomalously soft modes of optic H vibrations in the attractive electron-electron interaction.

Titanium that belongs to the leftmost Group IV forms superconducting χ-, η- and κ-hydrides with H/Ti ≈ 0.7–0.9 and $T_c \approx 4$ K. The occurrence of superconductivity in the Ti hydrides is attributed to the interaction between electrons and low-energy excitations specific to the vibrational spectrum of these very phases.

The influence of dissolved hydrogen on the superconductivity of *d*-metals of intermediate groups and of most alloys can be explained by combination of two effects. One is due to the filling of the *d*-band with the electrons supplied by the hydrogen. This can lead to the T_c changes of either sign depending on the electronic structure of the metal. Another effect is the monotonic decrease in T_c with increasing hydrogen concentration at a rate of –5 to –15 K per H atom. Presumably, this is due to the hydrogen-induced hardening of the acoustic modes of the host metal. Combining the two effects, for example, provides an explanation for the occurrence of $T_c \approx 0.9$ K in the hydride of molybdenum and in the dihydride of the $Nb_{88}Rh_{12}$ alloy. It also explains the T_c *vs.* H/Me dependences of hydrogen solid solutions in Tc, Ru, Re and in the A15-type, α-type and *bcc* alloys of Nb.

REFERENCES

[1] C.B. Satterthwaite and I.L. Toepke, *Phys. Rev. Lett.* **25** (1970) 741.

[2] T. Skoskiewicz, *Phys. Stat. Sol. (a)* **11** (1972) K123.

[3] B. Stritzker and H. Wühl, in *Topics in Appl. Phys.*, vol. 29, *Hydrogen in Metals II*, eds. G. Alefeld and J. Völkl (Springer-Verlag, Berlin) 1978, p. 243.

[4] E.G. Ponyatovsky, V.E. Antonov and I.T. Belash, in *Problems in Solid-State Physics*, eds. A.M. Prokhorov and A.S. Prokhorov (Mir Publishers, Moscow) 1984, p.109.

[5] E.G. Ponyatovskii, I.O. Bashkin, V.F. Degtyareva, V.I. Rashchupkin, O.I. Barkalov and Yu.A. Aksenov, *Sov. Phys. – Solid State* **27** (1985) 2077.

[6] E.G. Ponyatovskii and I.O. Bashkin, *Z. Phys. Chem.* **146** (1985) 137.

[7] A. San-Martin and F.D. Manchester, *Bull. Alloy Phase Diagrams* **8** (1987) 30.

[8] I.O. Bashkin, A.F. Gurov, V.Yu. Malyshev and E.G. Ponyatovsky, *Sov. Phys. – Solid State* **34** (1992) 674.

[9] A.M. Balagurov, I.O. Bashkin, A.I. Kolesnikov, V.Yu. Malyshev, G.M. Mironova, E.G. Ponyatovsky and V.K. Fedotov, *Sov. Phys. – Solid State* **33** (1991) 711.

[10] A.I. Kolesnikov, A.M. Balagurov, I.O. Bashkin, V.K. Fedotov, V.Yu. Malyshev, G.M. Mironova and E.G. Ponyatovsky, *J. Phys.: Condens. Matter* **5** (1993) 5045.

[11] I.O. Bashkin, A.F. Gurov, V.Yu. Malyshev and E.G. Ponyatovsky, *Sov. Phys. – Solid State* **34** (1992) 1386.
[12] I.O. Bashkin, V.Yu. Malyshev and E.G. Ponyatovsky, *Z. Phys. Chem.* **179** (1993) 111.
[13] I.O. Bashkin, V.Yu. Malyshev and E.G. Ponyatovsky, *Z. Phys. Chem.* **179** (1993) 289.
[14] I.O. Bashkin, V.Yu. Malyshev and M.M. Myshliaev, *Sov. Phys. – Solid State* **34** (1992) 1182.
[15] A.I. Kolesnikov, A.M. Balagurov, I.O. Bashkin, A.V. Belushkin, E.G. Ponyatovsky and M. Prager, *J. Phys.: Condens. Matter* **6** (1994) 8977.
[16] A.I. Kolesnikov, I.O. Bashkin, A.V. Belushkin, E.G. Ponyatovsky and M. Prager, *J. Phys.: Condensed Matter* **6** (1994) 8989.
[17] D.N. Mogilyansky, I.O. Bashkin, V.F. Degtyareva, V.Yu. Malyshev and E.G. Ponyatovskii, *Sov. Phys. – Solid State* **32** (1990) 1039.
[18] I.O. Bashkin, A.I. Kolesnikov and E.G. Ponyatovsky, *High Pressure Research*, **14** (1995) 91.
[19] I.O. Bashkin, V.K. Fedotov, H.-J. Hesse, A. Schiwek, W.B. Holzapfel and E.G. Ponyatovsky, *J. Phys.: Condensed Matter* **14** (2002) 955.
[20] E.G. Ponyatovskii, I.O. Bashkin and Yu.A. Aksenov, *Fiz. Metallov i Metallovedenie* **64** (1987) 1110 {in Russian}.
[21] E.G. Ponyatovsky, I.O. Bashkin, V.F. Degtyareva, Yu.A. Aksenov, V.I. Rashchupkin and D.N. Mogilyansky, *J. Less-Common Metals* **129** (1987) 93.
[22] I.O. Bashkin, V.Yu. Malyshev, V.I. Rashchupkin and E.G. Ponyatovsky, *Sov. Phys. – Sol. State* **30** (1988) 1155.
[23] I.O.Bashkin, *Z. Phys. Chem.* **163** (1989) 469.
[24] I.O. Bashkin, T.I. Dyuzheva, L.M. Lityagina and V.Yu. Malyshev, *Phys. Solid State* **35** (1993) 1528.
[25] K. Nakamura and Y. Fukai, *J. Alloys Compds* **231** (1995) 46.
[26] I.O. Bashkin, V.K. Fedotov, H.-J. Hesse, A. Schiwek, W.B. Holzapfel and E.G. Ponyatovsky, *High Pressure Research* **17** (2000) 217.
[27] E.Yu. Tonkov, *High Pressure Phase Transformations*, vol. 2 (Gordon & Breach, Philadelphia) 1992, p. 682.
[28] H. Numakura, M. Koiwa, H. Asano and F. Izumi, *Acta Metall.* **36** (1988) 2267.
[29] I.O. Bashkin, A.I. Kolesnikov, E.G. Ponyatovsky, A.M. Balagurov and G.M. Mironova, *Phys. Solid State* **37** (1995) 2065.
[30] R.M. Wood, *Proc. Phys. Soc. London* **80** (1962) 783.
[31] J.C. Jamieson, *Science* **140** (1963) 72.
[32] N.F. Miron, V.I. Shcherbak, V.N. Bykov and V.A. Levdik, *Sov. Phys. – Crystallogr.* **19** (1974) 468.
[33] I.O. Bashkin, A.I. Kolesnikov, V.Yu. Malyshev, E.G. Ponyatovsky, S. Borbely, L. Rosta and G. Pepy, *J. de Physique IV* (Colloque C8, Suppl. J. de Physique I, No. 12) **3** (1993) 290.
[34] O.T. Woo, G.C. Weatherly, C.E. Coleman and R.W. Gilbert, *Acta Metall.* **33** (1985) 1897.

[35] C. Korn, *Phys. Rev. B* **28** (1983) 95.
[36] H.L. Yakel, *Acta Cryst.* **11** (1958) 46.
[37] T.I. Dyuzheva, L.M. Lityagina, S.S. Kabalkina and M.E. Kost, *Fiz. Tverd. Tela* **33** (1991) 2763 {in Russian}.
[38] I. Schober and H. Wenzl, in: *Topics in Appl. Phys.*, vol. 29: *Hydrogen in Metals II*, eds. G. Alefeld and J. Völkl (Springer-Verlag, Berlin) 1978, p. 11.
[39] I.O. Bashkin, M.V. Nefedova, V.G. Tissen and E.G. Ponyatovsky, *Phys. Solid State* **40** (1998) 1950.
[40] V.M. Teplinskii, I.O. Bashkin, V.Yu. Malyshev and E.G. Ponyatovsky, *Sov. Phys. – Solid State* **31** (1989) 225.
[41] M. Gurvitch, *Phys. Rev. Lett.* **56** (1986) 647.
[42] U. Mizutani, *Prog. Mat. Sci.* **28** (1983) 97.
[43] B. Stritzker and J.D. Meyer, *Z. Phys. B* **38** (1980) 77.
[44] J.D. Meyer and B. Stritzker, *Physics of Transition Metals* (Inst. Phys. Conf. Ser. No. 55: Ch. 11, London) 1981, p. 591.
[45] X.W. Lin, M.O. Ruault, A. Traverse, J. Chaumont, M. Salome and H. Bernas, Phys. Rev. Lett. **56** (1986) 1835.
[46] I.O. Bashkin, A.I. Latynin and V.Yu. Malyshev, *Fiz. Tverd. Tela* **37** (1995) 2108 {in Russian}.
[47] I.O. Bashkin, M.V. Nefedova and V.G. Tissen, *Phys. Solid State* **42** (2000) 11.
[48] I.O. Bashkin, I.M. Barkalov, A.I. Bolshakov, V.Yu. Malyshev and E.G. Ponyatovskii, *Sov. Phys. – Solid State* **32** (1990) 1556.
[49] C. Korn and S.D. Goren, *Phys. Rev. B* **33** (1986) 64.
[50] H. Wipf, B. Kappesser and R. Werner, *J. Alloys Compds* **310** (2000) 190.
[51] A.I. Kolesnikov, V.K. Fedotov, I. Natkaniec, S. Khabrylo, I.O. Bashkin and E.G. Ponyatovsky, *JETP Lett.* **44** (1986) 509.
[52] A.I. Kolesnikov, M. Monkenbush, M. Prager, I.O. Bashkin, V.Yu. Malyshev and E.G. Ponyatovsky, *Z. Phys. Chem. NF* **163** (1989) 709.
[53] G.M. Vujičić, V.L. Aksenov, N.M. Plakida and S. Stamenković, *J. Phys. C: Solid State Phys.* **14** (1981) 2377.
[54] S.L. Drechsler, G.M. Vujičić and N.M. Plakida, *J. Phys. F: Metal Phys.* **14** (1984) L243.
[55] T. Galbaatar, N.M. Plakida and S.-L. Drechsler, *Z. Phys. B* **77** (1989) 387.
[56] V.E. Antonov, *J. Alloys Compds* **330-332** (2002) 110.
[57] E. Wicke and H. Brodowsky, in: *Topics in Appl. Phys.*, vol. 29: *Hydrogen in Metals II*, eds. G. Alefeld and J. Völkl (Springer-Verlag, Berlin) 1978, p. 73.
[58] B. Baranowski, *Ber. Bunsenges. Phys. Chem.* **76** (1972) 714.
[59] M. Hanson, H.R. Khan, A. Knödler and Ch.J. Raub, *J. Less-Common Metals* **43** (1975) 93.

[60] H.R. Khan and Ch.J. Raub, *J. Less-Common Metals* **49** (1976) 399.
[61] V.E. Antonov, I.T. Belash, O.V. Zharikov and A.V. Palnichenko, *Phys. Stat. Sol. (b)* **142** (1987) K155.
[62] B.N. Ganguly, *Z. Physik* 265 (1973) 433; *Phys. Lett. A* **46** (1973) 23.
[63] V.E. Antonov, I.T. Belash, V.Yu. Malyshev, E.G. Ponyatovsky, *Platinum Metals Review* **28** (1984) 158 [Reprinted in: *Int. J. Hydrogen Energy* **11** (1986) 193].
[64] V.I. Spitsyn, V.E. Antonov, O.A. Balakhovskii, I.T. Belash, E.G. Ponyatovskii, V.I. Rashupkin and V.Sh. Shekhtman, *Dokl. Akad. Nauk SSSR* **260** (1981) 132 {in Russian}.
[65] V.P. Glazkov, A.V. Irodova, V.A. Somenkov, S.Sh. Shil'shtein, V.E. Antonov and E.G. Ponyatovskii, *Fiz. Tverd. Tela (Leningrad)* **26** (1984) 3261 {Engl. Transl.: *Sov. Phys. – Solid State* **26** (1984) 1961}.
[66] V.E. Antonov, I.T. Belash, K.G. Bukov, O.V. Zharikov, A.V. Pal'nichenko and V.M. Teplinskiy, *Fiz. Metallov i Metallovedenie* **68** (1989) 1198 {in Russian}.
[67] V.E. Antonov, I.T. Belash, O.V. Zharikov, A.I. Latynin and A.V. Palnichenko, *Fiz. Tverd. Tela (Leningrad)* **30** (1988) 598 [Engl. Transl.: *Sov. Phys. – Solid State* **30** (1988) 344].
[68] B. Dorner, I.T. Belash, E.L. Bokhenkov, E.G. Ponyatovsky, V.E. Antonov and L.N. Pronina, *Solid State Commun.* **69** (1989) 121.
[69] D.K. Ross, V.E. Antonov, E.L. Bokhenkov, A.I. Kolesnikov, E.G. Ponyatovsky and J. Tomkinson, *Phys. Rev. B* **58** (1998) 2591.
[70] B. Stritzker, *Z. Phys.* **268** (1974) 261.
[71] T. Skośkiewicz, *High Temp. – High Pressures* **7** (1975) 684.
[72] T. Skośkiewicz, *Phys. Stat. Sol. (a)* **48** (1978) K165.
[73] L. Sniadower, L. Dumoulin, P. Nedellec and J.P. Burger, in: *Metal-Hydrogen Systems*, ed. T.N. Veziroğlu (Pergamon, Oxford) 1982, p. 357.
[74] J.C.M. van Dongen and J.A. Mydosh, *Z. Physik. Chem. N. F.* **116** (1979) 149.
[75] J.E. Schirber, *Phys. Lett. A* **45** (1973) 141.
[76] T. Skośkiewicz, A.W. Szafrański and B. Baranowski, *Phys. Stat. Sol. (b)* **59** (1973) K135.
[77] C.B. Friedberg, J.S. Pickel, A.F. Rex and J. Ruvalds, *Solid State Commun.* **29** (1979) 407.
[78] C.B. Friedberg, A.F. Rex and J. Ruvalds, *Phys. Rev. B* **19** (1979) 5694.
[79] H. Brodowsky and J. Fleischhauer, *Z. Naturforschung A* **38** (1983) 676.
[80] V.E. Antonov, I.T. Belash, E.G. Ponyatovskii and V.I. Rashupkin, *Zh. Eksp. Teor. Fiz., Pisma* **31** (1980) 451 {Engl. Transl.: *JETP Lett.* **31** (1980) 422}.
[81] P. Hertel, *Z. Phys.* **268** (1974) 111.
[82] B.N. Ganguly, *Z. Physik B* **22** (1975) 127.
[83] D.A. Papaconstantopoulos, E.N. Economou, B.M. Klein and L.L. Boyer, *Phys. Rev. B* **20** (1979) 177.
[84] K.H. Bennemann and J.W. Garland, *Z. Phys.* **260** (1973) 367.
[85] G. Wolf, J. Jahnke and K. Bohmhammel, *Phys. Stat. Sol. (a)* **36** (1976) K125.
[86] B. Stritzker, *Phys. Rev. Lett.* **42** (1979) 1769.

[87] G. Gladstone, M.A. Jensen and J.R. Schrieffer, in: *Superconductivity*, vol. 2, ed. R.D. Parks (Marcel Dekker, New York) 1969.

[88] V.F. Degtyareva, V.E. Antonov, I.T. Belash and E.G. Ponyatovskii, *Phys. Stat. Sol. (a)* **66** (1981) 77.

[89] V.E. Antonov, T.E. Antonova, I.T. Belash and E.G. Ponyatovskii, *Fiz. Metallov i Metallovedenie* **57** (1984) 671 {in Russian}.

[90] A.V. Irodova, V.P. Glazkov, V.A. Somenkov, V.E. Antonov and E.G. Ponyatovsky, *Z. Phys. Chem. N. F.* **163** (1989) 53.

[91] A.I. Kolesnikov, V.E. Antonov, A.M. Balagurov, S. Bennington and M. Prager, *J. Phys.: Condens.Matter* **6** (1994) 9001.

[92] V.E. Antonov, T.E. Antonova, I.T. Belash, V.Yu. Malyshev and V.I. Rashupkin, *Phys. Stat. Sol. (a)* **81** (1984) K185.

[93] V.E. Antonov, T.E. Antonova, I.T. Belash, E.G. Ponyatovskii and V.I. Rashupkin, *Phys. Stat. Sol. (a)* **77** (1983) K23.

[94] V.E. Antonov, T.E. Antonova, I.T. Belash, E.G. Ponyatovskii, V.I. Rashupkin and V.G. Thiessen, *Phys. Stat. Sol. (a)* **77** (1983) 71.

[95] V.E. Antonov, T.E. Antonova, I.T. Belash, E.G. Ponyatovskii and V.I. Rashupkin, *Phys. Stat. Sol. (a)* **78** (1983) 137.

[96] A. Maeland and T.B. Flanagan, *J. Phys. Chem.* **68** (1964) 1419.

[97] B. Baranowski, F.A. Lewis, S. Majchrzak and R. Wiśniewski, *Trans. Faraday Soc.* **68** (1972) 653.

[98] C.G. Robbins, M. Ishikawa, A. Treyvaud and J. Muller, *Solid State Commun.* **17** (1975) 903.

[99] H. Oesterreicher and J. Clinton, *J. Solid state Chem.* **17** (1976) 443.

[100] C.G. Robbins and J. Muller, *J. Less-Common Metals* **42** (1975) 19.

[101] V.E. Antonov, T.E. Antonova, I.T. Belash, E.G. Ponyatovskii and V.I. Rashupkin, *Fiz. Tverd. Tela (Leningrad)* **29** (1987) 1017 {Engl. Transl.: *Sov. Phys. – Solid State* **29** (1987) 582}.

[102] V.E. Antonov, T.E. Antonova, I.T. Belash, O.V. Zharikov, A.V. Palnichenko, E.G. Ponyatovskii and V.I. Raschupkin, *Fiz. Tverd. Tela (Leningrad)* **30** (1988) 2152 {Engl. Transl.: *Sov. Phys. – Solid State* **30** (1988) 1240}.

[103] V.E. Antonov, I.T. Belash, E.G. Ponyatovskii, V.I. Rashupkin and I.M. Romanenko, *Fiz. Tverd. Tela (Leningrad)* **29** (1987) 665 [Engl. Transl.: *Sov. Phys. – Solid State* **29** (1987) 381}.

[104] V.E. Antonov, T.E. Antonova, I.T. Belash, V.Yu. Malyshev, E.G. Ponyatovskii and V.I. Rashupkin, *Fiz. Tverd. Tela (Leningrad)* **28** (1986) 2352 {Engl. Transl.: *Sov. Phys. – Solid State* **28** (1986) 1316}.

[105] V.E. Antonov, T.E. Antonova, I.T. Belash and V.I. Raschupkin, *High Pressure Research* **1** (1989) 315.

[106] H. Peisl, in: *Topics in Appl. Phys.*, vol. 28: *Hydrogen in Metals I*, eds. G. Alefeld and J. Völkl (Springer-Verlag, Berlin) 1978, p. 53.

[107] V.E. Antonov, B. Dorner, V.K. Fedotov, G. Grosse, A.S. Ivanov, A.I. Kolesnikov, V.V. Sikolenko and F.E.Wagner, *J. Alloys Compds* **330-332** (2002) 462.

[108] B. Baranowski, S. Majchrzak and T.B. Flanagan, *J. Phys. F: Metal Phys.* **1** (1971) 258.
[109] V.A. Somenkov and S.Sh. Shil'shtein, *Phase Transformations of Hydrogen in Metals* (Institute of Atomic Energy, Moscow) 1978.
[110] B. Dorner, V.E. Antonov, I.T. Belash, E.L. Bokhenkov, E.G. Poniatovsky and L.N. Pronina, *Z. Phys. Chem. N. F.* **164** (1989) 1079.
[111] D.K. Ross, P.F. Martin, W.A. Oates and R.K. Bakhsh, *Z. Phys. Chem. N. F.* **114** (1979) 221.
[112] V.E. Antonov, K. Cornell, B. Dorner, V.K. Fedotov, G. Grosse, A.I. Kolesnikov, F.E. Wagner and H. Wipf, *Solid State Commun.* **113** (2000) 569.
[113] E. Raub and W. Fritzsche, *Z. Metallkde* **54** (1963) 317.
[114] E. Raub, H. Beeskow and W. Fritzsche, *Z. Metallkde* **54** (1963) 451.
[115] C.B. Satterthwaite and D.T. Peterson, *J. Less-Common Metals* **26** (1972) 361.
[116] A.F. Andersen and A.J. Maeland, *J. Less-Common Metals* **129** (1987) 115.
[117] E.M. Savitskii, Yu.V. Efimov, Ch.J. Raub and H.R. Khan, *Superconductivity of Noble-Metal Alloys* (Izd. Metallurgiya, Moscow) 1985 {in Russian}.
[118] B.T. Matthias, *Phys. Rev.* **97** (1955) 74.
[119] V.E. Antonov, I.T. Belash, V.F. Degtyareva, D.N. Mogilyansky, B.K. Ponomarev and V.Sh. Shekhtman, *Int. J. Hydrogen Energy* **14** (1989) 371.
[120] V.E. Antonov, T.E. Antonova, I.T. Belash, O.V. Zharikov, A.I. Latynin, A.V. Pal'nichenko and V.I.Rashchupkin, *Fiz. Tverd. Tela (Leningrad)* **31** (1989) 12 {Engl. Transl.: *Sov. Phys. – Solid State* **31** (1989) 1659}.
[121] V.E. Antonov, E.L. Bokhenkov, A.I. Latynin, V.I. Rashupkin, B. Dorner, M. Baier and F.E. Wagner, *J. Alloys Compds* **209** (1994) 291.
[122] V.E. Antonov, in: *Stability of Materials*, eds. A. Gonis, P.E.A. Turchi and J. Kudrnovsky (Plenum Press, New York) 1996, p.725.
[123] A.C. Switendick, *Solid State Commun.* **8** (1970) 1463; *Ber. Bunsenges.Phys. Chem.* **76** (1972) 535.
[124] V.E. Antonov, I.T. Belash, M.S. Zakharov, V.A. Orlov and V.I. Rashupkin, *Int. J. Hydrogen Energy* **11** (1986) 475.
[125] D.G. Westlake, *Trans. Metal. Soc. AIME* **245** (1969) 287.
[126] Ch.V. Kopetsky, V.A. Marchenko and G.I. Salnikov, *Fiz. Metallov i Metallovedenie* **59** (1985) 62 {in Russian}.
[127] G. Cannelli, R. Cantelli and M. Koiwa, *Phil. Mag.A* **46** (1982) 483.
[128] U. Zwicker and W. Böhm, *Z. Metallkde* **69** (1978) 600.
[129] J.K. Hulm and R.D. Blaugher, *Phys. Rev.* **123** (1961) 1599.
[130] W. Baden, P.C. Schmidt and A. Weiss, *J. Less-Common Metals* **88** (1982) 171.
[131] A.C. Switendick, in: *Topics in Appl. Phys.*, vol. 28: *Hydrogen in Metals I*, eds. G. Alefeld and J. Völkl (Springer-Verlag, Berlin) 1978, p. 101.
[132] P.V. Gel'd, R.A. Ryabov and L.P. Mokhracheva, *Hydrogen and the Physical Properties of Metals and Alloys* (Izd. Nauka, Moscow) 1985 {in Russian}.

[133] S.V. Vonsovsky, Yu.A. Izyumov and E.Z. Kurmaev, *Superconductivity of Transition Metals* (Springer-Verlag, Berlin) 1982.
[134] B.W. Roberts, *J. Phys. Chem. Ref. Data* **5** (1976) 581.
[135] V.E. Antonov, E.L. Bokhenkov, B. Dorner, V.K. Fedotov, G. Grosse, A.I. Latynin, F.E. Wagner and R. Wordel, *J. Alloys Compds* **264** (1998) 1.
[136] M. Baier, R. Wordel, F.E. Wagner, V.E. Antonov and T.E. Antonova, *J. Less-Common Metals* **172–174** (1991) 358.
[137] V.A. Somenkov and S.Sh. Shil'stein, *Z. Phys. Chem. N. F.* **117** (1979) 125.
[138] M. Baier, M. Karger, R. Ostermayer, F.E. Wagner, I. Dugandžić, H.J. Bauer, V.E. Antonov, T.E. Antonova, V.I. Rashupkin, S.M. Filipek and A. Stroka, *Z. Phys. Chem. N. F.* **179** (1993) 309.
[139] L.I. Vieland, A.W. Wicklund and J.C. White, *Phys. Rev. B* **11** (1975) 3311.
[140] R. Flükiger, in: *Superconductor Materials Science*, eds. S. Foner and B.B. Schwartz (Plenum Press, New York) 1981, p. 511.
[141] V.M. Pan, V.G. Prokhorov and A.S. Shpigel, *Metal Physics of Superconductors* (Naukova Dumka, Kiev) 1984 {in Russian}.
[142] J. Elton and H. Oesterreicher, *J. Less-Common Metals* **90** (1983) L37.
[143] A.I. Kolesnikov, I. Natkaniec, V.E. Antonov, I.T. Belash, V.K. Fedotov, J. Krawczyk, J. Mayer and E.G. Ponyatovsky, *Physica B* **174** (1991) 257.
[144] V.N. Kuznetsov and G.P. Zhmurko, *J. Less-Common Metals* **163** (1990) 1.
[145] B.I. Nikolin, *Multilayer Structures and Polytypes in Metal Alloys* (Izd. Naukova Dumka, Kiev) 1984 {in Russian}.
[146] H.L. Skriver, *Phys. Rev. B* **31** (1985) 1909.
[147] R. Andrievskii and Ya. Umanskii, *Interstitial Phases* (Izd. Nauka, Moscow) 1977 {in Russian}.
[148] R.A. Webb, J.B. Ketterson, W.P. Halperin, J.J. Vuillemin and B.B. Sandesara, *J. Low Temp. Phys.* **32** (1978) 659.
[149] Ch. Buchal, F. Pobell, R.M. Mueller, M. Kubota and J.R. Owers-Bradley, *Phys. Rev. Lett.* **50** (1983) 64.